Optimization of the Optical Infrastructure and Trapping Potential for a Quantum Processor Based on Trapped Barium Ions

by

XingHe Tan

A thesis
presented to the University of Waterloo
in fulfillment of the
thesis requirement for the degree of
Master of Science
in
Physics (Quantum Information)

Waterloo, Ontario, Canada, 2023

Author's Declaration

I hereby declare that I am the sole author of this thesis. This is a true copy of the thesis, including any required final revisions, as accepted by my examiners.

I understand that my thesis may be made electronically available to the public.

Abstract

Trapped ion quantum computers represent a cutting-edge quantum computing platform, keeping the highest reported state preparation and measurement fidelity of 99.97%. Recently, barium ion has emerged as the research interest of several teams due to its exceptional characteristics, including visible and inferred state transition frequencies, long-lived metastable states, and a simple hyperfine structure. Our research group aims to demonstrate trapping 16 $^{133}\text{Ba}^{+}$ ions on a micro-fabricated surface trap and build a quantum computing platform. In the long run, we intend to open access to this platform for the academic community to use. This project is named the QuantumIon project.

The project started in 2019, just before the global pandemic. During the pandemic, the QuantumION team did not have the lab space and the components to prototype and benchmark subsystems in parallel with system design. Instead, the team designed the entire system on computers during the pandemic. I joined the QuantumION team in 2022 and performed the system assembly, validation and optimization when the pandemic restrictions were lifted. In this thesis, I describe the optimization of the optical system for delivering laser beams to the ions and the validation of a 0.6 NA imaging system that will be used to observe the ion fluorescence as a means of measuring its quantum state. While benchmarking the optical systems, I found that the performance of the components deviated from their ideal specifications, such as insertion loss. Therefore, I had to modify the system design to ensure the optical systems functioned in practice. In addition, I conducted a feasibility study on delivering an ablation laser via multimode fiber and simulated a trapping potential on the surface trap that achieved approximately even spacing for 12 out of the 16 trapped ions.

Acknowledgements

I am grateful to my supervisor, Prof. Kazi Rajibul Islam, for supporting and guiding me on the thesis. His patience and professionalism set an example to me of how scientists treat mistakes and solve problems. I am also grateful to Prof. Crystal Senko for the enlightening discussions during our many meetings and for the trapped-ion course she taught, from which I greatly benefited. I'm greatly thankful to my committee members, Prof. Ray Laflamme and Prof. Jonathan Baugh, for joining my advisory committee and dedicating precious time to thesis review.

I sincerely appreciate all members of the QuantumIon lab for a supportive and creative environment. I enjoy working and discussing with my fellow labmates: Noah Greenberg, Collin Epstein, Akbar Jahangiri Jozani, Ana Bershanska, Akimasa Ihara, and Ali Mustafa Khatai. Also, many thanks to Ali Binai-Motlagh, Mahmood Sabooni, and Matthew Day, who graduated. And to the many co-op students I've worked with.

I want to thank friends from other labs: Sainath, Sakshee, Gilbert, Nikhil, Lewis, Jingwen, Anthony, Yu-Ting, Brendan, and Pei-Jiang. Their suggestions and their experience helped me to improve my work.

Dedication

This is dedicated to my beloved.

Table of Contents

List of Figures

List of Tables

List of Abbreviations

AHU Air Handling Unit 3

AOM Acousto-Optic Modulator xi, xviii, 12, 15–18, 22, 66

BD Beam Dump xv, 60

BPS Broadband Polarizing Beamsplitter Cube xii, 30

CCD Charge-Coupled Device xiv, xv, 41, 43, 48, 49, 60, 62, 63

CRM Cooling, Repumping, Measurement x, xii, xiii, 4, 27–29, 31–35, 37, 39

CW Continuous Wave 60

DC Direct Current 68, 70, 72, 78

EDS Energy-Dispersive X-ray Spectroscopy xv, 53, 54

EOM Electric-Optic Modulator xi, xviii, 9, 12, 15, 18–23

HDR High Dynamic Range xiii, 10, 26, 27, 33–35, 37, 39

HWP Half-wave Plate xii, 30

LIDT Laser Induced Damage Threshold 56, 63, 64

MS Mølmer-Sørensen 2, 78, 80, 81

NA Numerical Aperture 56, 67

PD	Photodiode xii, xv, 30, 60
PMT	Photomultiplier Tube xiv, 3, 42–45, 48
PPLN	Periodically Poled Lithium Niobate 15
RF	Radio Frequency xi, xvii, xviii, 16–19, 21, 68–71, 73, 78–80, 82
RGB	Red, Green, Blue 10, 22
sCMOS	scientific Complementary Metal–Oxide–Semiconductor xiv, 3, 11, 42–46
SPAM	State Preparation and Measurement 2

Chapter 1

Introduction

In the 20th century, Max Planck, Albert Einstein, Niels Bohr, Louis de Broglie, Max Born, Paul Dirac, Werner Heisenberg, Wolfgang Pauli, Erwin Schrödinger, Richard Feynman, and other scientists developed quantum mechanics that once again revolutionized people's perspective about the universe. From there, other branches of science flourished, such as chemistry, biology, material science, and information science. In 1983, Feynman proposed using a machine that obeys quantum mechanics to simulate nature [19]. Yuri Manin [9] and Paul Benioff [13] are also credited for contributing to forming the idea of quantum computers before Feynman. Operating under different laws of physics, quantum computers can solve some problems more efficiently than classical computers. One of the most famous is Shor's factoring algorithm [31]. Using this algorithm, one can calculate prime factors of a large integer in practical time. It can crack the widely used encryption method, the Rivest–Shamir–Adleman (RSA) algorithm, which relies on large prime numbers. This power is so strong that people define building a quantum computer as solving a problem that classical computers could not, achieving quantum supremacy. In 2017, quantum key distribution from satellite to ground has been experimentally demonstrated[29]. This key distribution method can detect if the communication has been eavesdropped. Thus, it could secure communication once again.

On the other hand, practical developments in quantum computation have also made significant progress. Researchers have investigated various types of qubits, such as ions, photons and synthesized qubits, to perform quantum computations. In the last decade, many milestones have been achieved, such as solving a sampling problem using synthesized qubits and photons [12, 44] and development in error correction code using ions as qubits [37]. Besides the three examples, there are many other experiments that mark the milestone for different types of qubits. Development on each type is at a different level of maturity, and they face different challenges in scaling up the number of qubits.

Trapped ion quantum computers utilize ions as qubits, which offer several advantages over other types of qubits. For example, the quantum state encoded in an ion can maintain coherence for up to an hour[41]. Additionally, the fidelity in the State Preparation and Measurement (SPAM) of an ion is notably high, with a record of 99.97% fidelity achieved on a trapped ion quantum computer using a barium ion[16]. However, there are also challenges associated with using ions as qubits. Most ions, such as ytterbium and calcium, require ultraviolet (UV) light to drive state transitions. The lack of waveguided optical modulators for UV wavelengths makes the optical engineering for trapped ion quantum computers particularly challenging.

$^{133}\mathrm{Ba}^{+}$, on the other hand, does not require UV lasers for quantum operations. All the necessary laser frequencies to drive state transitions are within the visible and infrared regions, making the waveguided optical modulators more commercially available. Another unique property of $^{133}\mathrm{Ba}^{+}$ is its 35 s lifetime $5\mathrm{D}_{5/2}$ metastable state, which is long compared to the typical operation time in the millisecond scale. This allows for the exploration of complex quantum operations, such as storing qubits in the metastable state (known as quantum memories), implementing same-species sympathetic cooling through an Optical, Metastable, and Ground state (OMG) architecture[11], and encoding more than two states in a qubit (known as qudits). However, $^{133}\mathrm{Ba}^{+}$ is radioactive. To ensure lab members' safety, the quantity is restricted to a few micrograms according to regulations. The quantity problem restricts the ion loading method to laser ablation. This method generates high-speed ions, requiring a deep potential depth for trapping. Barium ions have been successfully trapped in a four-rod trap[15]. Compared to a four-rod trap, a surface trap offers more flexibility in manipulating the electric potential, allowing for ion shuttling and the generation of non-harmonic potential. However, the potential depth of the surface trap is shallow, making ion trapping more challenging[43]. We aim to demonstrate the trapping of Barium-133 in a surface trap.

The QuantumIon project aims to build a 16 qubits barium-based surface trap quantum computer. We want to demonstrate all basic quantum operations, such as SPAM and Mølmer-Sørensen (MS) gate, and explore more advanced quantum operations, such as storing state in a metastable state, same spices sympathetic cooling, and encoding more than two states in one ion. Because waveguided optical modulators are commercially available, we have been able to demonstrate control on delivering 16 individually modulated laser beams to each ion, which we call the individual addressing system[14]. In the long run, we intend to open access to the QuantumIon platform to the academic community to perform experiments, giving users access to both software and hardware levels. We also designed robust and modular optical systems to minimize downtime for a repair or update.

This ambitious project is only possible when mechanical components, electronic devices, optical elements, and software are all working with each other appropriately. The layout of the system is shown in Fig 1.1. The quantum computing platform is primarily divided into three major sections: the optical table, the optical rack, and the electronics rack. The electronics rack houses the servers that run the software and electronic devices that control the quantum computing platform. We use the Advanced Real-Time Infrastructure for Quantum physics (Artiq) system and the Sinara hardware system to generate electric signals in real-time with nanoseconds precision [5]. To ensure a stable climate (temperature and humidity) for the optical systems, the optical table and the optical rack are housed inside an Air Handling Unit (AHU). The electronics rack, which generates heat, is positioned outside the AHU. The optical rack is equipped with laser controllers, laser generators, and laser modulators. Its primary function is to generate and modulate lasers. The optical table accommodates the vacuum chamber, which contains the ion trap; the free-space optical devices such as lenses and mirrors to deliver lasers; and a high numeric aperture system (0.6 NA) that uses sCMOS and PMT to detect the ion's fluorescence.

The QuantumIon project is a collaborative project between Professor Kazi Rajibul Islam and Professor Crystal Senko that started in 2019. This complex project requires the integration of hundreds of different types of components. Normally, subsystems should be prototyped and benchmarked in parallel with the system design. However, due to the global pandemic, lab access was limited, and the global supply chain crisis delayed the delivery of components indefinitely. Therefore, the QuantumIon team did not have the lab space and the components needed to conduct research in the conventional way. The team adopted a different strategy: to design the entire system first, then validate and benchmark the systems when the restrictions are lifted. A detailed computer-aided design (CAD) is also needed to build a robust system. Thus, the new strategy still works in our favour.

I joined the QuantumIon project in 2022 when the system design was completed and we were in the assembly stage. My main contribution to the project is to verify and benchmark the optical system. During my work, I found the actual performance of the components deviates from their specifications. Therefore, I must also optimize the optical systems to ensure they function in practice. Besides optical system optimization, I simulated trapping potential and conducted a feasibility study on a new subsystem design. In the rest of the introduction, I will first introduce the $^{133}\text{Ba}^{+}$ and the basic operations needed to trap one ion. Then, I will highlight the necessary components to perform these operations. Lastly, I will briefly summarize each chapter and highlight contributions and acknowledgements in each chapter. In this thesis, I hyperlinked the abbreviations in blue ink to a list of abbreviations. I have also hyperlinked each laser wavelength highlighted in blue ink to a

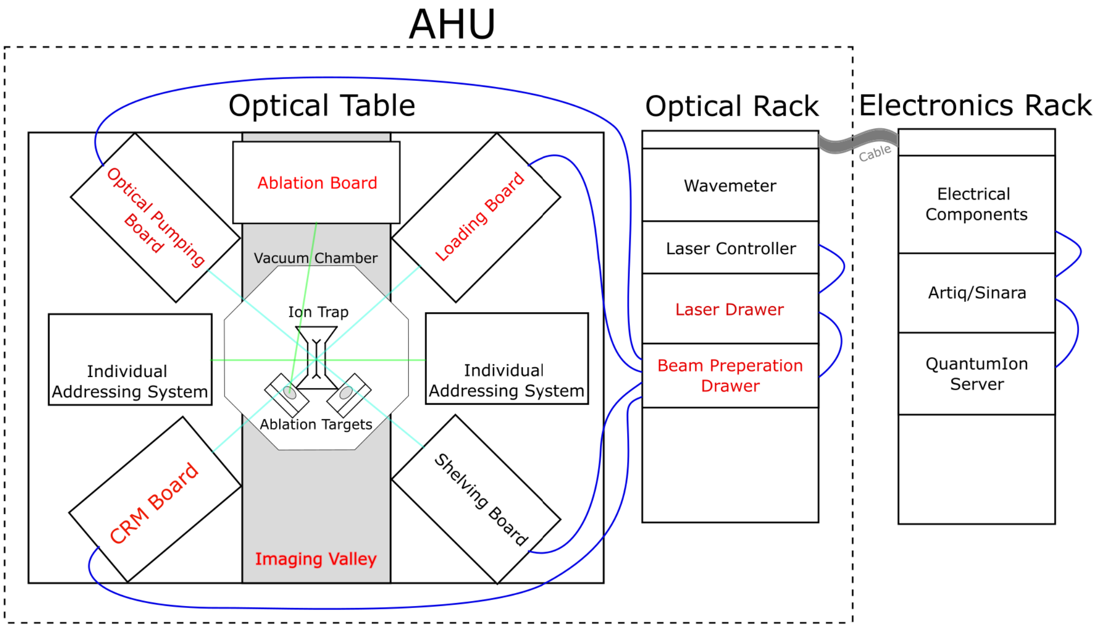

Figure 1.1: A sketch of the entire QuantumIon project setup. The components highlighted with red ink are components I worked on. The optical pumping board, loading board, CRM board, and shelving board are the optical boards that focus lasers onto the ions.

list of the descriptions of the lasers in the glossary.

1.1 Introducing Barium-133 Ion

Barium-133 is an alkaline earth metal. It becomes hydrogen-like when one of the two valence electrons is stripped. The energy structure of $^{133}\text{Ba}^{+}$ is shown in Fig 1.2. It has a nuclear spin of 1/2, so $^{133}\text{Ba}^{+}$ has a simple hyperfine structure. We encode the basis states into the clock states where $|0\rangle \equiv |F=0, m_f=0\rangle$, and $|1\rangle \equiv |F=1, m_f=0\rangle$[15].

$$|I-J| \leq F \leq |I+J| \tag{1.1}$$

$$-F \leq m_f \leq F \tag{1.2}$$

The clock states are insensitive to external magnetic fields, which allows us to take advantage of the Zeeman effect to split the hyperfine levels further [20]. This way, we will not address the unwanted hyperfine state during operations. The other advantage of ^{133}Ba$^+$ is the long metastable state 5D$_{5/2}$. It has a lifetime of 35 s, which allows us to study some unique quantum operations, such as quantum memory and the OMG architecture[11]. In addition, all the relative transition frequencies are in the visible or inferred range, which makes the fiber optical devices more accessible and affordable, so a modular plug-and-play system is possible. However, this isotope is radioactive. Safety policy requires lab members not to exceed the annual dose of 1 millisievert (mSv), which is equivalent to the radiation from 10,000 bananas. In comparison, the amount of radiation dosage people are exposed to during one typical chest x-ray is 0.1 mSv.

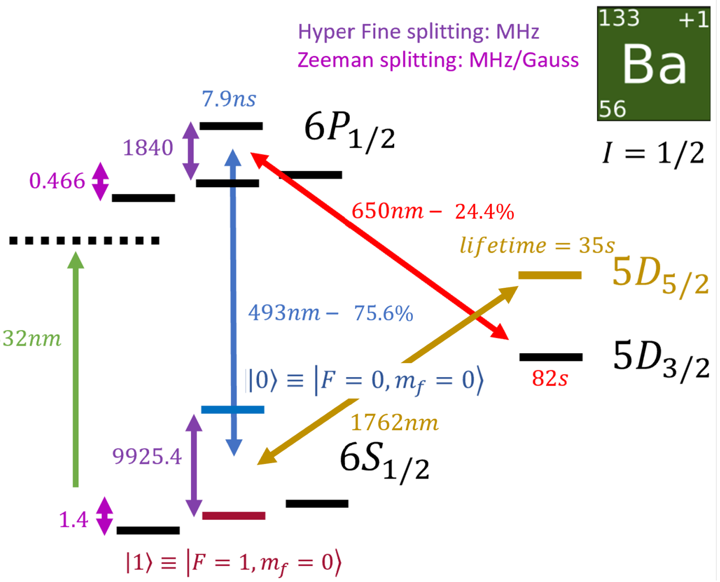

Figure 1.2: The energy level of the ^{133}Ba$^+$. The qubits are encoded in the 6S$_{1/2}$ clock state. The 5D$_{5/2}$ state is used as the shelving state because the lifetime is long and it won't be affected by other operations due to differences in transition frequencies. Figure adapted from [15].

1.1.1 Ion Loading

The isotope we chose to study, ^{133}Ba$^+$, is radioactive. We can only use < 5 μg to meet the University's safety policy. We chose the laser ablation method to load ions where an intense pulse laser is sent to a target that holds the ablation material. The ablation laser only heats and sublimates a fraction of the sample, which allows us to load Barium ions thousands of times from micrograms worth of sample [42]. ^{133}Ba is not naturally abundant. It is synthesized through a nuclear reaction. Therefore, we cannot obtain ^{133}Ba in metallic form; we can only obtain it in salt form. Thus, the ablation target is barium chloride. We use a pulsed 532 nm laser to ablate the target because it is a commercially available laser. Obtaining pure ^{133}Ba is nearly impossible. So, ablation would generate a range of different barium isotopes. We use the two-step photoionization process to select the desired isotope. A 553 nm laser is used for the first photoionization step. It drives the transition of neutral barium from the $6S_0$ state to the $6P_1$ state. This step is isotope selective due to the isotope shift. A 405 nm laser does the second step of photoionization. It will drive an electron into the continuum, thus ionizing the atom, as shown in Fig 1.3. The atoms in the plume generated through ablation have a high speed and spread in different directions. Therefore, to prevent the Doppler effect from shifting the first step transition frequency, the 553 nm laser should propagate perpendicular to the plume of atoms. The second photoionization step is less sensitive to frequency shift but sets the area of the ionization zone. We want the ionization volume to be small to prevent trapping contamination. Therefore, it should be perpendicular to the 553 nm laser and can be parallel to the plume of atoms, as shown in Fig 1.4.

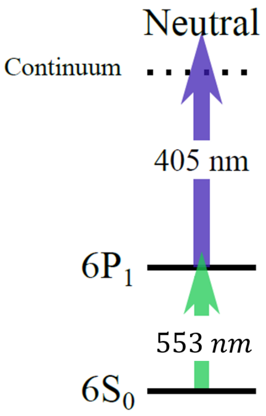

Figure 1.3: A sketch of the two-step photoionization process. The first step is an isotope selection step in which the transition from the 6S state to the 6P state is different between isotopes due to isotope shift. The second step drives an electron into the continuum with sufficient photon energy. Figure adapted from [23].

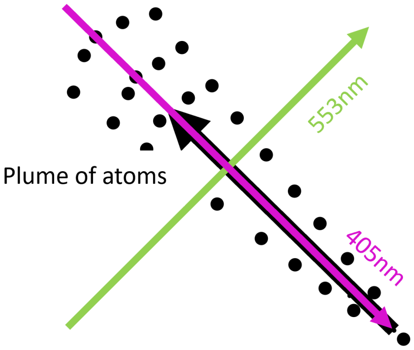

Figure 1.4: The orientation of the plume of atoms, 553 nm laser, and 405 nm laser. The 553 nm laser must be perpendicular to the plume of atoms to avoid frequency shift due to Doppler effect. The 405 nm laser must be perpendicular to the 553 nm laser to minimize ionization volume.

1.1.2 Doppler Cooling

A newly trapped ion is hot and moves too fast to be observed. Hence, we cool the ion through Doppler cooling. During state transition excited by photons, momentum is exchanged. When an ion moving in one direction absorbs a photon moving in the opposite direction, the net momentum of the ion decreases. When the ion emits a photon, the emitted photon scatters in random directions. Over time, the net momentum change induced by emitting photons averages to zero. Therefore, with a large number of photons, the net momentum of the ion decreased. A trapped ion is confined in the trap and oscillates in the trap. When the ion moves away from the laser source during half of the oscillation, the laser frequency decreases and results in a redshift, while moving toward the laser source during the other half of the oscillation, the laser frequency increases and results in a blueshift. By adjusting the addressing laser frequency, we match the blue-shifted frequency to the ion's transition frequency and excite state transition. Consequently, the red-shifted frequency is off-resonance and will not excite state transition. Overall, the ion slows down each time it circles to travel toward the laser source and thus cools. To cool an ion, we need the ion to emit photons continuously. Therefore, we need the 493 nm laser to drive ion from both $|0\rangle$ and $|1\rangle$ state to $6\mathrm{P}_{1/2}$ $|F=0, m_f=0\rangle$ state. However, there is a 23% chance the ion would decay to the $5\mathrm{D}_{3/2}$ state, which has a lifetime of 82 s. Therefore, we also need the 650 nm laser to pump the ion back to the $6\mathrm{P}_{1/2}$ state and complete an emission cycle. Fig 1.5 shows the state transitions required to perform Doppler cooling.

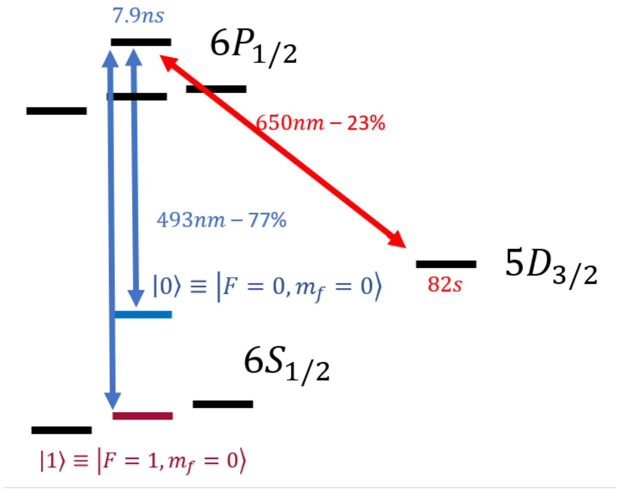

Figure 1.5: The Doppler cooling process. where the % shows the change in decay to that state. The time on the state shows the lifetime of the state. The goal is to drive a continuous excite and emit cycle.

1.1.3 State Measurement

State measurement is similar to Doppler cooling. We use the 493 nm laser to drive only from the 1 state to 6P$_{1/2}$ $|F = 0, m_f = 0\rangle$ state. According to the selection rules, 6P$_{1/2}$ $|F = 0, m_f = 0\rangle$ would not decay to 6S$_{1/2}$ $|F = 0, m_f = 0\rangle$ state because they have the same J number. With a 650 nm laser to pump ions out of the metastable state, we are completing an emission cycle for only the $|1\rangle$ state. Therefore, if the ion is in the $|1\rangle$ state, it will be bright. If the ion is in the $|0\rangle$ state, it will be dark. Fig 1.6 shows the state transitions required to perform state measurement.

1.1.4 Summary of Optical Devices Needed to Perform the Operations

Photoionization, Doppler cooling, and state measurement are three basic operations needed to trap an ion and check if an ion is trapped. In fact, Doppler cooling without detuning is what we need to observe if an ion is trapped because no matter which state the ion is in, it will fluoresce to confirm its existence. The ion trapping process requires 493 nm, 650 nm, 532 nm, 405 nm, and 553 nm lasers. The 493 nm, 650 nm and 532 nm require frequency

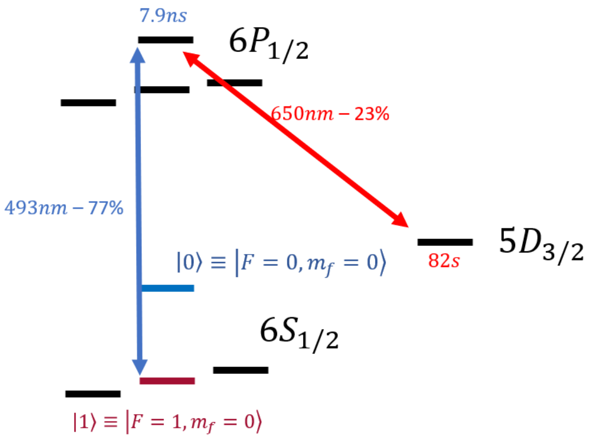

Figure 1.6: The state measurement process. where the % shows the change in decay to that state. The time on the state shows the lifetime of the state. The goal is to drive a continuous excite and emit cycle only when the ion is in the1 state.

control. Therefore, we need EOMs to modulate the laser frequencies. 553 nm laser was generated from a 1107 nm laser source whose frequency is doubled by a doubler. More details are shown in Chapter 2

1.2 System Layout

The very core of the system is the ion trap. It is contained inside a vacuum chamber along with an ablation target. The ultra-high vacuum environment is needed to prevent ions from being knocked out of the trap. The vacuum chamber has nine ports. Eight viewports are on the sides and form a hexagon; the ninth one is at the bottom of the chamber, which provides optical access for the imaging system. The customized optical table has a valley dedicated to the imaging system. One of the eight ports is used for electrical connections to the trap. Opposite to it is the viewport for the ablation laser. Two ports on the side are for the individual addressing system, where we apply a laser to each individual ion. The rest of the diagonal ports are for the global beams, which a laser will address all 16 ions, as shown in Fig 1.1. Around the chamber are the optical boards that deliver lasers onto the ions. The ablation board delivers the 532 nm laser to ablation targets. The 493 nm, 650 nm and 553 nm are delivered through the loading board. The 405 nm laser is delivered through the optical pumping board. The laser source of the ablation board is on the ablation board, but the 493 nm, 650 nm and 553 nm laser sources are on the optical rack. The optical rack has four layers: wavemeter, laser controllers, laser drawer, and beam preparation drawer. The wavemeter measures the laser frequencies and feedback to laser controllers to lock the laser frequencies. The laser sources are fiber coupled in the laser drawer, and then the fiber connects to the beam preparation drawer, where the lasers' phase, frequency, and intensity are adjusted. Lastly, the lasers are combined by an Red, Green, Blue (RGB) fiber-coupled combiner and delivered to the optical boards.

1.3 Chapter Outline and Author's Contribution

The rest of the chapters are structured as such, highlighting the author's contributions:

- Chapter 2 is about optimizing laser power. It first shows the power requirement for each laser and then describes how the insertion loss of each component is measured. Last, it reports the measured insertion loss of every component along a beam path and the power at the ions. The author is credited for testing the optical modulators, reducing and reorganizing the beam paths in the beam preparation drawer, testing all lasers in the beam preparation drawer and optimizing the power output of the 493 nm and 650 nm paths. Acknowledgements are given to Noah Greenberg and Akbar Jahangiri Jozani for spending time communicating with the supplier and sending the 553 nm laser back for repair. Acknowledgements are also given to Ali Binai-motlagh for valuable support and to Mark Elliott Wallace and former colleagues for system design and assembly.

- Chapter 3 focuses on the beam-shaping functionality of the optical boards. It describes the optical boards' structure, functions, and the beam-shaping telescope design in more detail. It also states the beam shaping reason and requirements. The author is credited for fine-tuning the beam-shaping telescopes and taking beam profiles to verify the result. Acknowledgements are for Ali Binai-motlagh, who taught me how to adjust the beam shape, take beam profile using a scanning slit beam profiler, and perform HDR profiling using the Python code he wrote. Acknowledgements are also given to Noah Greenberg and former members for designing the optical boards and to Ali Binai-motlagh, Stephen Del Grosso Milek and Mark Elliott Wallace for assembling the optical boards and for their support.

- Chapter 4 shows the imaging system is capable of imaging the ions. It first introduces the beam paths in the imaging system design in detail, then describes the aligning process for each beam path, and lastly displays the image of the trap's surface taken by the sCMOS camera in the system and argues that the image demonstrates the camera's ability to image the ions. The author is credited for aligning the imaging system and imaging the trap's surface. Acknowledgements are given to Noah Greenberg for designing the system, to Ali Binai-motlagh for his support and assistance in aligning the imaging system, and to Stephen Del Grosso Milek and Mark Elliott Wallace for assembling the system.

- Chapter 5 reports the result of the feasibility study on ablation via multimode fiber. It first conveys the advantages of ablation via multimode fiber. Then, analyze the possibility and propose a setup that theoretically works. Finally, reports the negative experiment results, analyzes the points of failure and proposes a new setup that would work. The author is credited for performing the theoretical works, simulating the optical setup using Zeemax opticstudio and performing the experiment. Acknowledgements are given to Sakshee Samir Patil, who taught me how to use Zeemax opticstudio. I would also like to acknowledge Noah Greenberg and Akbar Jahangiri Jozani for testing the ablation system and providing valuable data I can reference for this project.

- Chapter 6 shows the simulation result on a potential generated by a surface trap that can space the ions evenly. It first introduces how a four-rod trap traps an ion, and makes the comparison to a surface trap. Then, it describes how I calculate the potential, equilibrium position, and secular frequencies. Lastly, it provides a potential that gives close to equally spaced configurations and analyzes the properties of this potential configuration. The author is credited for writing programs to simulate and analyze the potential based on the Python package written by Jay Van Der Wall (Sandia National Laboratories) and Collin Epstein. Acknowledgments are given to Jay Van Der Wall, Collin Epstein, and Sandia National Laboratories for the amazing surface trap and for allowing us to use the Python package, and to Professor Rajibul Islam for giving me guidance and support on this project.

Chapter 2

Laser Sources and Beam Preparation Systems

The first major technical milestone of the QunatumIon project is to demonstrate trapping ions in the surface trap. One of the requirements for trapping ions is that all lasers addressing the ions should deliver sufficient laser power to the ions. Without sufficient power, the rate of state transitions would be slow and thus lower the efficiency of operations. However, every component between the laser source and the ions will reduce the laser power. Thus, the final laser power at the ions should be checked.

Before reaching the ions, laser beams would go through many optical devices. The laser drawer is where we store the laser sources and couple them into fibers. The fiber then delivers beams to the beam preparation drawer for necessary modulations. Lastly, the beams are delivered to the optical boards on the optical table. The optical boards will then focus the beam onto ions. The beam preparation drawer prepares the beam in three steps: modulation, fast switch, and grouping. Modulation is done by Electric-Optic Modulators (EOM). EOM can modulate the laser's phase, amplitude, and frequency. The fast switching is done by Acousto-Optic Modulators(AOM). Lastly, beam splitters and beam combiners distribute lasers to each optical board. Besides the modulators, we also used many beam splitters and mating sleeves. Mating sleeves were used to join two fibers. Beam splitters were placed between every modulator to provide power or frequency monitoring. As an example, the 493 nm laser path is shown in Fig. 2.1. The power monitoring was a necessary reading for proper remote control. However, the loss of the system is too large that there is no laser power outputting from the beam preparation drawer. My main objective is to reduce the insertion loss of the beam preparation drawer. To resolve this problem, I plan to use three steps. First, I will measure the insertion loss of each component and

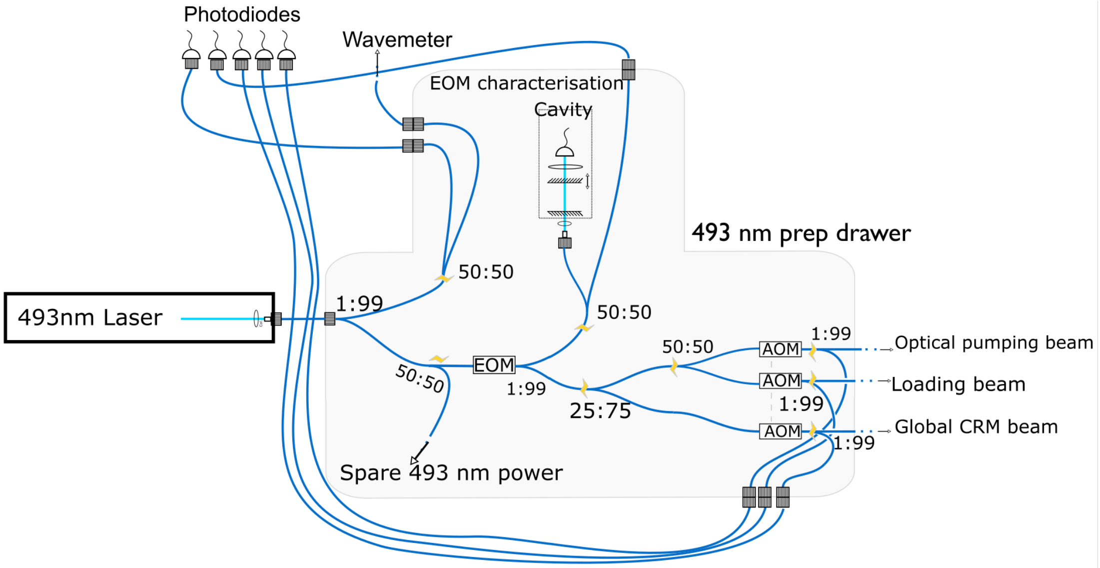

Figure 2.1: The original design of the 493 nm path is complicated and has beam splitters that sample the beam after every component.

identify problematic ones. Second, unnecessary components, such as monitoring paths, will be removed for the trapping test. The final step involves reducing insertion loss for the remaining components. Following these steps, I successfully measured sufficient laser power output. My contributions are as follows:

1. I redesigned and reassembled the beam preparation drawer.
2. I measured the insertion loss of each component.
3. I confirmed sufficient 493 nm and 650 nm laser power output.

The section 2.1 calculates the power requirement for each laser. The section 2.2 displays the tested insertion loss for each component. The section 2.3 states the solution applied to reduce insertion loss and the amount of output power after applying the solutions. The section 2.4 reports the problem remains unsolved. I want to acknowledge Noah Greenberg and Akbar Jahangiri Jozani for fixing the 553 nm laser and verifying sufficient power output and to Mark Elliott Wallace and former teammates for designing and assembling the original design.

2.1 Power requirement

Out of all the lasers, only the lasers that go through the beam preparation drawer (the 493 nm and the 650 nm lasers) do not have sufficient power at the ion. The 493 nm and 650 nm lasers drive specific state transitions in ^{133}Ba. Their power requirements are determined by the saturation intensity. Saturation intensity is related to the scattering rate. The scattering rate defines how fast an ion emits photons when a laser excites a specific two-level transition. A higher scattering rate means the ion appears brighter on an image [20].

$$R_{sat} = \frac{1}{2\tau}\frac{I/I_{sat}}{1 + I/I_{sat} + 4\delta^2\tau^2} \tag{2.1}$$

Where τ is the lifetime of the transition and δ is the frequency detuning from the resonance frequency of the transition. Going beyond the saturation intensity does not increase the scattering rate. Hence, the laser intensity should be adjusted to match the saturation intensity, which is given by:

$$I_{sat} = \frac{\pi}{3}\frac{h\ c}{\lambda^3\tau} \tag{2.2}$$

Where h is Planck's constant, c is the speed of light in vacuum, λ is the transition wavelength, and τ is the lifetime of the transition. The saturation intensity of each wavelength is listed in table 2.1.

Wavelength (nm)	Saturation Intensity (W/m^2)	Saturation Power (μW)
493.40	219.2	2.75
649.68	96	1.2

Table 2.1: saturation power is calculated using the area of the reshaped beam.

The 553 nm laser drives a specific transition in ^{138}Ba, which is used in the photoionization process. Based on previous experiments conducted by group members, the power required for the initial ionization step at 553 nm is approximately 15 μW [23]. Even though the largest power needed is 15 μW, we aim to provide laser power of 100 μW at the ions for the unmodulated laser to provide sufficient power when the laser is modulated.

2.2 Insertion Loss of the System

The first step in addressing the power issue is to measure the insertion loss of each component. Identifying problematic components is crucial for forming a proper plan. We use insertion loss instead of efficiency because it simplifies calculations. The total insertion loss of the entire system is the sum of the insertion loss of individual components. This approach provides a clearer understanding and facilitates our optimization efforts.

$$\begin{gathered} IL_{\text{system}} = \sum IL_{\text{component}} \\ IL = 10\log_{10}(\frac{P_{\text{in}}}{P_{\text{out}}}) \end{gathered} \tag{2.3}$$

The insertion loss of doubler, AOM and EOM are not constant; they depend on extra variables. Thus, their testing plans are described in the following subsections.

2.2.1 Doubler Test

A doubler utilizes non-linear optical material, usually Lithium Niobate crystal, to achieve second harmonic generation. Two photons with frequency ω excite the material's ground state twice to reach a virtual state. This virtual state then decays and emits one photon with a frequency twice that of the input photon, carrying twice the energy. In our case, the input frequency is 270.8 THz (1107 nm), and the output frequency is 542.1 THz (553 nm). The output power is[6]:

$$P_{\text{out}} = \mu P_{\text{in}}^2 \tag{2.4}$$

where μ is the coefficient with unit %/W ($\mathrm{P_{out}/P_{in}^2}$). both the input and output photons exhibit extraordinary polarization with respect to the crystal. To achieve net positive energy, quasi-phase-matching is employed in the waveguide. This involves inverting the polarization of the waveguide every half coherent length. The coherent length represents the distance the laser travels inside a medium during one period of time. The quality of phase matching directly affects the output power. Additionally, quasi-phase matching is sensitive to temperature. Therefore, optimizing the doubler's temperature is essential.

The doubler we use is the Periodically Poled Lithium Niobate (PPLN) waveguide module supplied by NTT Inovated Device. The doubler's temperature is precisely controlled using a temperature controller. The experiment setup is shown in Fig. 2.3. The optimal temperature for the doubler is 47.83 °C, and the efficiency coefficient is 56.6%/W. With an input power of 27 mW, the output power of 412 μW.

2.2.2 AOM Test

AOM utilizes the acoustic-optic effect to deflect the laser to different angles and modify the frequency of a laser. The specific AOMs we acquired are the Fiber-Q fiber-coupled

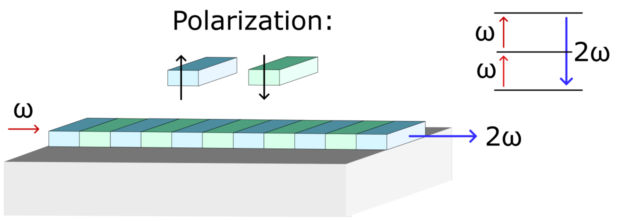

Figure 2.2: A sketch demonstrating how doubler works. The input laser with wavelength ω goes through Lithium Niobate crystals that flip polarisation every half coherent length, and the output laser will have wavelength 2ω. The polarization is flipped to match the phase of the laser, thus generating net positive power output. Image adapted from [6]

.

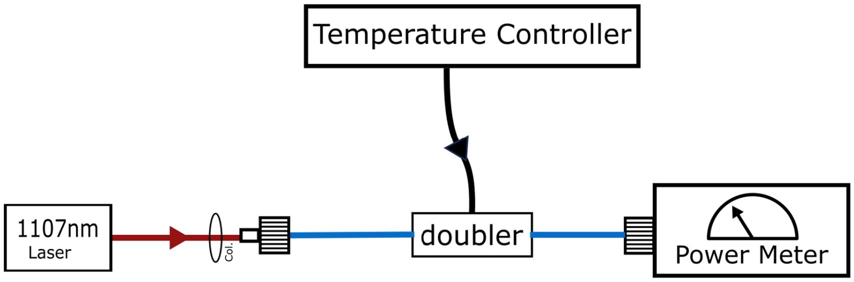

Figure 2.3: A sketch of the experiment setup. The doubler's temperature is controlled by a Temperature Controller. The power output is monitored by a power meter.

acousto-optic modulators from Gooch & Housego. A sketch of the AOM is shown in Fig. 2.4. AOM intake a Radio Frequency(RF) signal to drive a piezoelectric transducer, generating a sound wave that travels through the bulk material. This sound wave changes the uniform refractive index to a refractive index grating. When the incident laser beam encounters this grating, it gets deflected. The frequency of the deflected light is the sum of the incident light frequency and the RF frequency due to the Doppler effect, and the intensity of the deflected light is directly proportional to the amplitude of the RF signal. The rise and fall time of AOM is only about 25 ns [2], compared to a typical quantum gate operation time (μs scale [21, 36, 38, 10]), AOMs are fast enough to function as fast switch.

I used the E8241A PSG-L Series Performance Signal Generator to generate an RF signal. The signal is split by the ZAPD-30-S+ Mini-Circuits Power Splitter. One signal is

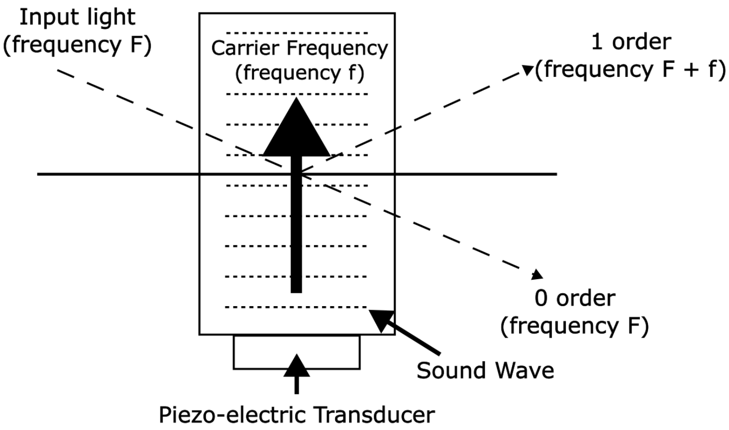

Figure 2.4: A sketch of laser entering AOM. The acoustic transducer sends sound waves, changing the refractive index to grids. The 0th-order beam is not deflected. The 1st-order beam is deflected, and the soundwave frequency is added to it. Image adapted from [1]

sent to an oscillator to monitor RF amplitude, while the other is amplified 30 dB by an amplifier and sent to the AOM. The 532 nm laser is used to test the 532 nm AOMs, while a 650 nm laser tests the rest of the AOMs. I optimized the AOMs' optical power output by adjusting the RF frequency. The RF power is slowly increased to a maximum (30 dBm) to prevent damaging the AOMs. The test setup is shown in Fig. 2.5.

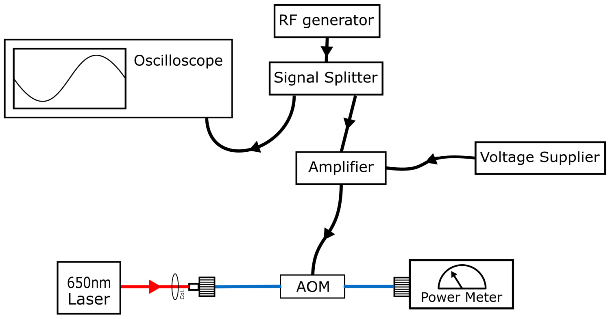

Figure 2.5: A sketch of the AOM experiment setup. The AOM is controlled by the signal generated by an RF generator. The oscilloscope is used to monitor the RF power. The power meter is used to monitor laser power output.

The optimum setting of each AOM is listed in table 2.2. The insertion loss of most AOMs I have tested does not meet the specified requirement of less than 2.5 dB. We conjecture that this deviation is caused by the difference in the designed operating laser wavelength as shown in table 2.2 and the actual applied wavelength (650 nm). An additional phenomenon I have observed is that the AOMs seem to be directional. The insertion loss of AOMs when the laser passes in one direction is around 2 dB lower than in the other direction. This behaviour is unexpected, as the direction of propagation can be inverted without changing the beam path. It's possible that the deflected beam has some aberration that was mechanically optimized for one propagation direction, leading to a higher loss in the other direction. Excluding the 532 nm AOMs, the average insertion loss is 3 dB, which is used as a reference value for future estimations.

AOM Label	RF frequency (MHz)	RF amplitude(dBm)	Insertion Loss (dB)
637nm AOM1	192.24	30	3.06
637nm AOM2	200	30	3.04
637nm AOM3	194	30	1.99
633nm AOM	200	30	2.46
532nm AOM1	200	30	4.09
532nm AOM2	200	30	7.7

Table 2.2: The optimum RF configuration for each AOM and the optical insertion loss under the configuration.

2.2.3 EOM Test

An EOM utilizes the linear electro-optic effect. It works by applying an oscillating external electric field to a Lithium Niobate crystal, which changes its refractive index. This alteration in refractive index, in turn, modifies the optical path length within the medium. As a result, the laser experiences a different phase. Consider the EOM with frequency Ω and small amplitude β adds phase to a laser with frequency ω and amplitude A:

$$\begin{gathered} u_{(t)} = Ae^{i(\omega t+\phi(t))} \\ \text{where } \phi(t) = \beta\sin(\Omega t) \end{gathered} \tag{2.5}$$

Taking the Jacobi-Angur expansion,

$$Ae^{i\omega t+i\beta\sin(\Omega t)} = Ae^{i\omega t}[J_0(\beta) + \sum_{n=1}^{\infty} J_n(\beta)e^{in\Omega t} + \sum_{n=1}^{\infty}(-1)^n J_n(\beta)e^{-in\Omega t}] \tag{2.6}$$

The first term, $J_0(\beta)$, is the carrier; the latter two describe a pair of frequency sidebands. There are infinite pairs of sidebands, but their amplitude depends on the amplitude of the RF signal. We denote the voltage that achieves a phase shift of π as the half-wave driving voltage, V_π. To achieve a full modulation depth, one should drive the phase from $-\pi$ to π, meaning the peak-to-peak voltage, V_{pp}, of the RF signal should be $2V_\pi$. V_π is usually provided by the manufacturer. The modulation depth is described by:

$$\left| \frac{\phi}{\pi} \right| = \frac{V_{\text{pp}}}{2V_\pi} \tag{2.7}$$

To characterize the EOMs, the relationship between modulation depth and the intensity of the carrier and sidebands will be examined. Fabry-Perot cavity is used to detect the frequency sidebands. A piezo motor keeps changing the length of the cavity, thus scanning the resonance frequency of the cavity. The laser exits the cavity only when its frequency matches the cavity's frequency. By probing the output laser with a photodiode, we can measure the frequency of the laser. Fig. 2.6 shows the experiment setup. Fig. 2.7 shows a frequency diagram of the laser. The tallest peak represents the carrier frequency, while the smaller bumps are the first-order sidebands.

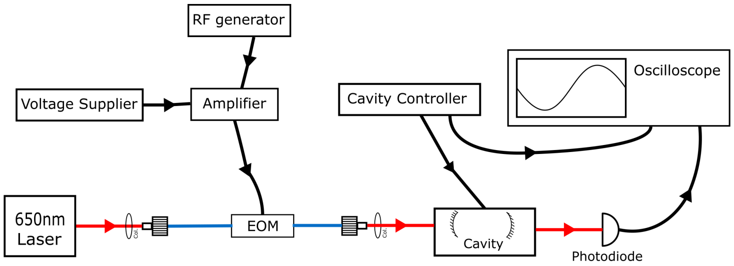

Figure 2.6: a sketch of the EOM experiment setup. The RF generator sends the signal to EOM. The cavity is used to measure the frequency of the laser after EOM.

The amplitudes of the carrier and the sidebands at different modulation depths were recorded, and the data was fit to equation 2.6. The plots in Fig. 2.8. show the results for three different EOMs at two different RF frequencies. Notice that as the RF frequency increases, the RF voltage required to achieve the same sideband power also increases. We need separate plots for low-frequency and high-frequency cases.

Importantly, the insertion loss of the EOMs is measured without RF input, so the power output corresponds to the peak power of the carrier. Using the plots from Fig. 2.8, the power of the sidebands can be calculated from the peak power of the carrier. The insertion loss of the EOMs is listed in the table 2.3.

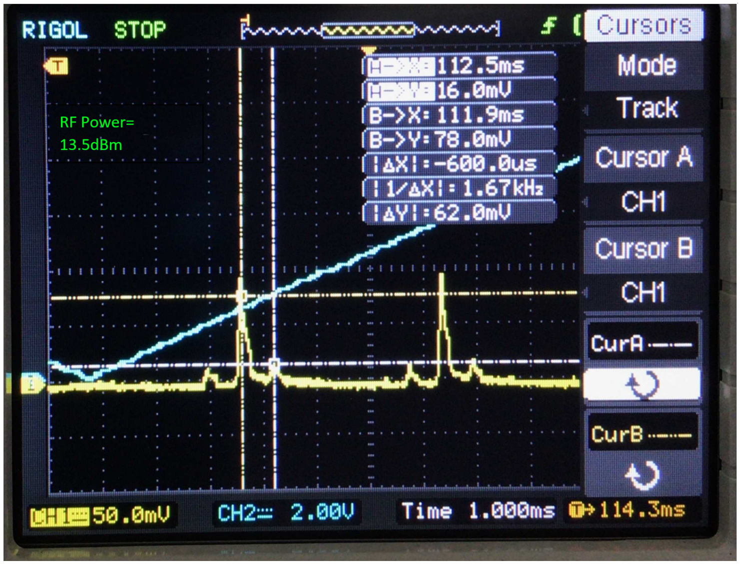

Figure 2.7: The sidebands of the modulated signal plotted by an oscilloscope. The horizontal axis is the fabry-perot scan time. The vertical axis is the output spectrum. The yellow line plots the modulated signal. The blue line plots the voltage to the piezo transducer that drives the cavity's length. The high peak at the center is the carrier frequency. The two small peaks on the sides are the first-order sideband. The peaks are skewered due to the Doppler effect of the moving mirror.

Label	Insertion Loss (dB)
493nm Jenoptik	5.23
650nm Jenoptik	6.02
493nm AdvR	4.07

Table 2.3: The insertion loss of the EOMs

2.2.4 Insertion Loss of Each Component

The insertion loss of the rest of the devices can be measured easily. Table 2.4 shows the summary of the insertion loss of all devices. The largest insertion loss contributors are the beam splitters and the mating sleeves. The beam path 493 nm laser take has in total 6 beam splitters and 9 mating sleeves, resulting in 14 dB insertion loss from beam splitters and 27 dB insertion loss from mating sleeves. It's no wonder that the beam preparation drawer yields no power output. The next section talks about the strategies we took to

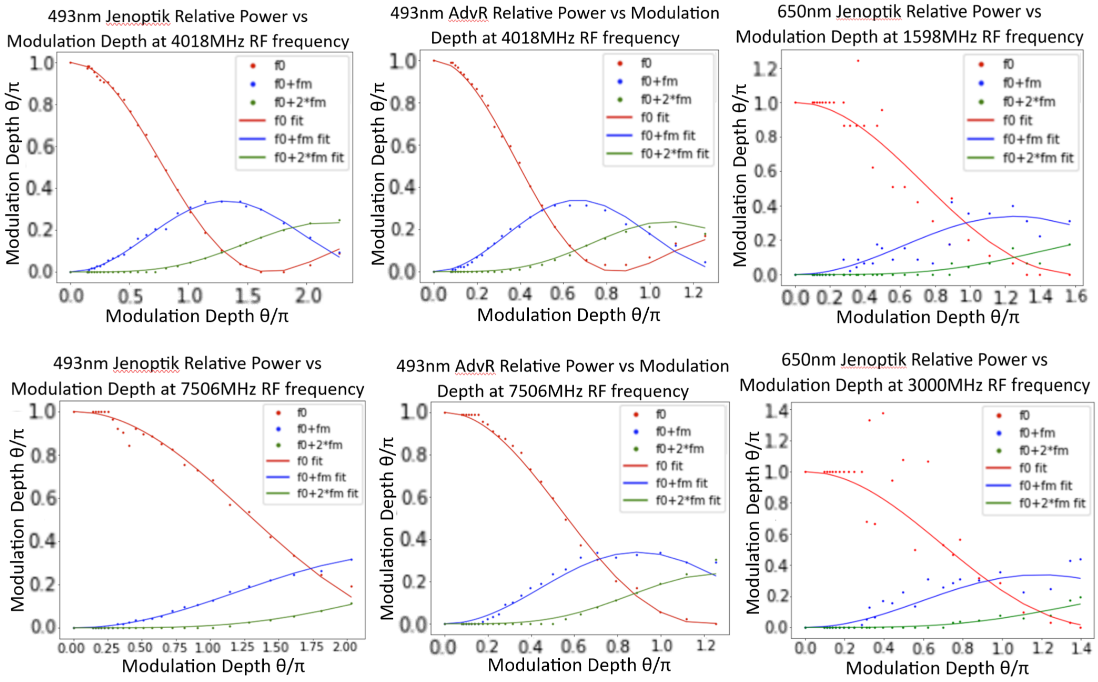

Figure 2.8: The modulation depth of the three EOMs under different RF frequencies. The modulation depth is directly related to the RF amplitude applied to the EOM. The red line, f_0, is the carrier frequency. The blue line is the first sideband, and the green line is the second sideband. The power is normalized to the peak carrier power. As the RF voltage increases, the modulation depth increases, the carrier power decreases, and the sideband power increases.

reduce the power loss.

2.3 Reduce Insertion Loss

Now the main source of insertion loss is identified, the plan for fixing the problem is straightforward. First, minimize the use of beam splitters and mating sleeves in the system. This involves temporarily disassembling the entire system setup and retaining only the essential components for the trapping test. Second, reduce the insertion loss for each component. Among these components, the most crucial is the insertion loss of the mating sleeves, as its quantity remains significant even after streamlining the setup.

Component.	Insertion Loss (dB)
Fiber	0.94
Laser Source to coupling	6.2
Collimator	3
Beam Splitter	2
Red Green Blue (RGB) Combiner	3.4
Mating Sleeve	4.69
AOM	3
EOM	6.02
Doubler(with 27 mW input power)	18.2
Optical board	1.6

Table 2.4: A summary of the insertion loss of each component.

2.3.1 Optical Path Design

The original design includes components that are unnecessary for the trapping test. For instance, in the 493 nm path, as shown in Fig. 2.1, beam splitters are placed after each component to monitor the laser power. The beam is initially sampled to feed the wavemeter, which locks the laser frequency. The laser from the EOM is directed into a cavity to monitor frequency sidebands. The laser is then split into three paths for three different optical boards. However, for the trapping test, only one board is required. All of these are not necessary for the trapping test. Only one board is needed for the trapping test, so only one path is needed. Therefore, all monitoring paths are removed. The new design only has one 493 nm path, one 650 nm path and one 553 nm path. However, I split 650 nm into two because we have enough power to do so. The adjusted beam path for 493 nm, 532 nm, and 650 nm lasers are shown in Fig. 2.9.

493 nm Beam Preparation Path

The 493 nm laser begins by sampling 1% of its power for the wavemeter, creating a feedback loop that locks the laser frequency. Afterward, it goes through the EOM, AOM, and combiner before entering the loading board, as illustrated in Fig. 2.9. The fibers are connected using a fiber mating sleeve.

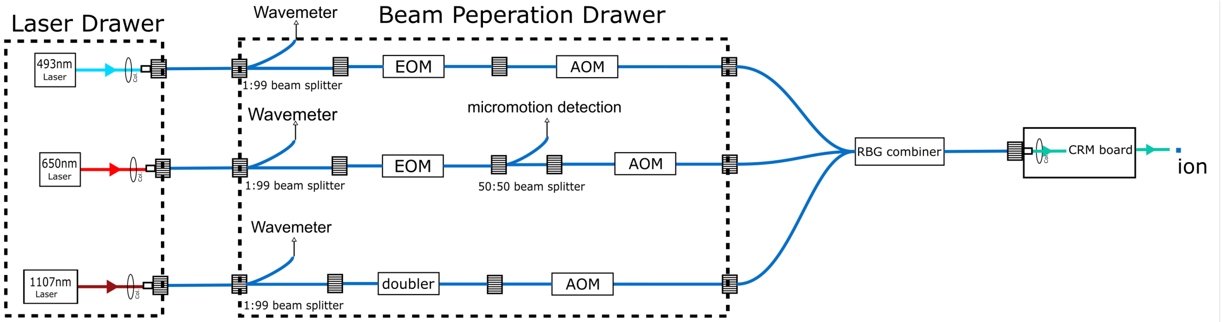

Figure 2.9: The new design of the 493 nm, 532 nm, and 650 nm path are much more simple. The wavemeter samples each laser through a 1 : 99 beam splitter and then locks laser frequency through a feedback loop. The 1107 nm laser's frequency is doubled to generate a 532 nm laser. The 650 nm laser split an extra path because we have sufficient power for it.

650 nm Beam Preparation Path

The 650 nm laser path is exactly the same as the 493 nm laser path except for the 50 : 50 beam splitter after the EOM. The extra path is reserved for micromotion detection. Micromotion detection is not related to this thesis; this path was reserved because we have sufficient power to do so.

553 nm Beam Preparation Path

Different from the previous two paths. A doubler is used to generate 553 nm laser from 1107 nm laser before being modulated.

2.3.2 Mating Sleeves

The mating sleeve was improved with the index-matching gel. The gel can effectively remove any air gap between two fiber tips and improve transmission. It reduced the insertion loss of the mating sleeves from 4.69 dB to 1.1 dB.

2.3.3 Results

With an initial power of approximately 70 mW from the laser source, the 493 nm laser achieves a power of 132.87 μW at the target, and the 650 nm laser reaches 123.6 μW at the target, both surpassing the necessary levels. Unfortunately, the 1107 nm laser had a mode hopping issue and had to be sent back to the manufacturer for repair, preventing the verification of its power output.

2.4 Unresolved Problems

Three significant problems affecting power output remain unresolved. The first issue is with fiber coupling, where a majority of the laser power fails to couple with the fiber. This inefficiency results from the divergence of the laser. The laser divergence was larger than expected, causing the beam to clip on optical elements, resulting in power loss, as depicted in Fig. 2.10.

The second unresolved problem is the insertion loss of all other components. Especially the beam splitters. The monitoring paths are removed temporarily, but they are still needed to provide remote system monitoring. Therefore, a more efficient way to monitor the laser power and frequency and a more efficient way to sample the laser are needed. The third problem is the mode hopping issue of the 1107 nm laser. It resulted in inconsistent power output from the 1107 nm laser and was returned to the manufacturer for repair.

2.5 Conclusion and Outlook

In this chapter, I focused on optimizing the power of the optical system and successfully delivering enough power to the ions (> 100 μW). It is achieved by removing unnecessary beam paths to reduce the number of beam splitters and mating sleeves present in the beam path. The fiber-based optical system is advantageous in making the optical system modular. The modular property allows us to utilize space more efficiently by moving laser sources from the optical table to a rack. However, a fiber-based optical system poses a challenge in maintaining a low insertion loss. We have observed power fluctuation by tapping the fiber. Temperature changes also showed effects on power fluctuation. Thus, during future upgrades, maintaining temperature and reducing vibration on fiber are recommended.

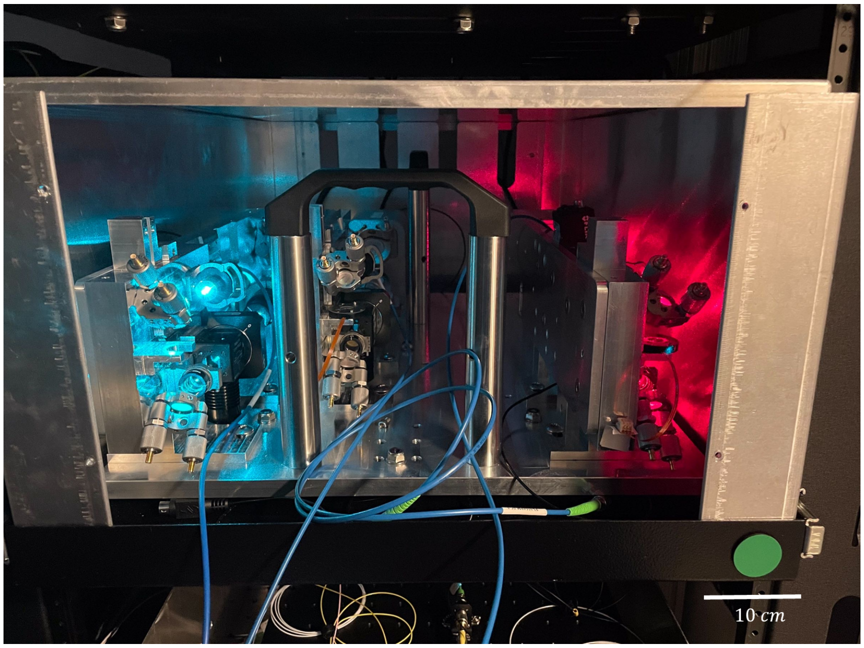

Figure 2.10: An image of the laser drawer. On the left is the 493 nm path. On the right is the 650 nm path. The optical elements are mounted on the customized baseboards. We should not see it glowing like this. It means the laser clipped on optical elements, and most of the light did not enter the fiber.

Chapter 3

Laser Beam Delivery System

Chapter 2 covered the discussion on the required laser power at the ions. This chapter will primarily address the delivery of the laser to the ions. It is essential to distribute laser intensity uniformly across all 16 ions to ensure consistent operations. However, enlarging the beam size indefinitely is not feasible because the laser would clip onto the trap's surface and increase background noise. Additionally, merely adding filters is not sufficient to reduce background noise, as one of the laser frequencies coincides with the ion fluorescence frequency. Consequently, the beam needs to be shaped to avoid clipping onto any mechanical structure while ensuring uniform coverage across all ions. The optical boards are specifically designed to shape the beams and focus them onto the ions. Hence, two critical parameters of the optical boards that need to be assessed are the beam shaping ability and the amount of laser clipping on the trap's surface.

My contributions to beam shaping are as follows:

1. I aligned the optical components to achieve the desired beam waist.
2. I took the beam profiles to confirm the beam waist.
3. I took High Dynamic Range(HDR) intensity profiles to confirm the laser does not clip too much power on the trap surface.

The section 3.1 will introduce the optical table layout and the specific optical boards I worked on. The section 3.2 explains the beam shape requirement. The section 3.3 shows how shaping is done on each optical board. The section 3.4 reports the measured results. I want to acknowledge Ali Binai-motlagh, who taught me how to adjust the beam shape,

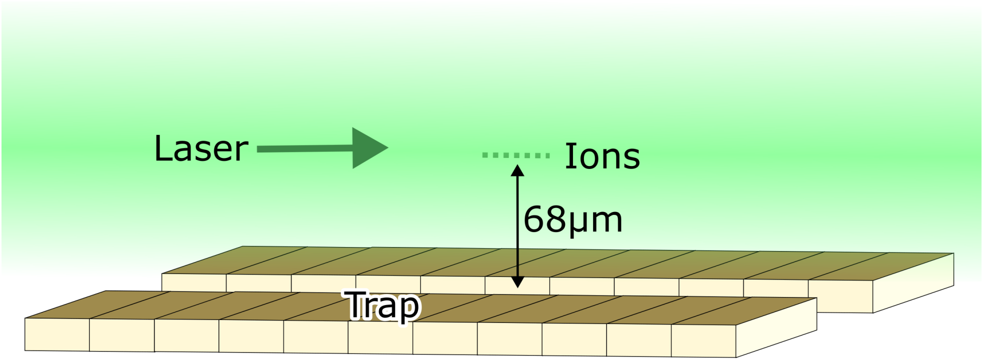

Figure 3.1: A sketch of laser propagating across the trap. The green light indicates the laser addressing the ion. Despite being focused on the ion, some laser power would still clip on the trap's surface.

take beam profile using a scanning slit beam profiler, and perform HDR profiling using the Python code he wrote. Ali has also characterized part of the system, which I will acknowledge again later in the chapter. I also want to acknowledge Noah Greenberg, Stephen Del Grosso Milek, Mark Elliott Wallace, and former labmates for system design and assembly.

3.1 The Optical Table Layout

The optical table layout is shown in Fig. 3.2. Four optical boards were used to deliver lasers to the ions: Loading, Cooling Repumping Measurement(CRM), Optical Pumping, and Shelving board. Each board holds one to two beam paths. Each beam path is named after the optical board it passes through. The trap has been split into loading, quantum, and storage zones. By design, the ions are trapped in the loading zone and then shifted to the quantum zone to perform quantum operations. We could also shift the ions to the storage zone if they don't participate in quantum operation. The separation between the two zones is about 1mm. The loading path and the photoionization path were pointed to the loading zone. The CRM lasers are pointed to the quantum zone. The storage zone is free of lasers.

Among the four optical boards, three are tested. The shelving board was not tested

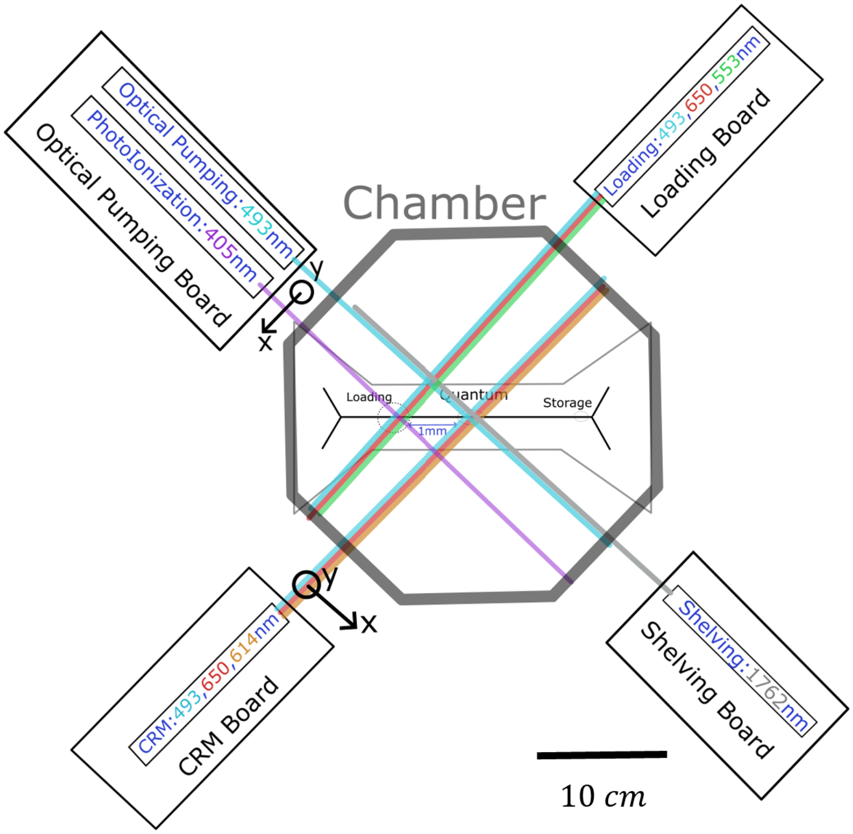

Figure 3.2: An off-scale sketch of the trap, chamber and optical boards. The trap has been split into the loading, quantum, and storage zones. The separation between the loading and the quantum zone is 1mm. The four optical boards are CRM, loading, optical pumping, and shelving boards. The CRM and the Shelving board address the quantum zone. The loading board addresses the loading zone. The 405 nm laser on the optical pumping board addresses the loading zone, and the 493 nm laser addresses the quantum zone. The x and y axes denote the orientation of each laser when taking beam profiles.

because the laser had not been purchased yet. On the CRM board, the 493 nm beam is used to measure and cool ions, and the 650 nm lasers repump ions from metastable states to excited states. The 553 nm laser on the loading board and the 405 nm laser on the optical pumping board performs two-step photoionization. The 553 nm drives the specific isotope from the $6s^{2}\,^{1}S_0$ state to the $6s6p\,^{1}P_1$ state. Then, the 405 nm laser excites an electron into the continuum.

Each board has a telescope that shapes the beam to the desired size. Fig. 3.3 shows an image of the beam shaping telescope, and Fig. 3.4 shows the optical schematic of the CRM board. Lasers on the same board pass through the same telescope. We are putting different wavelengths through the same lens; thus, chromatic aberration needs to be considered. Therefore, achromatic lenses were used to reduce chromatic aberration to an insignificant level [24]. I worked on the CRM, optical pumping, loading, and photoionization telescopes. Nonetheless, I worked with Ali Binai-motlagh on this project. He also characterized the optical pumping board and the loading board. A more specific contribution is described in the "Telescope Design" section.

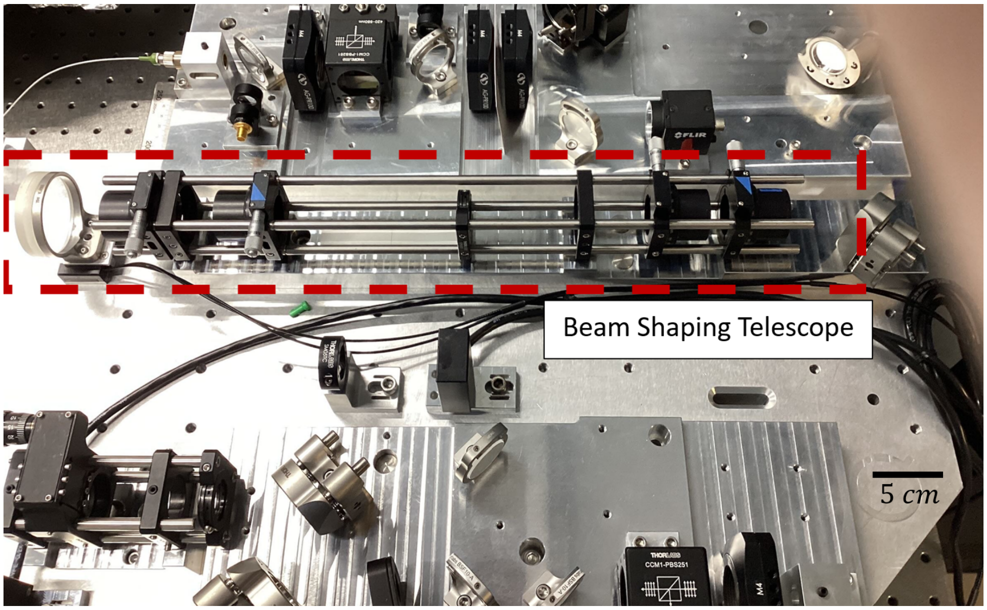

Figure 3.3: An image of the optical board. The red dotted block highlights the beam-shaping telescope. Two pairs of cylindrical lenses are mounted on the cage system. The focusing lens is on the left side of the telescope.

3.2 Beam Requirements

Addressing all 16 ions with uniform intensity is important for all global operations. The beams we use are single-mode Gaussian beams. The intensity drops exponentially with

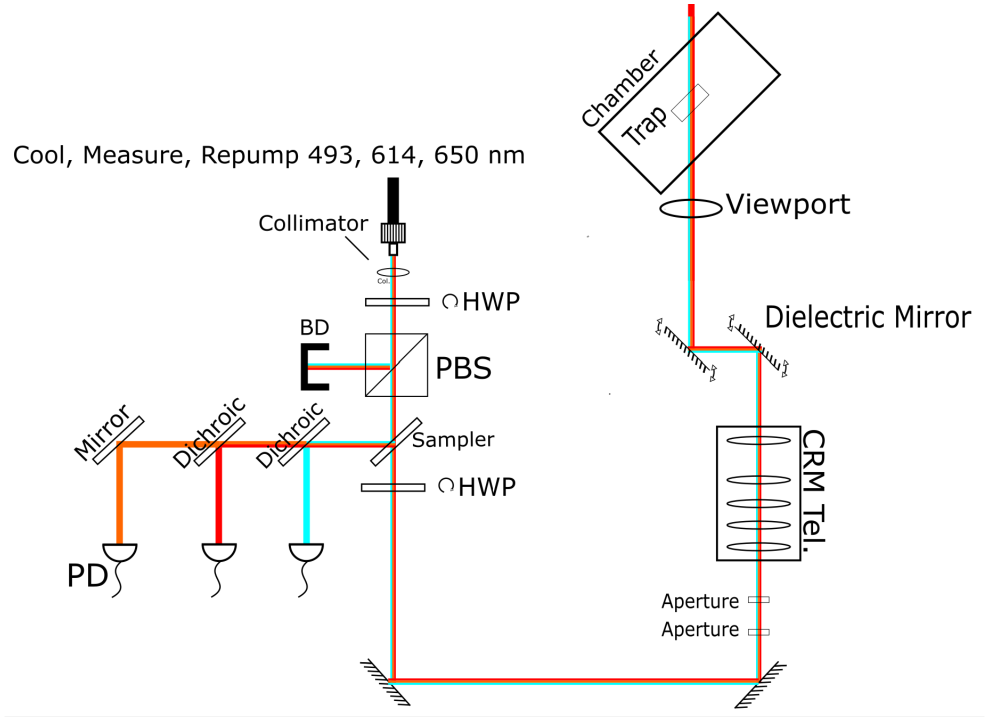

Figure 3.4: An optical schematic of the CRM board. The photodiodes(PD) monitor the power of each laser. The HWP and the BPS sets control the laser power.

respect to the square of radius. The ions on the edge of the ion chain would experience less intensity. To address this issue, we want to reach saturation intensity on all 16 ions. Therefore, 95% of the laser intensity should cover all 16 ions. We also do not want the laser to clip on the trap's surface. The 493 nm is the wavelength we used to probe ions and also the wavelength for ion detection. Therefore, filtering wavelength will not reduce the background noise induced by the 493 nm laser. Thus, to reduce the background noise, we must shape the beam so as not to clip on the trap. We want the beam to be $< 10^{-3}$ of the peak power. Consider the assumption that ions are spaced evenly at 4 μm, and the beams are at 45° angle to the ion chain; the beam waist should be bigger than 200 μm. However, cross-contamination of laser-addressing the neighbouring zone should also be limited. Therefore, the beam waist should be smaller than 240 μm. The intensity of the Gaussian beam is:

$$I_{(r)} = \frac{2P}{\pi\omega_0^2}\exp(\frac{-2r^2}{\omega_0^2}) \tag{3.1}$$

$$\omega_0^2 = \frac{z_{\mathrm{R}}\lambda}{\pi} \tag{3.2}$$

where P is the power, ω_0 is the beam waist, r is the distance to the center of the beam, z_R is the Rayleigh length, and λ is the wavelength. We normalize the laser intensity to the peak intensity, $\frac{2P}{\pi\omega_0^2}$. The intensity at the neighbouring zone ($r = 707$ μm) is $\sim 10^{-8}$ of the peak intensity. The ions are levitated about 68 μm above the trap surface. To prevent the trap surface from scattering too many photons, the beam waist along the normal of the trap surface should be less than 22 μm. In this case, the intensity at the surface of the trap ($r = 68$ μm) is $\sim 10^{-9}$ of the peak intensity. The Rayleigh length of the beam sets the lower limit of the beam waist along this direction. Since the beam waist is inversely proportional to the Rayleigh length, the beam might clip on the edge of the trap if the Rayleigh length is shorter than the length of the beam crossing the trap. The length of the beam crossing the trap surface is 990 μm. Using equation 3.2, the Rayleigh length of the beam is $z_{\mathrm{R}} = 1841$ μm if the beam waist is 17 μm. In conclusion, the beam should be shaped to ellipse with a radius $x \approx 200-240$ μm and $y \approx 17-22$ μm for all wavelengths we use except 405 nm laser. The 405 nm laser is used for the second step of photoionization. There is no need to expand it to cover 16 ions, so the desired shape is a circle with a radius of ~ 19 μm, which will not clip on the surface of the trap or induce cross-talk to the neighbouring zone. The intensity at 1mm away

3.3 Telescope Design

3.3.1 CRM and Optical Pumping Path Telescope

The CRM and the loading board must focus the beam to an ellipse shape. It can be achieved through two sets of achromatic cylindrical lenses that address the x and y-axis differently. For each direction, the two lenses expand or shrink beam size accordingly. Lastly, a lens with a 300 mm focal length will focus the beam to the ions. The x-axis cylindrical lenses will shrink the beam; hence, the beam expands to the desired shape after the focusing lens. The y-axis cylindrical lenses will expand the beam; hence, the beam shrinks to the desired shape after the focusing lens, as shown in Fig. 3.5. The final beam size depends on the distance between two cylindrical lenses, and the angle between the two lenses should be perfectly perpendicular.

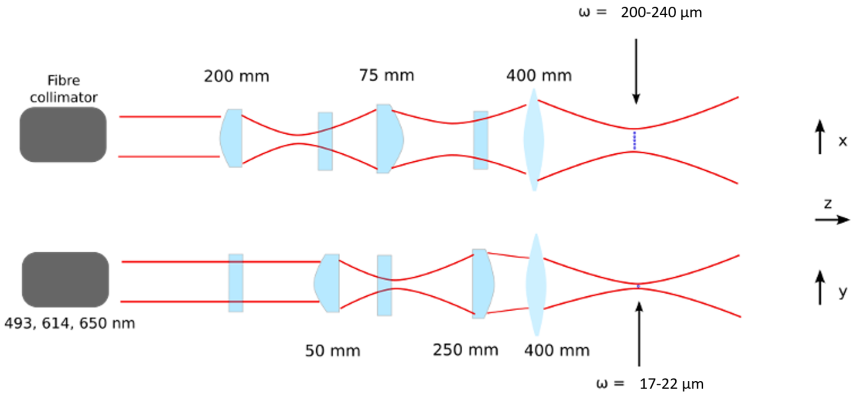

Figure 3.5: The lens system on the CRM and Optical Pumping path viewed from two perpendicular directions. The cylindrical lenses are convex along one axis and flat along the perpendicular axis. The focal lengths of each lens are labelled near the lens. ω denotes the beam radius at the focus along a specific direction [14].

3.3.2 Photoionization Telescope

The photoionization board needs to shrink the beam. Therefore, we use two spherical lenses to expand the beam and then focus it down to the desired shape with the third lens, as shown in Fig. 3.6. The final beam radius depends on the distance between the spherical lenses.

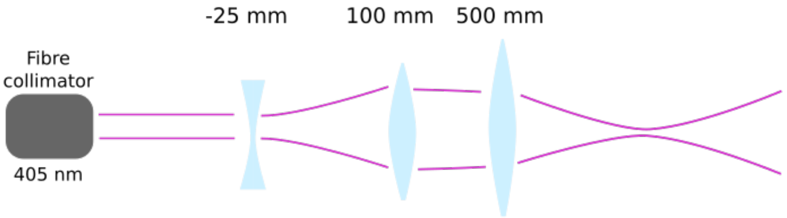

Figure 3.6: The lens set of the 405 nm laser. The focal lengths of each lens are labelled near the lens [14].

3.4 Results

The beam profiles are taken by the DataRay's Beam'R2 – XY Scanning Slit Beam Profiler. The beam radius is determined by $1/e^2$ of peak intensity. The intensity profile is measured through HDR profiling. The HDR profiling is a function that stitches the images of the laser taken at different exposure times into one complete intensity profile. The experiment setup is as shown in Fig. 3.7.

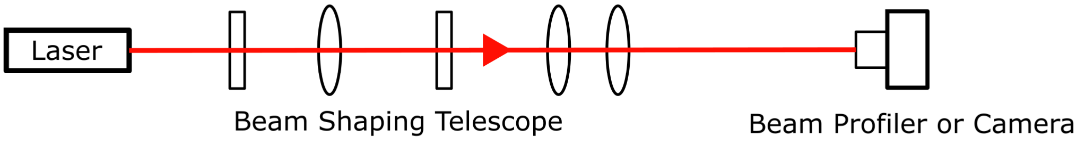

Figure 3.7: A sketch of the experiment test setup. The sketch is reduced to the laser source, telescope, and detecting device (Beam Profiler or Camera).

3.4.1 The CRM Path

A 493 nm laser is used to test the telescope. The beam profile of the CRM telescope is shown in Fig. 3.8. The beam width along the x-axis is 242 μm, and the beam width along the y-axis is 20.4 μm. The profile shows some bumps that could be caused by laser clipping on the lenses. The intensity profiles along the two axes are shown in Fig. 3.9. It shows we are clipping 4×10^{-3} of the peak intensity on the trap surface and less than 10^{-5} of the peak intensity to the loading zone, which is acceptable.

3.4.2 The Optical Pumping Path

The beam profile of the optical pumping telescope measured with the 493 nm laser is shown in Fig. 3.10. The beam width along the x-axis is 222 μm, and the beam width along the y-axis is 16.3 μm. The intensity profiles along the two axes are shown in Fig. 3.11. The intensity at the trap's surface is about 4×10^{-3} of the peak intensity. The intensity at the loading zone is less than 10^{-3} of the peak intensity, which is acceptable.

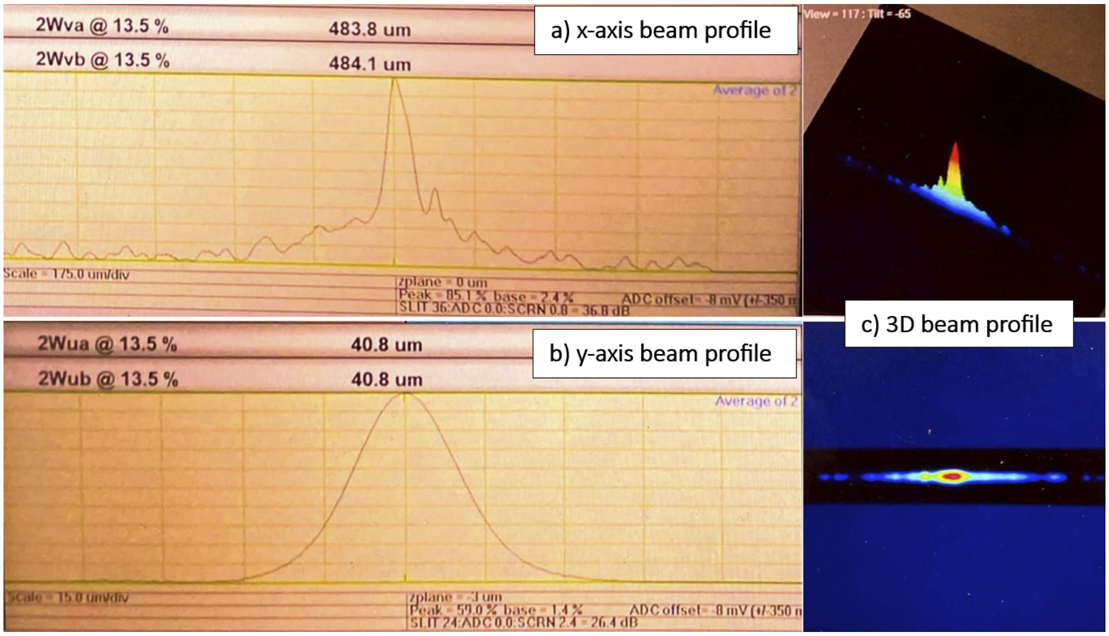

Figure 3.8: The beam profile of the 493 nm at the focus of the CRM telescope. a) shows the beam diameter along the x-axis is 483.8 μm, and b) shows the y-axis is 40.8 μm. c) is a 3D beam profile of the laser.

3.4.3 The Loading Path

I would like to acknowledge Ali Binai-motlagh for optimizing and characterizing this path. He took both the beam profile and the HDR intensity profile of this path. I have also taken the beam profile, but I did not take the HDR intensity profile. The beam profile shown in Fig. 3.12 was taken by me. The HDR intensity profile shown in Fig. 3.13 is taken by Ali Binai-motlagh. The figure shows that the beam width along the x-axis is 239.8 μm, and the beam width along the y-axis is 23 μm. The intensity at the trap's surface is about 4×10^{-3} of the peak intensity. The intensity at the loading zone is less than 10^{-3} of the peak intensity, which is acceptable.

3.4.4 The Photoionization Path

The beam profile of the photoionization path measured with the 405 nm laser is shown in Fig. 3.14. The beam waist is 18.8 μm. I would like to acknowledge Ali Binai-motlagh

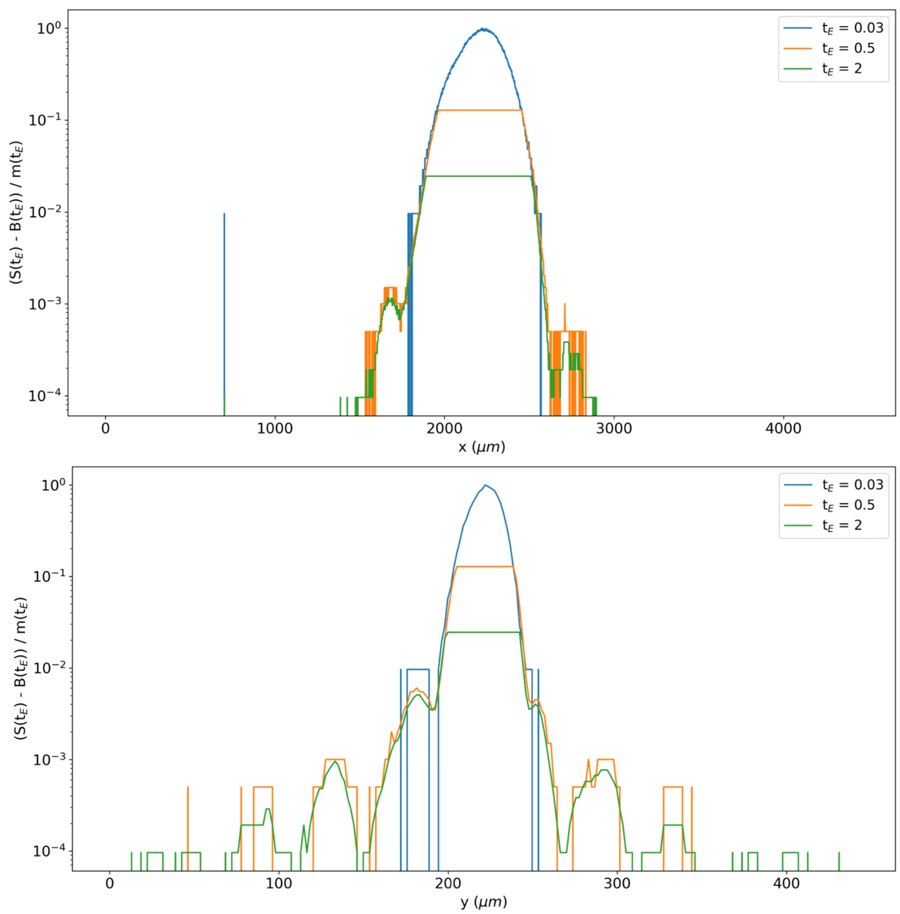

Figure 3.9: The HDR intensity profile of the laser at the focus of the CRM board. The vertical axis denotes the intensity normalized to the peak intensity. The horizontal axis denotes the position along the x or the y axis. t_E is the exposure time of the camera, $S_{(t_\mathrm{E})}$ is the maximum intensity measured at exposure time, $B_{(t_\mathrm{E})}$ is the average background intensity measured at exposure time, and $m_{(t_\mathrm{E})}$ is the adjustment factor. It shows beam intensity drops to 4×10^{-3} of the peak intensity at 68 μm along the y-axis and to $< 1 \times 10^{-5}$ of the peak intensity at 707 μm along the x-axis.

for taking the intensity profile, as shown in Fig. 3.15. The intensity at 68 μm has reached background noise.

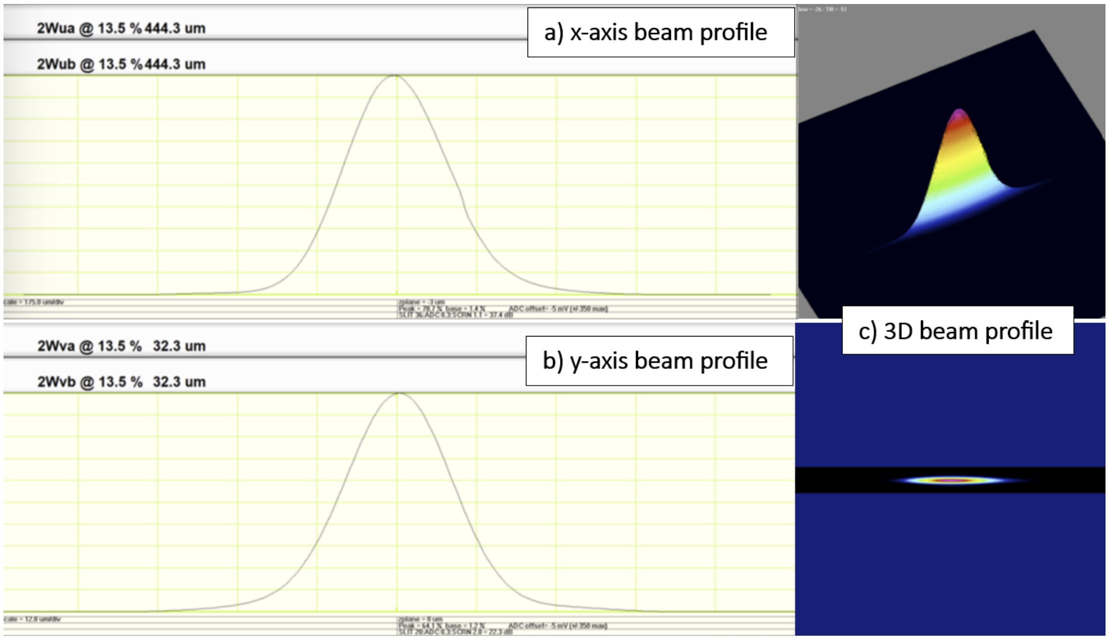

Figure 3.10: The beam profile of the 493 nm at the focus of the optical pumping telescope. a) shows the beam diameter along the x-axis is 444 μm, and b) shows the y-axis is 32.3 μm. c) is a 3D beam profile of the laser.

3.5 Conclusion

In conclusion, the ability to shape the beam has been verified for each optical board. Even though we could still work with the amount of laser clipping on the trap's surface, the measured intensity is much higher than the calculated intensity. It makes sense since the intensity profile is not perfectly Gaussian. Multiple small bumps appeared near the peek, indicating the laser was clipping somewhere along the path and inducing an interference pattern. To address this issue, larger cylindrical lenses are needed. However, this requires redesigning the cage system of the telescope because the current cage system is specific to the current lens size. Machining new pieces might be necessary. In addition, the current system does serve the purpose of trapping an ion. Hence, an upgrade will be delayed until after the trapping test. Another test that should have been done is to test the chromatic aberration of the system. It could be done by measuring the beam size of each laser at a fixed distance. The chromatic aberration test can help us rule out a potential factor when a problem shows up later.

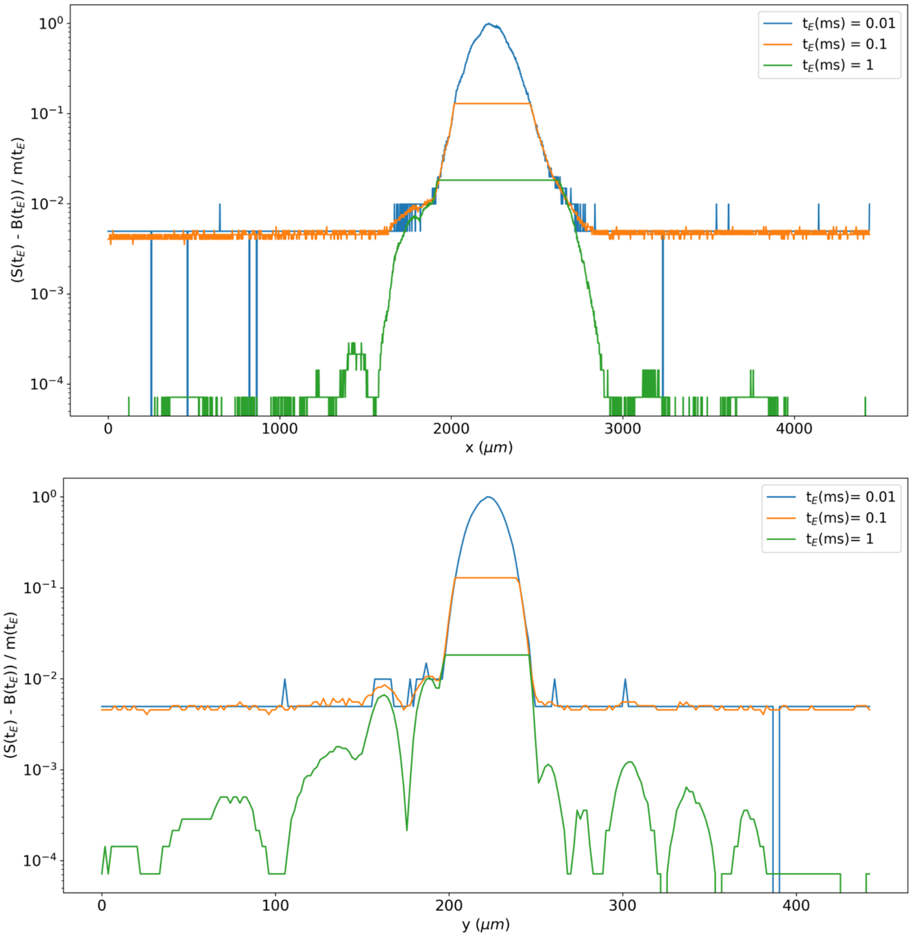

Figure 3.11: The HDR intensity profile of the laser at the focus of the CRM board. The vertical axis denotes the intensity normalized to the peak intensity. The horizontal axis denotes the position along the x or the y axis. t_{E} is the exposure time of the camera, $S_{(t_{\mathrm{E}})}$ is the maximum intensity measured at exposure time, $B_{(t_{\mathrm{E}})}$ is the average background intensity measured at exposure time, and $m_{(t_{\mathrm{E}})}$ is the adjustment factor. It shows beam intensity drops to 4×10^{-3} of the peak intensity at 68 μm along the y-axis and to $< 1 \times 10^{-3}$ of the peak intensity at 707 μm along the x-axis.

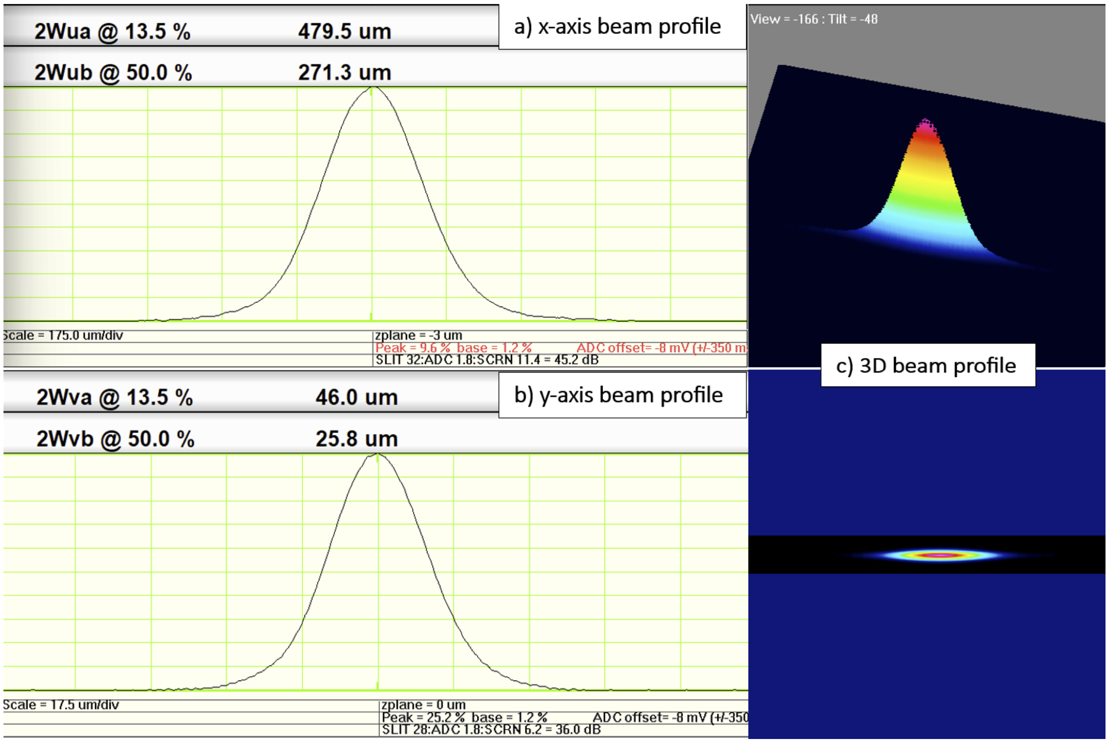

2Wua @ 13.5 % 479.5 um

2Wub @ 50.0 % 271.3 um

Scale = 175.0 um/div

zplane = -3 um

Peak = 9.6 % base = 1.2 % ADC offset= -8 mV (+/-350 m

SLIT 32:ADC 1.8:SCRN 11.4 = 45.2 dB

2Wva @ 13.5 % 46.0 um

2Wvb @ 50.0 % 25.8 um

Scale = 17.5 um/div

zplane = 0 um

Peak = 25.2 % base = 1.2 % ADC offset= -8 mV (+/-350

SLIT 28:ADC 1.8:SCRN 6.2 = 36.0 dB

Figure 3.12: The beam profile of the 4 nm laser at the focus of the loading telescope. a) shows the beam diameter along the x-axis is 479.5 μm, and b) shows the y-axis is 46 μm. c) is a 3D beam profile of the laser.

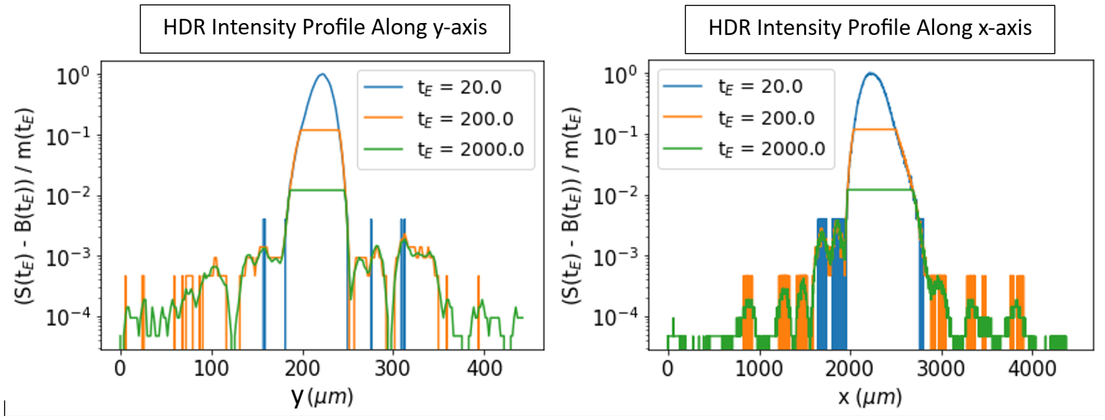

Figure 3.13: The HDR intensity profile of the laser at the focus of the CRM board. The vertical axis denotes the intensity normalized to the peak intensity. The horizontal axis denotes the position along the x or the y axis. t_{E} is the exposure time of the camera, $S_{(t_{\mathrm{E}})}$ is the maximum intensity measured at exposure time, $B_{(t_{\mathrm{E}})}$ is the average background intensity measured at exposure time, and $m_{(t_{\mathrm{E}})}$ is the adjustment factor. It shows beam intensity drops to 1×10^{-3} of the peak intensity at 68 μm along the y-axis and to $< 1 \times 10^{-3}$ of the peak intensity at 707 μm along the x-axis.

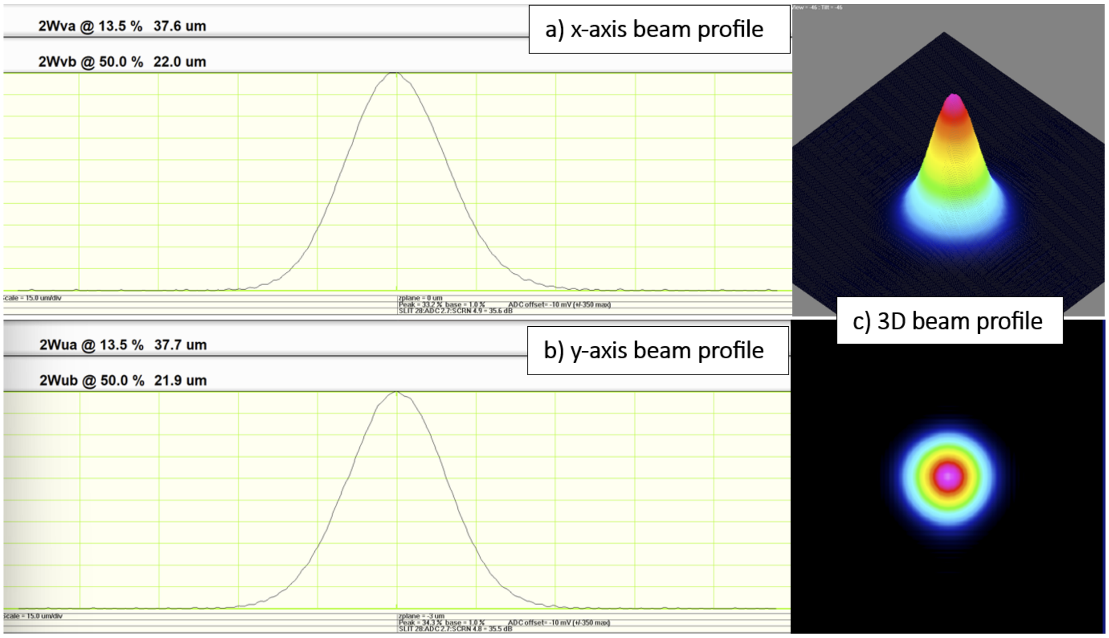

Figure 3.14: The beam profile of the 405 nm laser at the focus of the photoionization telescope. a) shows the beam diameter along the x-axis is 37.6 μm, and b) shows the y-axis is 37.7 μm. c) is a 3D beam profile of the laser.

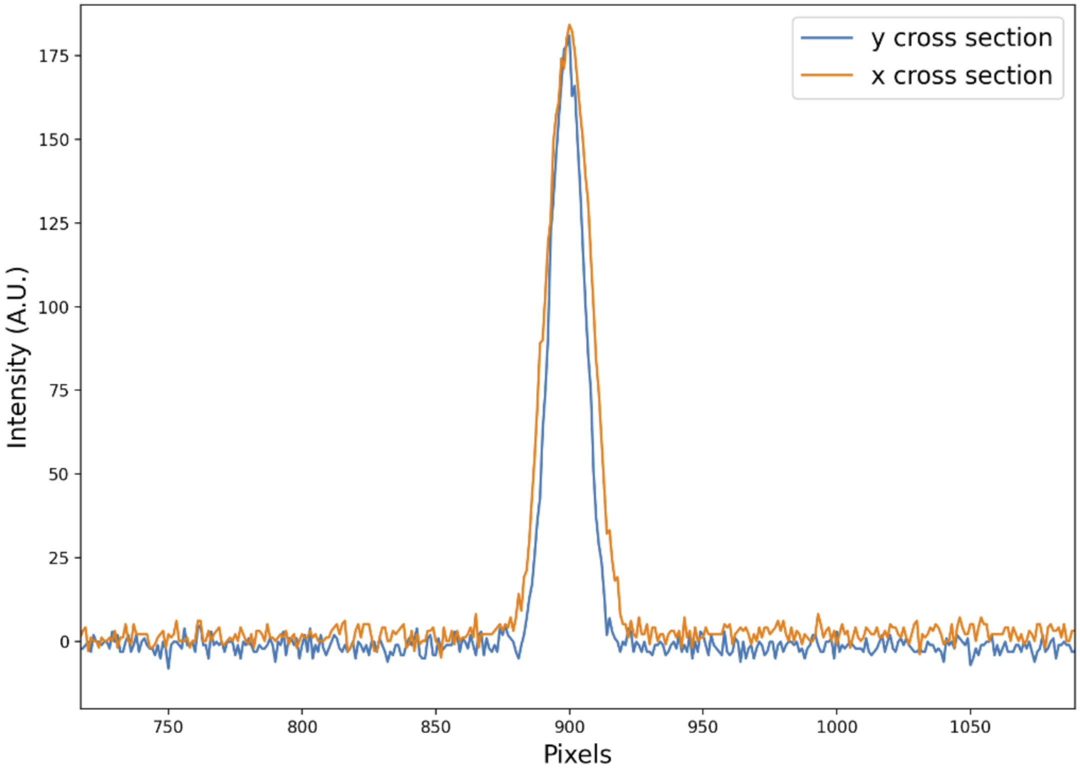

Figure 3.15: The intensity profile of the 405 nm laser measured at the focus of the photoionization telescope. The intensity unit is the arbitrary unit of the Charge-Coupled Device(CCD) camera. The pixel size is 4.68 μm. The 886 pixel is about 68 μm away from peak intensity and is close to background intensity.

Chapter 4

Validating Imaging System

The ability to observe ions is a critical requirement for trapping ions. This is done through the state measurement process, where a laser excites the ion and detects the ion's fluorescence. However, the ion's fluorescence is exceptionally faint, requiring the counting of individual photons. To accomplish this, PMTs are employed for photon counting. However,PMTs cannot distinguish the source of the photons, providing only a global photon count. To address this limitation, we utilize a scientific Complementary Metal–Oxide–Semiconductor(sCMOS) camera to capture images of the ions. However, there are no references to the positions of ions for us to calibrate the imaging system before an ion is trapped. Thus, we image the trap's surface instead. The ions are only 68 μm above the trap's surface. If we can image the trap's surface, we can image the ions by shifting the focus point from the trap's surface to the ion's position. The designed ion spacing is 4 μm(reasoning is explained in Chapter 6), but the pixel size of the sCMOS camera is 6 μm. Thus, two ions could be imaged into one pixel. Therefore, the image needs to be magnified so the camera can distinguish one ion from another. My contribution to this task is first to align the beam paths and take images of the trap's surface using the sCMOS camera. Then, the magnification of the lens system is calculated to confirm the camera can distinguish two ions. In section 4.1, the layout of the imaging valley is introduced. In the section 4.2, the result of beam path alignment and electrode imaging. I would like to acknowledge Ali Binai-motlagh, Mark Elliott Wallace, and Stephen Del Grosso Milek for assembling and testing the system before me, which provided valuable experience. And to Noah Greenberg and former labmates for designing the system.

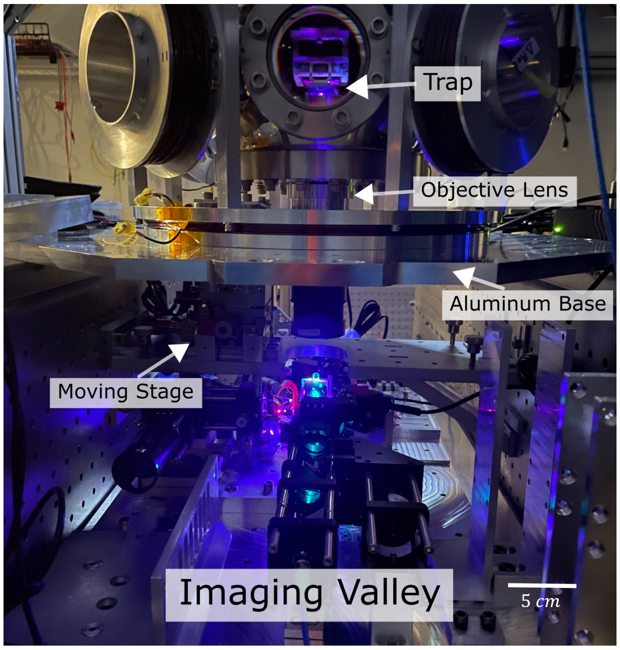

Figure 4.1: A photo of the imaging valley with the vacuum chamber.

4.1 Introduction of the Imaging Valley

The Imaging Valley is designed to collect the ion's fluorescence. The imaging system has two parts: The objective lens and the imaging board. The objective lens is mounted on a movable stage attached to the optical table, allowing displacement along all three axes and rotation along two axes. A shield is in place to prevent the lens from colliding directly with the viewport. The imaging board is placed in the valley of the customized optical table. It can move relative to the objective lens. This design of the imaging valley enhances stability and minimizes background noise. Fig. 4.1 shows a photo of the imaging valley. The Imaging board has four optical paths, as shown in Fig. 4.2. The 532 nm path collects the neutral fluorescence of Barium atoms. The 650 nm path delivers a 650 nm laser to measure micromotion. The Individual Imaging path is designed to measure photon counts from each individual ion using PMTs. The sCMOS path images the ion chain with a sCMOS camera. All paths have been installed at the current stage except the Individual Imaging path because it's unnecessary until we can trap multiple ions. My work is to align the imaging board and optimize the position of the objective lens so we can image the trap's surface on the Charge-Coupled Device(CCD) camera in the 532 nm path and the

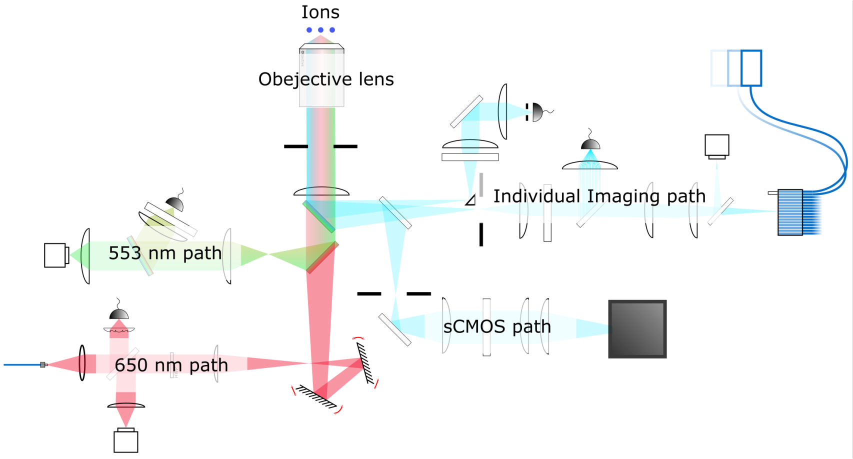

Figure 4.2: The four beam paths in the imaging valley. The objective lens collects the ion's fluorescence. The sCMOS path is designed to image the ions by detecting 493 nm light. The 553 nm path detects the neutral fluorescence from barium atoms. The 650 nm path is designed to detect the micromotion of the trapped ions; it is not currently in use. The individual imaging path is designed to match a PMT to each ion; it is not assembled. Adapted from [14]

sCMOS camera in the sCMOS path. Once we could image the trap's surface, we could move the objective lens 68 μm away to shift the focus from the trap's surface to the ions.

4.2 Alignment Results

4.2.1 Aligning the Imaging Board

The alignment of the imaging board is the first step, as the position of all optical paths is dependent on it. Lasers were used to assist alignment. Proper lasers were mounted at the position of cameras orPMTs. They propagate backward to the trap surface. The board is determined to be aligned when the trap surface reflects the lasers from all paths. A 650 nm laser is used to align the 650 nm path, a 405 nm laser is used for the 553 nm path, and a 493 nm laser is used for the sCMOS path. The beam reflected off the trap's surface is shown in Fig. 4.3, proving the imaging board is aligned.

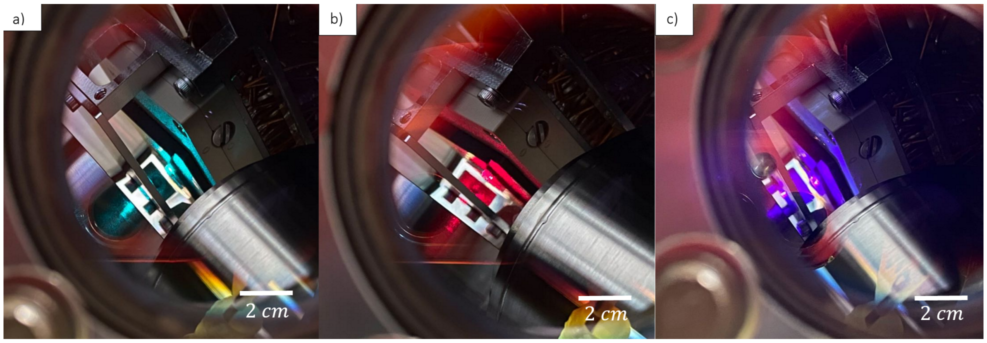

Figure 4.3: Lasers clipping on the trap, showing the beam paths are aligned to the trap. a) is the sCMOS path, b) is the 650 nm path and c) is the 553 nm path.

4.2.2 Aligning sCMOS path

The sCMOS path is the most important optical path that visualizes the trapped ions. A flip mirror is used to switch the detector between an sCMOS camera and aPMT, as shown in Fig. 4.4. Both the sCMOS camera and thePMT measure fluorescence from all Ions. To verify the alignment of thePMT path, a laser at the position of thePMT is directed to the trap's surface. The laser reflecting off the trap's surface confirms that thePMT is collecting light from the trap's surface.

Since the PMT only counts the number of photons, a perfect image of the trap on the PMT is not required. However, for the sCMOS camera, a clear image of the trap is needed to confirm the ability to observe ions. The designed ion spacing is about 4 μm, but the pixel size of the camera is 6 μm. Without magnification, it would be impossible to distinguish between two ions. Therefore, we have installed a lens system with a magnification of 6. This results in ion separations on the camera being about 4 pixels. Despite this, a spacing of 24 μm (equivalent to 4 pixels) is still quite narrow. If there were aberrations in the image or if the image was out of focus, we might not be able to see an ion. Therefore, the goals for the sCMOS path alignment are:

1. Obtaining a sharp image of the trap.
2. Calculating the magnification of the sCMOS path.

Because there was no light source inside the trap, a flashlight illuminated it. The best possible image with the sCMOS camera is shown in Fig. 4.5. The electrodes can be

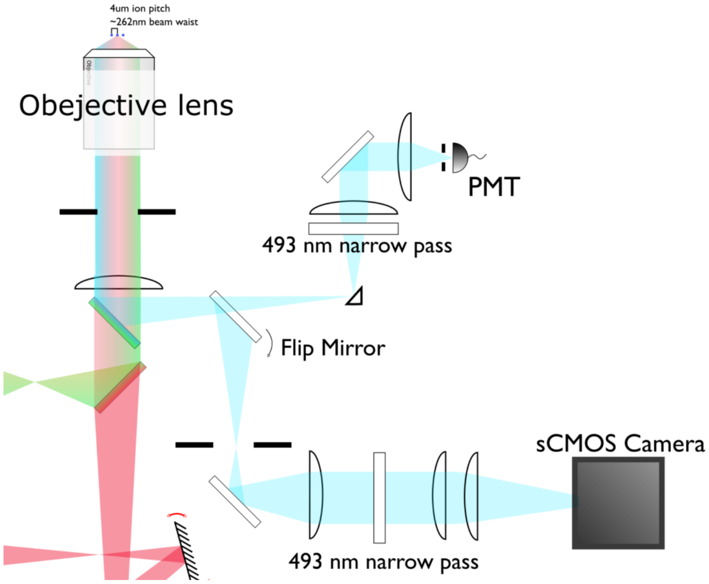

Figure 4.4: The detailed sCMOS path. The light is focused onto the sCMOS camera or the photodiode controlled by the flip mirror.

identified, but the image is not very sharp. However, we have moved the objective lens as close to the chamber as possible.

After verifying the dimensions outside the chamber were correct, we concluded that the trap was installed too far up in the chamber; it should be moved about 1 mm closer to the objective lens. By comparing the size of multiple electrodes on the image to its actual dimensions, the magnification of the sCMOS path is between 4.4 and 5. Even though it's lower than the desired magnification, we can still distinguish two ions. Even though the sCMOS camera could not focus on the trap's surface, it could still focus on the ions because the ions are 68 μm away from the trap's surface. We estimated the size of the electrodes if the focus is on the ions. The length of the electrodes will expand by 51 μm when the objective is focused 68 μm away from the trap's surface. However, the length of the inner electrodes is 77 μm[35], which means we won't be able to distinguish two electrodes if the focus is on the ions. Because we can distinguish two electrodes, the focus point did pass the position of the ions. Thus, we should be able to focus on the ions by moving the focus point away from the trap's surface. A sketch of the system is shown in Fig. 4.6. The magnification still needs adjustment. However, without a sharp image, we could not determine the magnification accurately.

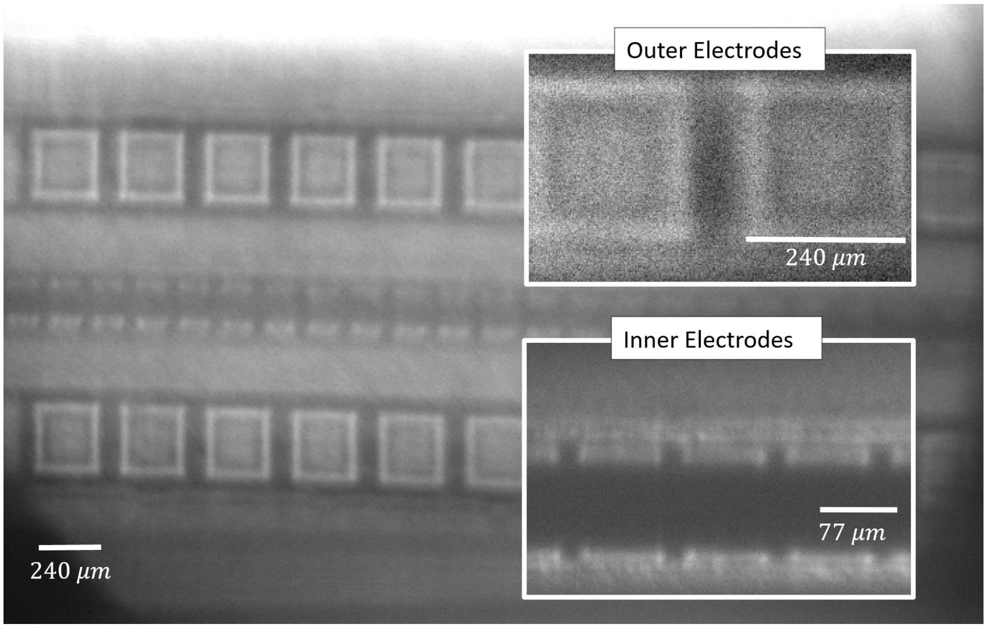

Figure 4.5: The image of the trap. We can resolve the inner electrodes and the outer electrodes.

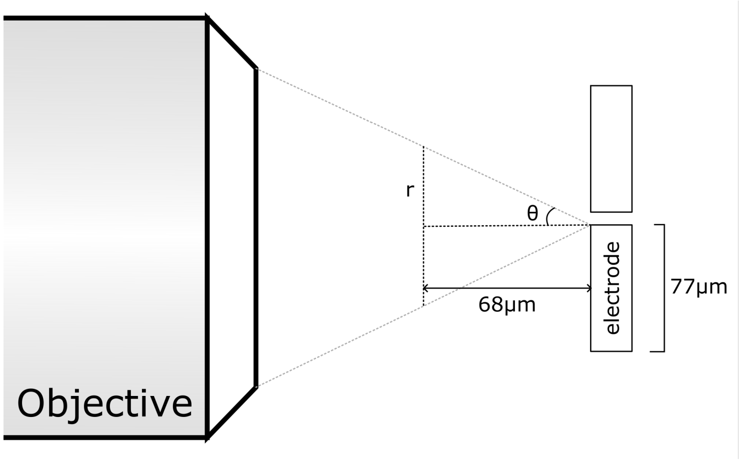

Figure 4.6: A sketch indicates how much will the inner electrodes expand if we focus on the ions.

4.2.3 Aligning the 553 nm Path

On the 553 nm path, a beam splitter splits light into two paths. One goes to the CCD camera, and the other to the PMT, as shown in Fig. 4.7.

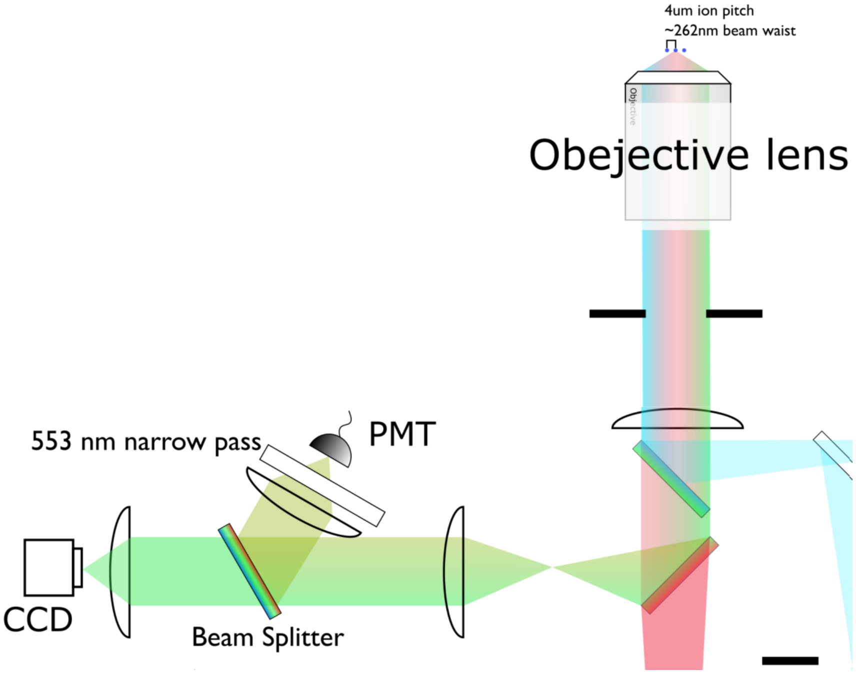

Figure 4.7: The detailed 553 nm path. The light is focused onto a CCD camera and the photodiode. The beam path is split by a beam sampler.

The 405 nm laser is placed where PMT is to illuminate the trap's surface, and the CCD camera is used to observe the image of the tarp. I imaged the trap onto the CCD camera, as shown in Fig. 4.8, but the camera was at the wrong distance. The designed position of the CCD camera is 20 cm away from the last lens; however, the camera was placed a few cm away from the last lens. This could mean that a wrong lens was installed or the positions of the lenses were wrong. However, we did not have access to the lenses at the time because the lead base plate of the chamber was in the way, and the chamber could not be removed because we were also performing tests on the chamber. In addition, we could still image the trap surface, and the PMT is aligned to count photon numbers. Therefore, the 553 nm still served the purpose and is not a blockade to testing the rest of the system. Thus, this issue will be addressed during the first big system update.

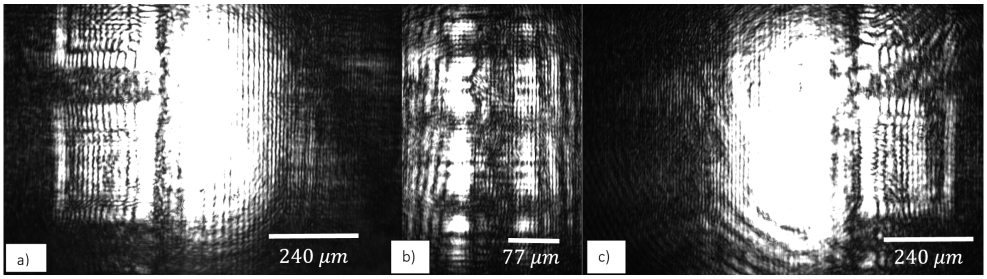

Figure 4.8: The electrodes on the trap that is imaged by the CCD camera. a) and c) are the outer electrodes. b) is the inner electrodes.

4.3 Conclusion

In conclusion, the alignment of the imaging system has been successfully completed. Images of the trap's surface have been captured. Although the sharpness of the electrode images could be improved, these images still prove the ability to focus on ions. We encountered two minor issues during this process, but they did not hinder our ability to confirm the presence of ions. The most significant challenge was the absence of a reference object within the vacuum chamber. Once the vacuum chamber is sealed, there are no illuminating objects at the ion's position except for the ions themselves. As a result, precisely adjusting the system to the position of the ions without any trapped ions is a complex task. Nevertheless, we identified the object closest to the ions to serve as our reference. This approach allowed the majority of the variables to be optimized, leaving only the position of the focus to be fine-tuned once an ion has been trapped. The next step in fine-tuning the imaging system will wait until we trap an ion.

Chapter 5

A Feasibility Study on Delivering Ablation Laser Via Multimode Fiber

Barium is an alkaline earth metal that has two valence electrons. Hence, barium ions can be generated when sufficient energy forces one of the valence electrons to leave the atom. This energy can be delivered in various forms. The photoionization process delivers the energy through a laser. However, this process is probabilistic and not efficient. So, a "swarm" of atoms is sent through the ionizing region in the hope of trapping one.

Atomic ovens are devices typically used to generate atoms inside a vacuum chamber. An atomic oven is usually a stainless steel tube with one opening pointing at the trap. A wire is wrapped around the tube, and the sample material is inside the tube. The electrically heated wire will increase the temperature of the bulk material and cause the material to sublimate. However, this process is not efficient as the sublimation continues after switching off the oven because the material takes minutes to cool down, leading to a waste of many atoms. Each run can sublimate atoms on the scale of 10^{15} atoms [40]. While the amount of waste is usually acceptable because the sample size is large enough, this is not the case for ^{133}Ba, which is radioactive. According to the Canadian Nuclear Safety Commission, the average public annual dose limit is 0.1mSv [17], which corresponds to about 5 μg of ^{133}Ba, about 10^{16} atoms. Therefore, it's crucial to reduce waste.

Laser ablation is a more suitable method for this purpose. It involves sending a short pulse laser (in a nanosecond or a picosecond scale) focus to a small spot about 100 μm in diameter on the sample. We also refer to this sample as the ablation target. Only the material inside the spot will sublimate due to the rapid heat transmission. Moreover, only the spot is heated, allowing the heat to dissipate quickly into the entire target after the pulse. Once the material inside one spot is depleted, the laser focus moves to a different spot on the target or even a spot on a different target and continues ablation. This process achieves on-demand ablation and saves materials in each ablation.

A free-space optical system that delivers an ablation laser was successfully built and tested previously in our laboratory. The sample we use is in salt form ($BaCl_2$). We did not use metallic barium because ^{133}Ba is synthesized through nuclear reactions. It does not exist in metallic form. The target we used for initial setup and diagnostic was ^{138}Ba instead of ^{133}Ba because ^{138}Ba is naturally abundant and non-radioactive, making it easier to obtain and safer to operate. To observe the atoms, a 553 nm laser was used to excite the fluorescence of the neutral ^{138}Ba atoms. A manuscript which I co-authored that will report this success, will be available soon. From the experiment, we learned the parameters of the laser that generate measurable plumes of atoms per ablation. In estimation, a 5 μg $BaCl_2$ target can be ablated about $250,000$ times. Assuming that 1 ion can be trapped per ablation and we trap 100 ions each day, one target can be used for 7 years. Comparing the lifetime of one target (7 years) to the half-life of ^{133}Ba (10 years), there is no need to further extend the lifetime of a target. The laser's center wavelength is 532 nm, and the pulse width is < 1 ns. The laser is focused to approximately 100 μm in diameter. The repetition rate has no strict limits. I set the repetition rate to 1 kHz for more continuous energy measurement. The fluence at the target should be 0.57J/cm^2 [42]. Fluence is a measurement of energy density.

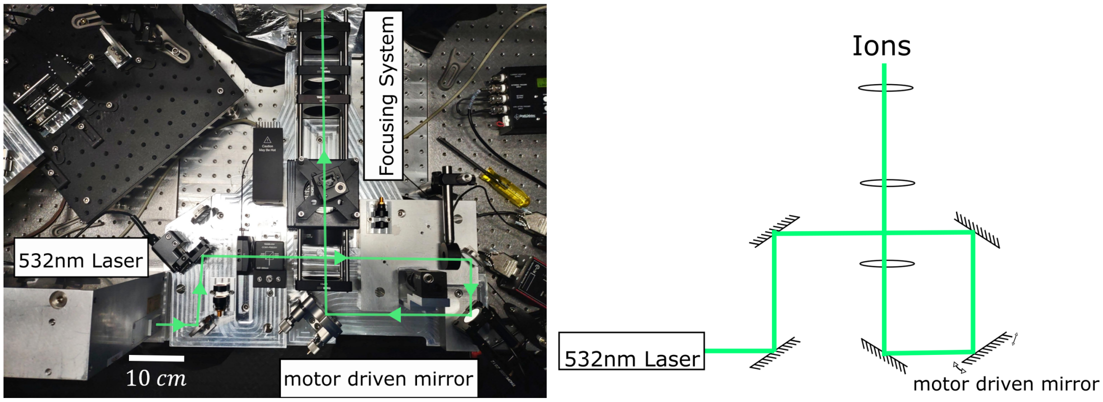

Figure 5.1: An image of the ablation board. The ablation board combines the laser source and the focusing system on one solid custom-designed optical board. Motor-driven mirrors shift the focus point. The green line indicates the beam path.

The ablation board is depicted in Fig. 5.1. The ablation board has both the laser source and the focusing system mounted on a single custom-made aluminum board. Unlike the optical boards I introduced in previous chapters, this setup is not as modular as other boards. A modular system would allow us to change the laser to a different brand with a different size without interfering with the focusing system. A modular system also allows moving the laser source off the optical table to save space on the optical table for other optical components.

To make the current ablation system modular, we envision a fiber-based ablation solution. This solution proposes splitting the ablation board into two parts: a laser source and a focusing system connected through a fiber. This would make replacing any components less impactful on the other components. Ideally, the entire focusing system will be small enough to be mounted on a three-axis moving stage, allowing us to maintain the quality of the beam while changing the ablation spot.

Delivering an ablation laser through the optical fiber is not a new idea. It is used in the biomedical field. The two sources report positive results on delivering ultra-short pulse laser (< 10 ps) [18, 27]. My teammate Monica also reported a positive result on delivering an ablation laser through a single-mode fiber [45]. However, her target is ytterbium metal. The ionic bonds in barium salt are stronger than the metallic bonds in ytterbium metal, which means more energy is required to ablate barium salt. As a result, we are considering the use of multimode fiber. Multimode fibers have larger core diameters than single-mode fibers, allowing them to transmit more energy.

I am responsible for conducting the feasibility study and test sending ablation laser through multimode fiber. My contributions are as follows:

1. I theoretically checked the feasibility of the multimode solution and designed a system based on the calculation.
2. I experimentally tested the system and obtained a negative result due to a much lower damaging threshold than calculated.
3. I analyzed the experiment data and proposed a new design.

In section 5.1, I evaluated that a fibre with a 10 μm diameter fibre core and a numerical aperture of 0.1 has a damage threshold of 248 μJ and the energy required to enter the fiber is 90 μJ. In section 5.2, the optical system that images the fiber tip to the target has been designed and simulated. In section 5.3, the damage threshold of 10 μm and 25 μm diameter core fibers could not transmit sufficient energy.

I want to acknowledge Sakshee Samir Patil for teaching me how to use Zeemax opticstudio to simulate optical design, Noah Greenberg and previous members for designing and assembling the current ablation system, and Noah Greenberg and Akbar Jahangiri Jozani for testing the ablation system and providing the ablation system requirement and valuable data I refer to during calculations.

5.1 Feasibility Study

The primary requirement for ablation is achieving sufficient fluence at the ablation target. Fluence is a measure of energy density expressed in J/cm^2. Given that the beam's area is set, the main focus of the feasibility study is to check if the fiber can deliver sufficient energy for ablation. One characteristic of the multimode fiber that impacts the amount of energy transmitted is the fiber's broadening effect. A broadened pulse laser will have a lower peak energy. To offset it, more energy should be introduced into the fiber. Therefore, the broadening effect should also be examined. The first step of the feasibility study is to clarify the desired beam waist at the target. The second step is to calculate the energy required to enter the fiber. Following this, the broadening effect is analyzed and incorporated. Finally, the fiber's damage threshold is calculated to identify the appropriate fiber for ablation.

5.1.1 Energy Entering the Fiber

The fluence, which measures energy density, depends on the size of the ablation spot. By reducing the beam waist, we can achieve the same fluence with less energy. However, the beam size cannot be too small; otherwise, the ablation experience would be inconsistent. Fig. 5.2 shows an Energy-Dispersive X-ray Spectroscopy(EDS) image displaying the distribution of barium salt on the ablation target. The gap between the two salt crystals is approximately 10 μm. To ensure a stable ablating experience, the beam size is set to approximately 100 μm.

Using 100 μm to calculate the energy required at the target and assume 50% fiber coupling efficiency, the energy entering the fiber should be about 90 μJ.

$$E_{\text{in}} = \text{fluence} \times \text{area} \div 50\% = 0.57\ \text{J/cm}^2 \times \pi(50\ \mu\text{m})^2 \times 2 = 89.6\ \mu\text{J} \tag{5.1}$$

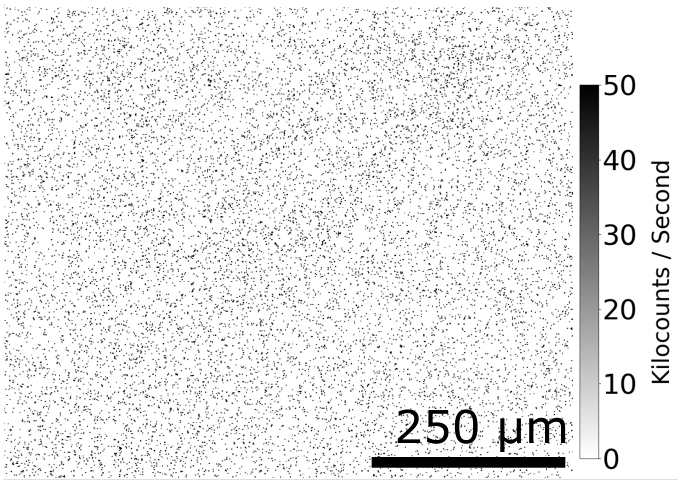

Figure 5.2: The EDS image of the target. the black dots show where barium chloride crystals are. The image reflects the distribution of barium chloride on the ablation target.

5.1.2 Broadening Effect of the Fiber Due to Mixed Modes

The broadening effect in fiber is influenced by the mixed mode of the fiber. In the context of geometric optics, different laser modes can be considered as rays that enter the fiber at various angles. Assuming the fiber has been stretched to a straight line shown in Fig. 5.3, a laser ray entering the fiber at an angle will travel a greater distance inside the fiber than a ray that goes straight through the fiber. Consequently, the angled ray will exit the fiber later, causing a broadening effect. This broadening is estimated by comparing the time it takes for a laser to travel the longest path (the angled ray) and the shortest path (the straight ray). The longest path corresponds to a laser entering at the maximum angle, which is determined by the fiber's numeric aperture.

Since the broadening effect of a longer fiber is stronger, a 1 m long fiber was chosen because it is the shortest fiber available on Thorlabs. When calculating the longest path, Snell's law has been considered to find the angle of the laser inside the fiber. Assuming the fiber is straight, all the reflective angles inside the fiber will be the same. Therefore, we can unfold the longest path into a large triangle, as shown in Fig. 5.3.

$$\sin(\theta_{\text{refrective}}) = \frac{NA}{n_{\text{Silica}}} = \frac{0.1}{1.4607} \tag{5.2}$$

$$\theta_{\text{refrective}} = 4 \tag{5.3}$$

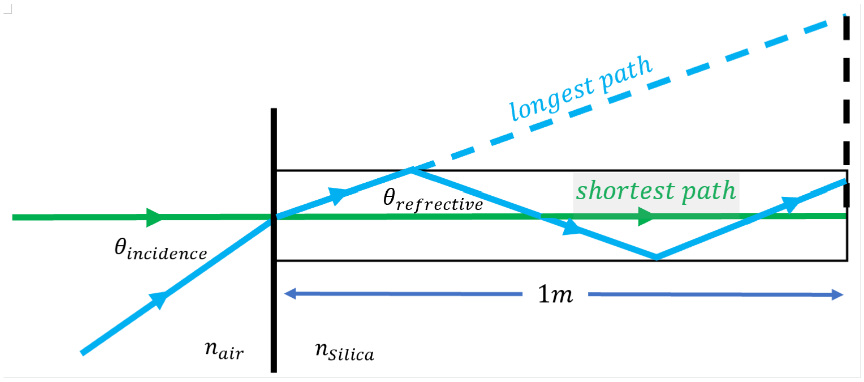

Figure 5.3: sketch of the longest beam path. The green path indicates the shortest path through the fiber. The blue path indicates the longest path through the fiber. The blue dotted line is the longest path unfolded to a straight line.

$$L_{\text{max}} = \frac{1\text{m}}{\cos(\theta_{\text{refrective}})} = 1.002\text{m} \tag{5.4}$$

$$\Delta t = T_{\text{max}} - T_{\text{short}} = \frac{L_{\text{max}}}{c/n_{\text{Silica}}} - \frac{L_{\text{short}}}{c/n_{\text{Silica}}} = 0.011 \text{ ns} \tag{5.5}$$

The broadening effect of a 1 m fiber with $NA = 0.1$ is two magnitudes lower than the pulse width, so it can be ignored. If $NA = 0.3$, the broadening is $\Delta t = 0.1$ ns. A broadening higher than it could not be ignored. Therefore, the numeric aperture of the fiber should be less than 0.3.

5.1.3 Broadening Effect of the Fiber due to Dispersion

The dispersion of a pulse laser inside a fiber is another factor contributing to the broadening effect. A laser pulse is a sum of infinitely slightly different frequencies around the main frequency. The refractive index varies for these different frequencies, causing them to travel at different speeds within the medium. As a result, some frequencies exit the fiber earlier and some later. A pulse width of 1 nanosecond corresponds to a frequency width of about 1GHz. The difference in the refractive index corresponding to this 1GHz frequency difference for the 532 nm laser is less than 0.00001[7].

$$\Delta T = \frac{1.002 \text{ m}}{c/n_{\text{high}}} - \frac{1.002 \text{ m}}{c/n_{\text{low}}} = \frac{1.002 \text{ m}}{1.46071} - \frac{1.002 \text{ m}}{1.4607} = 3 \times 10^{-5} \text{ ns} \ll 1 \text{ ns} \tag{5.6}$$

Thus, the broadening effect due to dispersion can be ignored, and we can conclude that the energy entering the fiber should be 90 μJ.

5.1.4 Damage Threshold of MM Fiber

Thorlabs is the supplier for all optical elements in this setup. According to the spec sheet, the safe level of multi-mode fiber is $\sim 1\text{GW/cm}^2$ for a 10ns pulsed laser (peak power) [8]. Therefore, the practical power is:

$$P_{\text{Peak}} = 1\text{GW/cm}^2 \times \text{area} \tag{5.7}$$

To compare the damaging power, we need to convert the peak power density to the average energy density. The energy meter measures the average energy with a 1 second sample time. Thus, 1 second is used to convert power to energy. The average power can be estimated from peak power through the pulse width to repetition time ratio. Therefore, the average threshold power is:

$$\begin{gathered} P_{\text{average}} = \frac{\text{pulse width}}{\text{repetition time}} \times P_{\text{peak}} = 1\text{ns}/1\text{ms} \times P_{\text{peak}} = 1\text{kW/cm}^2 \times \text{area} \\ \frac{E_{\text{threshold}}}{1\text{s}} = P_{\text{threshold}} \\ E_{\text{threshold}} = 1\text{kJ/cm}^2 \times \text{area} \end{gathered} \tag{5.8}$$

where $E_{\text{threshold}}$ is the damaging energy. This Laser Induced Damage Threshold (LIDT) given by Thorlabs is a 10ns pulse laser. However, the pulse length of our laser is 1ns. Therefore, we must adjust the damage threshold. According to Thorlabs equation[3]:

$$LIDT_{adjusted} = LIDT \times \sqrt{\frac{\text{Pulse Length}}{\text{Testing Pulse Length}}} \times \sqrt{\frac{\text{Wavelength}}{\text{Testing Wavelength}}} \tag{5.9}$$

Wavelength should also be considered when calculating the adjusted LIDT. However, Throlabs did not provide the testing wavelength. Therefore, the assumption that the testing wavelength is similar to 532 nm was made. The adjusted LIDT is 316.2 kJ/cm^2, and the damaging power is 248 μJ for $\emptyset$10 μm core fiber and 1552 μJ for $\emptyset$25 μm core fiber. Here $\emptyset$ indicates the number after it describes the diameter of the fiber core.

Compared to the practical damage threshold to the required input energy, the $\emptyset$10 μm core fiber will not be damaged:

$$E_{\text{Entering}} = 90\ \mu\text{J} < 248\ \mu\text{J} = E_{\text{threshold}} \tag{5.10}$$

Thus, the fiber we pick is 1 m long $\emptyset$10 μm core fiber with a Numerical Aperture (NA) = 0.1.

5.2 Optical System Design

The objective of the optical system is to project the image of the fiber tip onto the ablation target to a specific size. This can be accomplished in several ways. However, our system is sensitive to insertion loss, so the design should minimize the use of lenses. As a result, the design is based on a straightforward two-lens optical system. The size and focal length of the two lenses need to be calculated. We denote the lens closer to the fiber tip as the first lens and the lens closer to the ablation target as the second lens. Since the separation between the optical board and the ablation target is 28 cm, the second lens should have a focal length of 30 cm. It is the closest to 28 cm that is available on Thorlabs. The lens size depends on the divergence angle of the beam, as shown in Fig. 5.4. The divergence angle, Θ_{div}, is:

$$\Theta_{div} \simeq \frac{2\lambda}{\pi\omega_o} = \frac{2 \cdot 532 \text{ nm}}{\pi 50 \ \mu\text{m}} = 0.0068 \text{ rad} \tag{5.11}$$

The beam radius at the second lens, R, is:

$$R = \tan(\Theta_{\text{div}}) \cdot 30 \quad \text{cm} = 2 \text{ mm} \tag{5.12}$$

Therefore, the lens radius should be larger than 2mm.

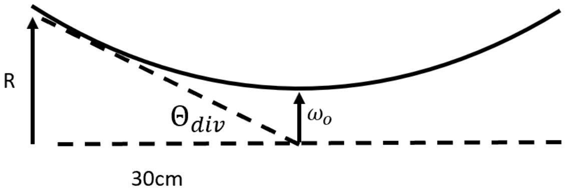

Figure 5.4: A sketch of the beam at the beam waist. R is the beam's radius at the second lens, Θ_{div} is the divergence angle, and ω_o is the beam waist.

Knowing the focal length of the second lens, the focal length of the first lens can be calculated through the desired magnification of the system:

$$M = \frac{f_2}{f_1} = \frac{\text{Image Size}}{\text{Objective Size}} \tag{5.13}$$

Magnification less than 2 is not feasible because that would require $f_1 > f_2 = 15$ cm. In this case, the lens system is too long, and the first lens needs to be very large to include all the light out of the fiber. Therefore, we can only magnify the fiber core. The larger the magnification, the shorter the lens system. The smallest fiber core available on Thorlabs is 10 μm in diameter. Thus, the magnification is 10.

$$f_1 = \frac{f_2}{M} = \frac{300 \text{ mm}}{10} = 30 \text{ mm} \tag{5.14}$$

The first lens' focal length is 30 mm. Thus, the two lenses I picked are 30 mm focal length and 300 mm focal length. The fiber is 10 μm in diameter, and $NA = 0.1$. The sketch of the optical system is shown in Fig. 5.5. Next, we need to consider the lens size. The lens must be large enough to include all the light out of the fiber. The beam radius at the first lens is then:

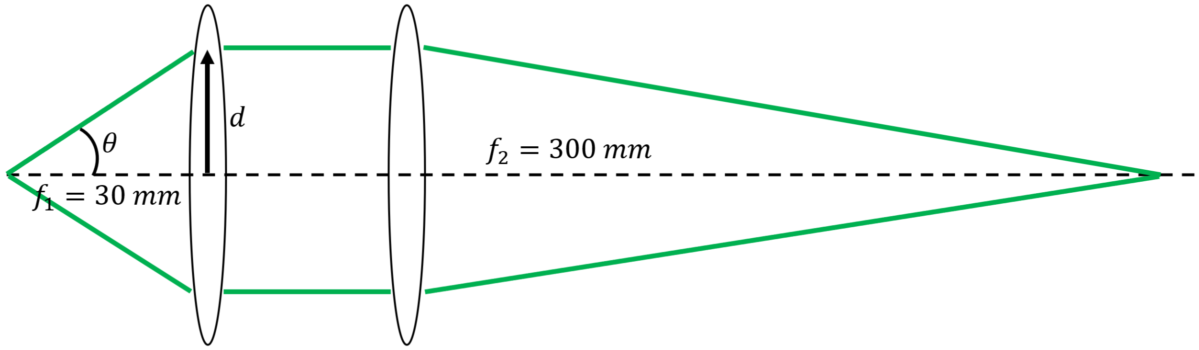

Figure 5.5: The sketch of the two lenses system where d is the beam's radius at the first lens. The objective is 10 μm in diameter, and the desired image is 100 μm in diameter.

$$d = \tan(\theta) \cdot 30 \text{ mm} = 3 \text{ mm} \tag{5.15}$$

Therefore, a 1-inch lens can easily cover the 6 mm beam diameter. It is also bigger than the beam width required to focus it under 100 μm. In conclusion, The two lenses are 30 mm and 300 mm 1-inch lenses.

The optical system was simulated using Zemax OpitcStudio to confirm the result. The simulation results are displayed in Fig. 5.6. The top left block shows the distance between lenses. From it, the length of the system is estimated to be ~ 7.5 cm, which is acceptable. The distance from the second lens to the target is 30 cm, as expected. The spot diagram on the imaging plane is shown in the right block. The "OBJ" shows the ray's position on the objective plane, and the "IMA" shows the ray's position on the image plane. Two points separated by 5 μm on the objective plane simulate the radius of the fiber. The separation between two chief rays is 49 um on the image plane, so the magnification is as expected. The simulation also shows the GEO is 76.3 μm. The GEO radius is where all the rays are enclosed. The RMS radius, the average radius of all rays, is 60.8 μm. They show most of the light has been focused within 98 μm diameter, but some aberration exists. The system's role is not just to focus the beam. It should also monitor the ablation power and align the beam with the target. To achieve this, a 10 : 90 beam splitter is added between the first and second lenses. This splitter samples light towards the target and reflects light back from the target. The light directed towards the target is focused on a photodiode to monitor the laser power. The light reflected from the target is focused on a camera to assist in beam alignment. Since the required energy is only 36% of the fiber damage

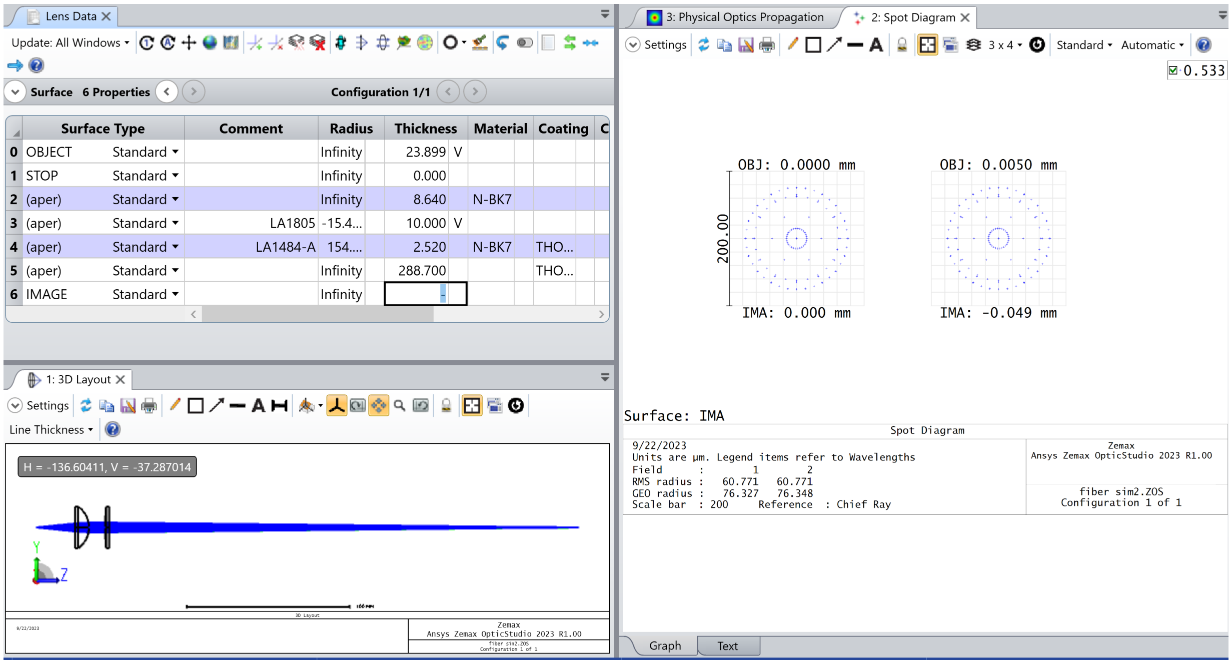

	Surface Type		Comment	Radius	Thickness		Material	Coating	C
0	OBJECT	Standard		Infinity	23.899	V			
1	STOP	Standard		Infinity	0.000				
2	(aper)	Standard		Infinity	8.640		N-BK7		
3	(aper)	Standard	LA1805	-15.4...	10.000	V			
4	(aper)	Standard	LA1484-A	154....	2.520		N-BK7	THO...	
5	(aper)	Standard		Infinity	288.700			THO...	
6	IMAGE	Standard		Infinity	-				

```
Surface: IMA
                              Spot Diagram
9/22/2023                                           Zemax
Units are µm. Legend items refer to Wavelengths     Ansys Zemax OpticStudio 2023 R1.00
Field      :       1        2
RMS radius :   60.771   60.771
GEO radius :   76.327   76.348                      fiber sim2.ZOS
Scale bar  : 200     Reference  : Chief Ray         Configuration 1 of 1
```

Figure 5.6: The Zemax simulation of the new setup. The top left block shows the distance between two surfaces in the "Thickness" column. The bottom left block is a sketch of the lens system. The right block shows the spot diagram at the image plane. Each spot is a ray trace from the object that landed on the image plane. The Rays are traced from two points from the objective plane separated by 5 μm. The IMA shows the position of the chief ray at the imaging plane and that the beam radius at the imaging plane is 49 μm, as expected.

threshold, the fiber can handle the additional energy needed to compensate for the beam splitter. The system will use two laser sources instead of one. One is a pulse laser for ablation, and the other is a low-power Continuous Wave (CW) laser for beam alignment, as shown in Fig. 5.7. Three actuators drive a linear translation stage to shift the focusing point. The entire imaging section sits on this stage. The full setup has not been assembled and tested until the feasibility of ablation through MM fiber is confirmed. The experiment will focus solely on the possibility of ablation.

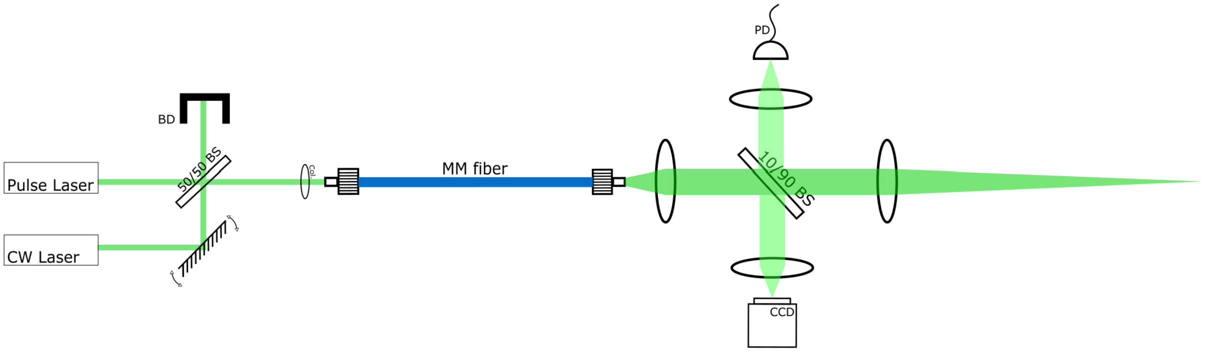

Figure 5.7: The full setup of the system, which includes power monitoring by a Photodiode (PD) and beam alignment assistance by a Charge-Coupled Device(CCD) camera. A beam splitter merges the two laser sources, and the excessive beam is ended by Beam Dump(BD).

5.3 Experiment Result

After the design and assembly phases, the system underwent experimental testing to confirm if it met the requirements. However, not every detail needed verification. The two key questions that required answers were: What is the size of the beam waist? And could fiber handle the amount of energy needed?

5.3.1 Measured Beam Waist

The beam waist was measured with a CW laser for system calibration. The DataRay's Beam'R2 - XY Scanning Slit Beam Profiler was initially used to profile the CW laser beam. By varying the distance between the profiler and the optical system, the location of the beam waist was identified. The beam diameter at the waist was found to be 84 μm, and the beam waist was located 281 mm away from the focusing lens. The beam profile at the imaging plane is shown in Fig. 5.8. Both the beam waist and the focal length met the requirements.

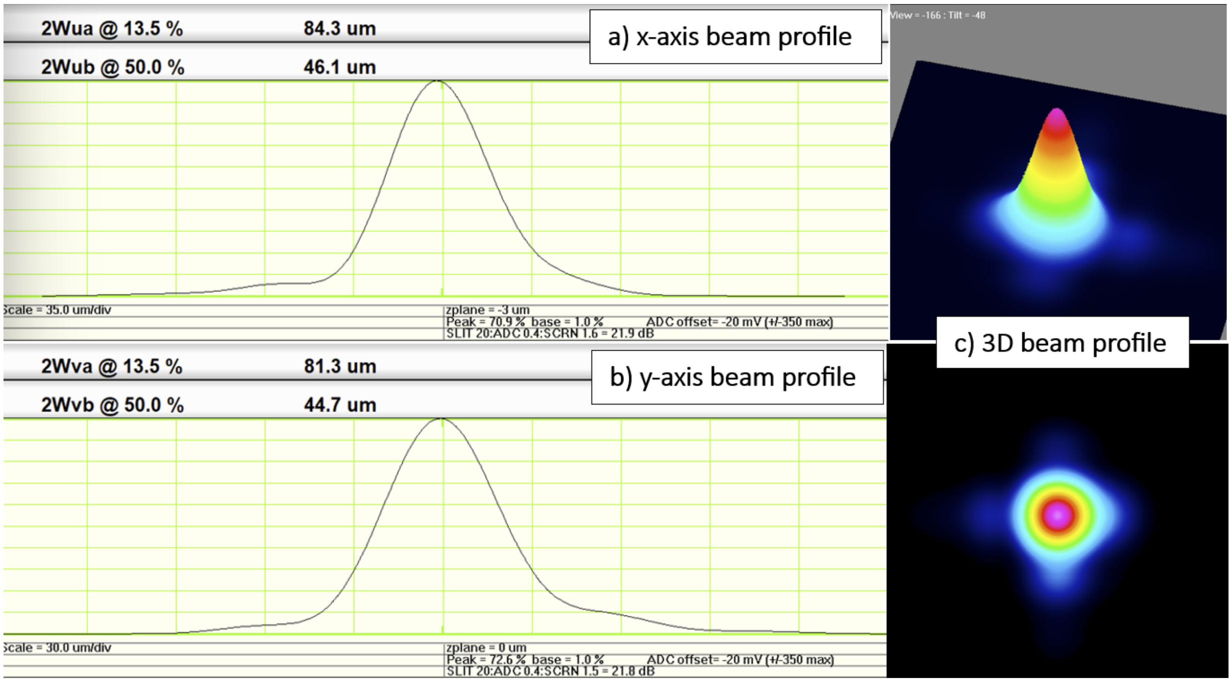

Figure 5.8: The beam profile taken by the scanning slit profiler at 281 mm distance. The a) and b) show the intensity along the y-axis and the x-axis are about 84 μm. The "2Wva@13.5%" shows the beam diameter where the intensity drops to 13.5% of peak intensity. c) shows the 3D intensity map.

5.3.2 Measured Damage Threshold

The damage threshold is determined by intentionally damaging a fiber. The 532 nm pulse laser, with a pulse width of 1 ns and a repetition rate of 1 kHz, is used for this purpose. The process involves the following steps:

1. Couple the pulse laser: The pulse laser at low power output is coupled into the multimode fiber.

2. Power Increment: The laser power is gradually increased while monitoring the output power of the fiber.
3. Damage Detection: The sudden drop in output power indicates the fiber has been damaged, and the incremental step stops.
4. Energy Measurement and Inspection: The laser energy is measured, and the fiber tip is inspected.

The energy at which damage occurs is found to be much lower than the calculated value. The ∅10 μm core fiber is damaged at an energy of 25.2 μJ, and the ablation radius is similar to the radius of the fiber core. Fig. 5.9 compares the undamaged fiber tip, the damaged fiber tip when focused on the surface, and the damaged fiber tip when focused into the ablated hole. It appears that the laser was focused only on the fiber core. Therefore, it is assumed that the radius of the beam on the fiber tip is equal to the radius of the fiber core. As a result, the damaging fluence is 32.08 J/cm^2.

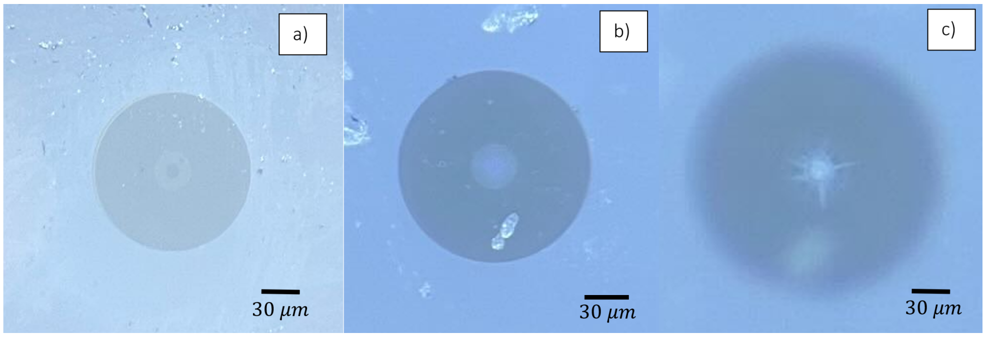

Figure 5.9: These are images of the ∅10 μm fiber core. a) Undamaged fiber. b) damaged fiber focused on the fiber tip. c) The damaged fiber that is focused into the ablated hole.

Using this measured damaging fluence, the damaging energy for a ∅25 μm core fiber was calculated to be 157.5 μJ. However, the damaging energy measured experimentally for the ∅25 μm core fiber was only 25 μJ. Upon inspecting the laser tip, it was observed that the damaged area was approximately the same size as the fiber core, as shown in Fig. 5.10.

The increase in area did not result in the expected increase in damage energy. This suggests that the intensity distribution of the multimode fiber may not be as uniform as initially assumed. To investigate this, the intensity profile of the pulse laser was captured using a CCD camera. A lens with a focal length of 100 mm was used to focus the laser onto

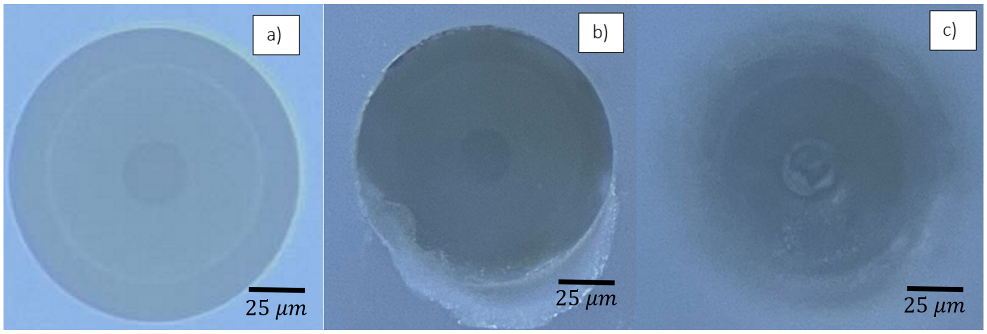

Figure 5.10: a) is the undamaged ∅25 μm fiber. b) is the input end of the damaged fiber when focused on the surface of the fiber tip. c) is the input end of the damaged fiber when focused on the damaged fiber core.

the CCD camera instead of the collimator. This was necessary because the collimator's focal length of 10 mm was too short to image the laser onto the CCD sensors without hitting the sensor shield. The 3D and 2D intensity profiles of the laser, shown in Fig. 5.11, indicate that the pulse laser is approximately Gaussian. This means there are no specific areas where the intensity is highly concentrated.

5.4 Conclusion and Discussion

In conclusion, the experiment demonstrated that Thorlabs ∅10 μm and a ∅25 μm core fiber was unable to transmit enough energy to ablate barium chloride. However, my colleague Monica was successful in transmitting a laser through a single-mode fiber. The primary difference between her experiment and mine is the ablation laser used. Monica's ablation laser has a wavelength of 1574 nm, a pulse width of 4 to 5 ns, and a repetition rate of 1 to 40 Hz[45]. In contrast, the ablation laser used in this experiment has a wavelength of 553 nm, a pulse width of < 1 ns, and a repetition rate of 1 kHz.

The laser used in this experiment has a shorter wavelength, shorter pulse width, and higher repetition rate, all of which suggest that the energy is condensed to a smaller time range. This concentrated energy could damage the fiber more easily. Adjusting the LIDT from the damage threshold measured by Monica, the damage threshold of the ∅10 μm and a ∅25 μm core fiber are 69 μJ and 431 μJ, which are still significantly higher than the measured damage threshold. Besides the wavelength and pulse width, which are considered in the LIDT equation, the repetition rate is a likely factor that caused the discrepancy in damage threshold. When the repetition rate is low, heat from the laser pulses has time to dissipate. However, when the repetition rate is high, heat could accumulate at the fiber tip and damages it [28]. However, a high repetition rate also means the peak intensity is lower if the average intensity remains the same. Thus, reducing the repetition rate would result in sending more energy to the fiber and damage the fiber more easily.

Despite these challenges, ablation via a multimode fiber is still possible. The fiber damage threshold can be increased by enlarging the fiber core diameter. However, a larger fiber core also has a larger numeric aperture. Meanwhile, the broadening effect sets an upper limit on the numeric aperture. Therefore, the fiber core diameter also has an upper limit depending on the manufacturer. Future experiments on the multimode fiber ablation solution should consider trying on the maximum fiber core diameter and remembering to lower the repetition rate of the pulse laser.

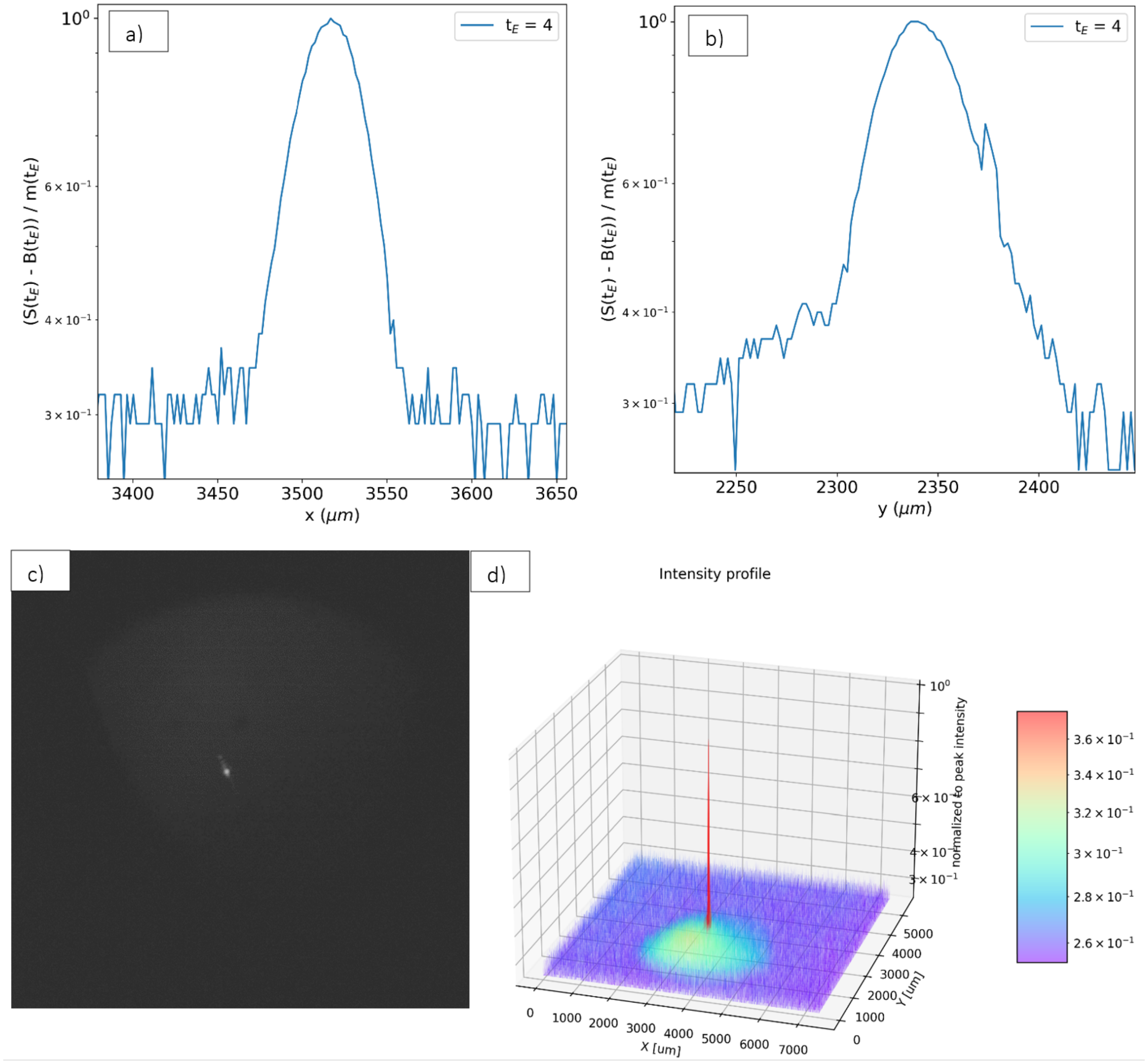

Figure 5.11: a) and b) are the pulse laser's intensity profile along the camera's x and y-axis, normalized to the peak intensity. It shows the beam has no area with a spiking power. c) is the original photo of the laser at the focus. d) shows the 3D intensity profile mapped from the whole picture. The laser appears shape because the beam size is small relative to the size of the picture. The rim around the beam might be caused by the reflection of the laser that was clipping part of the optical system.

Chapter 6

Trapping Potential and Equilibrium Positions of Ions

In previous chapters, I presented systems designed for loading, operating, and observing ions. The final component of the quantum computing platform is the trapping system. Ions, as charged particles, can interact with an electric field, which allows them to be trapped in an electric potential well. However, Gauss's law states that an electric field does not converge in free space, implying that ions cannot be trapped in a static potential. Instead, they can be trapped in a dynamic potential. For instance, a four-rod Paul trap [15] uses a dynamic electric field to trap ions. The four-rod trap employs a static field to confine the ion along the x-axis. It generates a hyperbolic parabolic potential on the y-z plane and confines the ion along the y-axis. But before the ion escapes the trap, the trap flips the hyperbolic parabolic potential to confine the ion in the z-axis. By quickly switching confinement on the y-z plane, the four-rod trap achieves confinement along all three axes. By adjusting the strength of the potential along the three axes, the ions form a one-dimensional chain, referred to as an ion chain.

The four-rod trap is widely used due to its simple structure. However, it is limited to generating a harmonic potential. Within this potential, ions are not evenly spaced at their equilibrium position. This is because the ions at the center experience the Coulomb's force from all surrounding ions, while the ions at the edge only feel the Coulomb's force from one side. As a result, the spacing between ions at the center is smaller than at the edge. The development of our individual addressing system requires ions to be evenly spaced. This system directs 16 laser beams to 16 ions, with each laser having its own Acousto-Optic Modulators(AOM) to adjust frequency, amplitude, and phase [14]. This setup allows for coupling any pair of ions in the ion chain. However, if the ions are not evenly spaced, optical engineering becomes exceptionally challenging.

On the other hand, the separation between ions should not be too large. A proper spacing between ions for our system was calculated to be approximately 4 μm. This separation strikes a balance between ion interaction strength and optical limitations. The coupling strength between two ions depends on the Coulomb's interactions between them. The closer the ions are, the stronger the coulomb's force, thus stronger the coupling strength. However, the closer the ions are, the more difficult it is to distinguish two ions. In addition, the state fidelity of one ion would be affected by the crosstalk from the laser addressing the neighbouring ion. However, when the laser crosstalk intensity is $\leq 10^{-4}$ level (10^{-4} of the peak intensity), the crosstalk is negligible. 10^{-4} levels can be achieved when ion separation is 4 times the beam waist of the laser. Lab members from another project experimentally measured $> 99.9\%$ fidelity when the addressing beam is greater and equal to 4 times the beam waist [30]. Our Raman beam objective lens has Numeric Aperture NA =0.37, corresponding to about 1 μm beam waist. Therefore, we aim at about 4m ion separation. My labmate Ali measured the laser crosstalk intensity of our individual addressing system to be 10^{-4} level [14].

In this project, I simulate the surface trap's trapping potential, calculate the ions' equilibrium position and secular frequencies, and optimize the potential to evenly spaced 12 out of 16 ions to about 4 μm apart. After finding such potential, I will analyze its properties. In section 6.1, I will introduce how a four-rod trap traps ions. In section 6.2, I will explain how to calculate the potential induced by the surface trap numerically. In section 6.3, I adapted the Controlgen Python package to write programs that optimize the trapping potential for evenly-spaced ions. I would like to acknowledge the Sandia National Laboratories for giving us the Pheonix surface trap and also Jay Van Der Wall and Collin Epstein, who wrote the Controlgen Python package I adapted to perform the simulation.

6.1 Four-rod Trap Potential

In this section, I provide how to calculate trapping potential analytically. To be consistent with other materials, I use the traditional way of defining the axis of the trap as shown in Fig 6.1. Surface traps operate under the same principle as four-rod traps. Yet, four-rod traps have the simplest geometry and can help us understand how surface traps work. According to Earnshaw's theorem, any static electric field cannot trap a charged particle. The Gauss's law states:

$$\nabla \cdot E = \frac{\rho}{\varepsilon_o} \tag{6.1}$$

When the volume charge density, ρ, is zero, the divergence of the electric field is zero. This means there are no converging electric fields in free space. Consequently, ions cannot be trapped with a static electric field. However, it is possible to trap ions using a dynamic field. An ion can be trapped in a hyperbolic parabolic potential if the hyperbola becomes a parabola before the ion can escape. A typical Paul trap accomplishes this with a quadrupole configuration. The four rods create a hyperbolic parabolic potential and flip the hyperbola to a parabola by reversing the polarity on two rods along the y-axis. The other two rods along the z-axis maintain the same polarity, as shown in Fig 6.1 a) and b). From the ion's perspective, the alternating potential appears as a potential well, known as a pseudopotential. Thus, when we apply a Radio Frequency(RF) voltage to the two y-axis rods and a Direct Current (DC) voltage to the two z-axis rods, the four rods create confinements along the y-axis and z-axis. The x-axis confinement is achieved by applying a DC voltage to the two needles pointing along the x-axis, Fig 6.1 c).

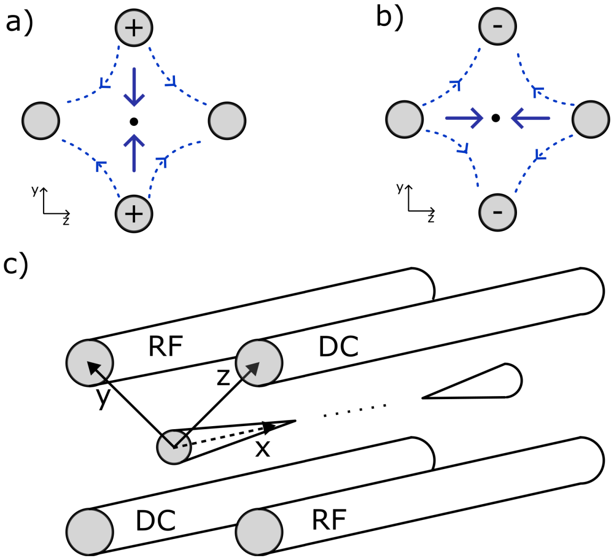

Figure 6.1: Sketchs of a Paul trap. a) and b) are the sketch of the trap on the y-z plane. The blue dotted lines show the direction of the electric field, and the blue arrows show the direction of confinement. c) Is a sketch of the Paul trap. The black dots at the center indicate the position of ions.

The quadrupole potential takes the form [26]:

$$V_{Y,Z,X} = \alpha Y^2 + \beta Z^2 + \gamma X^2 \tag{6.2}$$

where $\alpha = -2, \beta = 1, \gamma = 1$ to satisfy the Laplace equation's constraint that $\alpha + \beta + \gamma = 0$. The saddle points for both potentials are at $(Y = 0, Z = 0, X = 0)$, but the confining axes are perpendicular along the y-axis and z-axis. We can alternate between these two potentials by applying an oscillating field along the y-axis. The force equation is:

$$F_{Y(t)} = m\ddot{Y} = eE_{(t)} = eE_{0(Y)}\cos(\Omega t) \tag{6.3}$$

where m and e are the mass and charge of the ion, $E_{0(Y)}$ is the amplitude that only depends on Y, and Ω is driving RF frequency. $E_{0(Y)}$ cannot be homogeneous along Y because the electric field is stronger when the ion is closer to the rods. If the field is homogeneous, the time average of the force is zero, and the ion will not experience restoring force. Consider the homogeneous case where E_0 is constant, the time average force, $\langle F_{Y(t)} \rangle_t$, is then:

$$\langle F_{Y(t)} \rangle_t = eE_0 \langle \cos(\Omega t) \rangle_t = 0 \tag{6.4}$$

However, we can estimate the position of the ion near the saddle point using the homogeneous case. Solving equation 6.3 in the homogeneous potential case:

$$Y_{(t)} = -\frac{eE_0}{m\Omega^2}\cos(\Omega t) + Y_0 \tag{6.5}$$

where $Y_0 = \langle Y(t) \rangle_t$ is the time average position of the ion, which is the saddle point, and $E_0 = E_{0(Y_0)}$ is the time average potential at the saddle point. We could consider the inhomogeneous electric field around the saddle point as such:

$$E_{0(Y)} = E_0 + \frac{\partial E_{0(Y)}}{\partial Y}\,|_{Y=Y_0}\,(Y - Y_0) \tag{6.6}$$

Submitting equation 6.6 to the force equation 6.3 and estimate $Y - Y_0$ using equation 6.5:

$$\begin{aligned} F_{Y(t)} &= eE_{0(Y)}\cos(\Omega t) \\ &= e\cos(\Omega t)[E_0 + \frac{\partial E_{0(Y)}}{\partial Y}\,|_{Y=Y_0}\,(-\frac{eE_0}{m\Omega^2}\cos(\Omega t))] \\ &= eE_0\cos(\Omega t) - \frac{e^2}{m\Omega^2}E_0\frac{\partial E_{0(Y)}}{\partial Y}\,|_{Y=Y_0}\,\cos(\Omega t)^2 \end{aligned} \tag{6.7}$$

The time average of the force is:

$$\begin{aligned} \langle F_{Y(t)} \rangle_t &= -\frac{e^2}{2m\Omega^2}E_0\frac{\partial E_{0(Y)}}{\partial Y}\,|_{Y=Y_0} \\ &= -\frac{e^2}{2m\Omega^2}E_0\frac{\partial}{\partial Y_0}E_{0(Y_0)} \\ &= -\frac{e}{2}\frac{\partial}{\partial Y_0}\frac{e}{m\Omega^2}E_{0(Y_0)}^2 \\ &= -\frac{e}{2}\frac{\partial}{\partial Y_0}V_p \end{aligned} \tag{6.8}$$

$$V_p = \frac{e}{m\Omega^2} E^2_{0(\mathrm{Y}_0)} \tag{6.9}$$

where V_p is the pseudopotential. The superposition of the pseudopotential along the y-axis and the static potential along the z and x-axis forms the effective potential, which takes the form:

$$\phi = \frac{1}{2} m(\omega_y^2 Y^2 + \omega_z^2 Z^2 + \omega_x^2 X^2) \tag{6.10}$$

Knowing the effective potential, the frequency of the ion's motion can be calculated from the curvature of the potential well:

$$\omega_u = \sqrt{\frac{e}{2\pi m} \frac{\partial^2 V_{(u)}}{(\partial u)^2}}; u \in y, z, x \tag{6.11}$$

where ω_u is the secular frequency along an axis, it denotes the frequency of the ion's oscillation along the particular axis, u is some axis, and the second derivative of the potential is the curvature of the potential. If the curvature is greater than zero, the potential forms a convex potential well. Conversely, if the curvature is smaller than zero, the potential is concave and anti-confining.

Analyzing the motion of ions accurately requires solving Mathiues' equation. To keep it simple, consider only applying the potential on the y-z plane as an example. The effective potential is [22]:

$$\phi_{(y,z,t)} = (U - V\cos(\Omega t)) \frac{y^2 - z^2}{2r_0^2} \tag{6.12}$$

where U is the DC voltage, $V\cos(\Omega t)$ is the RF voltage, Ω is the drive frequency, and r_0 is the distance from ion to electrodes. The equation of motion of an ion of mass m and charge e is then:

$$\ddot{y} + \frac{e}{mr_0^2}(U - V\cos(\Omega t))y = 0 \tag{6.13}$$

$$\ddot{z} - \frac{e}{mr_0^2}(U - V\cos(\Omega t))z = 0 \tag{6.14}$$

They can be rewritten into Mathieu differential equations:

$$\frac{d^2 y}{d\zeta^2} + (a - 2q\cos 2\zeta)y = 0 \tag{6.15}$$

$$\frac{d^2 z}{d\zeta^2} - (a - 2q\cos 2\zeta)z = 0 \tag{6.16}$$

$$a = \frac{4eU}{mr_0^2\Omega^2};\ q = \frac{2eV}{mr_0^2\Omega^2};\ \text{and } 2\zeta = \Omega t \tag{6.17}$$

It has stable and unstable solutions depending on the value of parameters a and q. The range of a and q that both y-axis and z-axis motion are stable is plotted in Fig 6.2. If we consider just the y-axis, where we apply only RF voltage and ground DC rods, then the a parameter is zero, and the stability depends only on the q parameter. Thus, the ions' stability depends on the voltage ratio to the drive frequency. We set our is RF voltage to $V = 200$ V and the drive frequency to around $\Omega = 35$ MHz. The distance from ion to electrode, r_0, of the Phoenix trap is 140 μm. Consequently, the a and q parameters of the trap are $a = 0.0029$ and $q = 0.29$, which is in the stable region. The stable solution to Mathieu differential equation is [22]:

$$u_{(t)} = \alpha_1^{'} \sum_{n=-\infty}^{n=+\infty} C_{2n}\cos(\omega_n t) + \alpha_1^{''} \sum_{n=-\infty}^{n=+\infty} C_{2n}\sin(\omega_n t) \tag{6.18}$$

where $u_{(t)}$ is $y_{(t)}$ or $z_{(t)}$, $\alpha_1^{'}$ and $\alpha_1^{''}$ are constants depending on the initial state of the ion, $C_2 n$ is the amplitude of the oscillation, and ω_n is the secular frequency of the ion. It takes the form:

$$\omega_n = \frac{(2n \pm \beta)\Omega}{2} \tag{6.19}$$

where n is the mode number, β is related to the q parameter. The lowest three frequencies are then:

$$\omega_0 = \frac{\beta\Omega}{2}\ ,\ \omega_1 = (1 - \frac{\beta}{2})\Omega\ ,\ \omega_2 = (1 + \frac{\beta}{2})\Omega \tag{6.20}$$

6.2 Surface Trap

The Phoenix trap, fabricated by the Sandia National Laboratory, is a surface trap with a more complex geometry than the four-rod trap. The Pheonix trap features multiple pairs of electrodes and two RF rails, as depicted in Fig 6.3. A pair of electrodes refers to two electrodes with the same y coordinate. Calculating the potential analytically would be very difficult. Therefore, the potential is calculated numerically.

6.2.1 Calculating Surface Trap Potential

Sandia National Laboratory created the Controlgen Python package that calculates the potential numerically using the superposition principle. When requested to calculate the

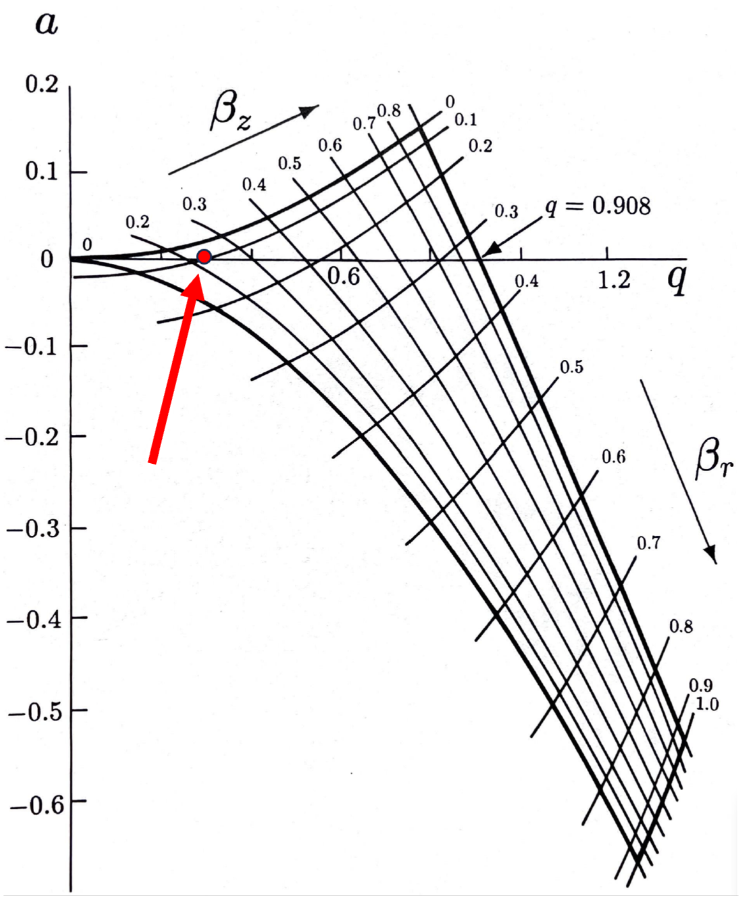

Figure 6.2: The lowest stability zone of the a and q parameters plot. The red dot marks the a and q parameters of our surface trap where $a = 0.0029$ and $q = 0.29$ The figure is adapted from [22]

potential induced by the DC electrodes to a location, it calculates the potential contributed by one electrode when 1V was applied to it while all other electrodes were grounded and then multiplies the potential with the voltage applied to this electrode. The sum of such potential contribution of all electrodes is the potential at the given location:

$$P_{DC(r)} = \sum_{i}^{\text{All Electrodes}} p_{i(r)} \cdot V_i \tag{6.21}$$

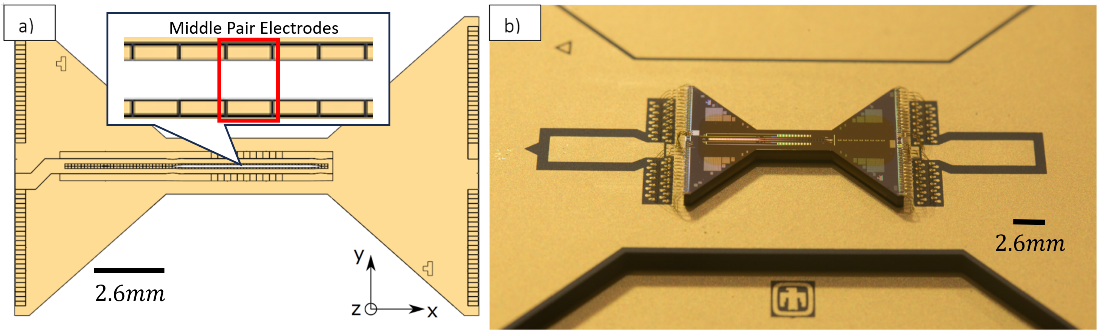

Figure 6.3: The Pheonix surface trap. a) is a 2D sketch of the surface trap. The trap axes are shown at the bottom right corner. However, the origin is at the center of the trap. b) is a photo of the real trap [35]

$$p_{i(r)} = \sum_{m}^{\text{all facet in the mesh}} \frac{e_m}{4\pi\epsilon_0 r} \tag{6.22}$$

where $\mathrm{p}_{\mathrm{i(r)}}$ is the potential contribution at point r when 1V is applied to the i th electrode, and V_{i} is the voltage applied to the ith electrode. $\mathrm{p}_{\mathrm{i(r)}}$ is calculated from the geometry of the electrode. The electrode is divided into a mesh of facets. The potential contributed by the electrode is the sum of potential contributed by each facet calculated using electrostatic. The contribution of each electrode, when 1V is applied to it, is stored in a file to reduce calculation time.

The pseudopotential is calculated using Eq.6.9:

$$P_{\mathrm{RF}(r)} = PP_{\text{constant}} \times E^2_{(r)} \quad \text{,where} \quad PP_{\text{constant}} = \frac{eV^2_{\mathrm{rf}}}{4m\Omega^2} \tag{6.23}$$

where $\mathrm{PP}_{\mathrm{constant}}$ is a constant depending on the properties of the tarp and ion, m is the ion's mass, Ω is the RF frequency, $\mathrm{E}_{\mathrm{(r)}}$ is the electric field at position r generated by the RF rail when 1V is applied to it, and V_{rf} is the voltage applied to the RF rail. $\mathrm{E}_{\mathrm{(r)}}$ is calculated from the derivative of the static potential when 1V is applied to the RF rail, and the potential is also calculated from the geometry of the RF rail.

Lastly, the potential contribution of an ion in the trap is calculated using Coulomb's law:

$$P_{\mathrm{charge}(r)} = \frac{e}{4\pi\varepsilon_0 |r - r'|} \tag{6.24}$$

where $|r - r'|$ is the distance between the measured point and position of the ion, e is the charge of the ion, and ε_0 is the permittivity of the vacuum. The potential of the trap is then:

$$P_{\text{trap}(r)} = P_{\text{DC}(r)} + P_{\text{RF}(r)} + \sum_i P_{\text{charge } i(r)} \tag{6.25}$$

Using the Controlgen package, I can calculate the trap potential by specifying the voltages on every electrode.

6.2.2 Secular Frequency Calculation

The Controlgen package also provides a function that returns the secular frequency of an ion at a specific position. The secular frequency is calculated using equation 6.11. To prevent square rooting a negative number, the sign of the curvature is moved outside the square root. Therefore, a negative secular frequency at a position means the ion is anti-confining at that position. However, this function does not calculate the motional frequency of the collective motional modes of the ions in the ion chain.

6.2.3 Equilibrium Position Calculation

I developed a Python code to calculate the equilibrium position of the ions. The equilibrium position of the ions is the position with minimum potential. When ions are present in the trap, the potential they induce also needs to be taken into account. This means that as the position of the ions changes, so does the location of minimum potential. To address this, a program was developed. The program begins by dividing the space into fine cells to achieve the desired level of accuracy. The initial position of the ions is then set. During each step of the evolution process, the ions move to the neighbouring cell with the smallest potential. After a sufficient number of steps, the ions will have reached their equilibrium position. This method does not take into account the initial conditions of the ions. It simply moves the ions to the point of lowest potential and keeps them there. The quickest evolution occurs when the initial position of the ions is the equilibrium position. The closer the initial position is to the equilibrium position, the fewer steps are needed to reach equilibrium.

6.3 Potential, Secular Frequency and Equilibrium Position Simulation

Three pairs of electrodes can generate the simplest harmonic potential well. The simplest voltage setup is to apply negative volts on one pair of electrodes and ground the rest. Fig 6.4 shows the potential along the three axes when only −1 V is applied to a pair of electrodes while the rest is grounded. The potential along the x-axis is weaker than the potential along the y and z-axis. Therefore, the ions would line up along the x-axis. The potential along the z-axis is asymmetric. However, the lowest point is still near the trap surface. Fig 6.5 shows the equilibrium positions of 16 ions along the x-axis within

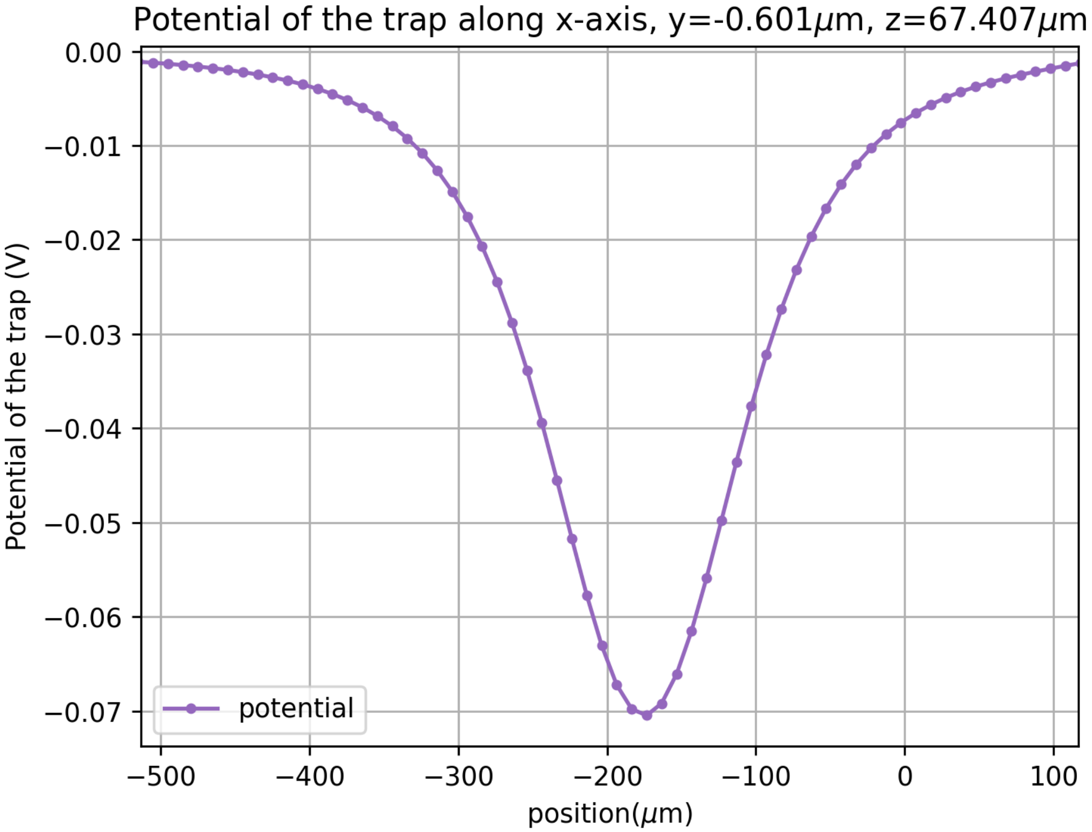

Figure 6.4: The potential of the trap when −1 V is applied to the middle pair of electrodes while the others are grounded.

this potential well. The ions in the middle section are more dense than those in the edge sections. This is because the ions in the middle sections experience the potential confining force plus the Coulomb's forces from all edge ions. The ions on the edge only experience the confining force. We couple the ions' state through the ion chain's motional mode, which is driven by lasers that address the ions with the same secular frequency. Therefore, we also would like to know the secular frequencies of the ions at their equilibrium position. Fig 6.6 adds the secular frequency of an ion along all three axes if the ion is at that position. We need to increase the potential in the middle section of the ion chain to counter the squeezing by the edge section ions. We could achieve this with five pairs of electrodes. The two edge pairs create x-axis confinement, the second pairs form the base of the potential well, and the middle pair shapes the potential into a W shape and supports the middle section electrodes. Fig 6.7 shows the spacing between two ions when we change the voltage on the edge pairs, second pairs, and middle pair electrodes. Each line plots the spacing between two neighbouring ions against the voltage applied to electrodes. We should see all lines converge to one point when the separations between ions are all equal. The figure shows that the ion's position depends on the relative voltage between electrodes. Thus, we can fix the edge and second pairs of electrodes, only modifying the middle pair to find the even spacing setup. The figure also shows that the edge ions always have a larger separation than ions in the middle section; hence, I will remove four edge ions and find a voltage that evenly spaces the middle section ions. Although the simulation shows even spacing for only 12 ions in the middle, if we trap more than 16 ions, we can find a voltage setting that provides even spacing for the middle 16 ions.

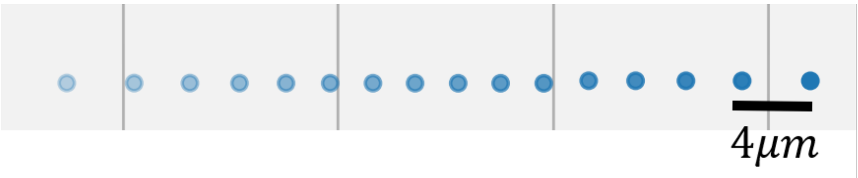

Figure 6.5: The equilibrium position of 16 ions inside the potential is shown in Fig 6.4. The spacing between ions is larger at the edge than at the center of the ion chain.

Fig 6.8 shows the zoomed-in spacing between ions when only the voltage on the middle pair electrodes is changed. The black line plots the standard deviation of the separations. When the voltage applied to the middle pair is not strong enough, we would see ions are in a similar pattern as the U shape potential well. When the voltage is too strong, we are creating two potential wells. When the voltage is just right, The spacing

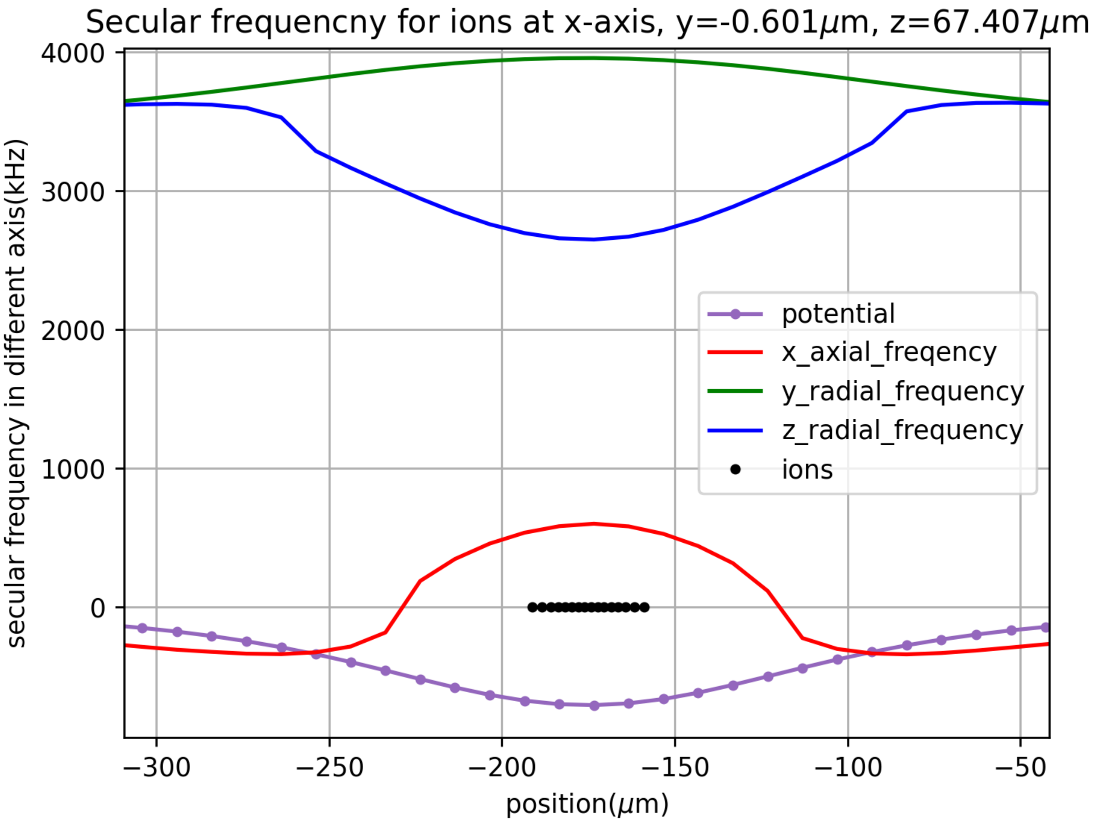

Figure 6.6: The potential of the trap with equilibrium positions and the secular frequencies along each axis.

between ions is approximately the same. However, we still won't find a point where all lines converge exactly to one point. The best voltage setting for five pairs of electrodes is $2.9\text{V}, -2.1\text{V}, 0\text{V}, -2.1\text{V}, 2.9\text{V}$. Under this configuration, the separation between the two ions in the middle is 3.3 μm, and the separation between the two ions on the edge is 3.9 μm. The standard deviation of the separation between the middle 12 ions is 0.028 μm. The y-axis secular frequency is $\sim$ 1.5 GHz bigger than the z-axis secular frequency. The secular frequencies along the y-axis and the z-axis are $\sim$ 3 GHz bigger than the secular frequencies along the x-axis, as shown in Fig 6.8. The separations between secular frequencies are desirable. With the GHz scale separation, the laser coupling to the ion's motion along one axis will not accidentally couple to the other axes. The standard deviation of the y-axis secular frequencies is 3.5 kHz. This is also desirable. The Raman lasers address ions along

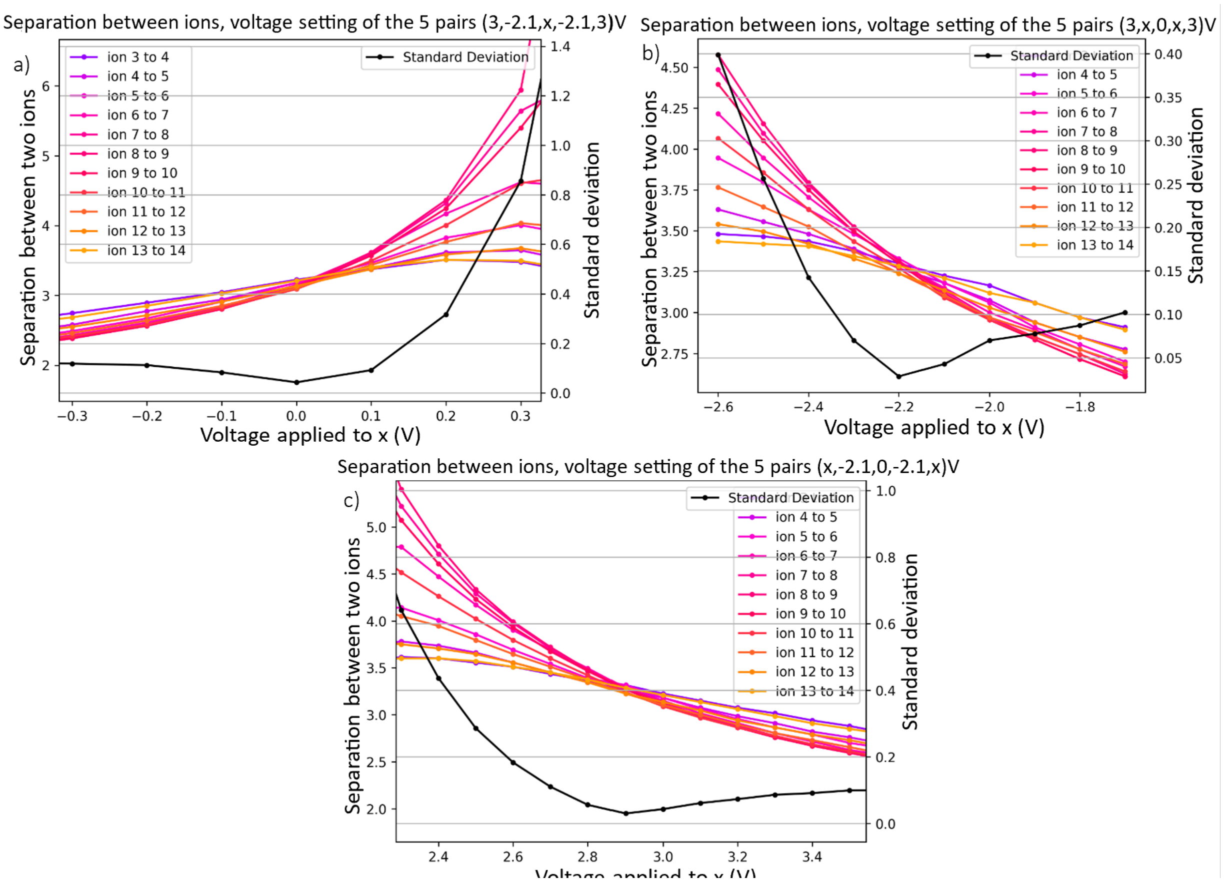

Figure 6.7: The spacing between the ions when the voltage on some electrodes varies. When all ions have equal spacing, all lines should converge to one point. The black line plots the standard deviation of the separation. a) is when the middle pair electrodes are modified. It shows the best configuration for this setup is 0 voltage. b) is when the second two pairs are adjusted. c) is when the edge pairs are adjusted.

the y-axis, so we couple the states through the y-axis ion's motion. Therefore, we wish the y-axis secular frequencies to be similar. However, this secular frequency is the frequency of a single ion, not the frequency of the phonon modes. We can use it to predict trapping but can't calculate the laser frequency detuning needed to perform the Mølmer-Sørensen(MS) gate.

In the cases mentioned above, we only modified the DC voltage. The RF voltage governs

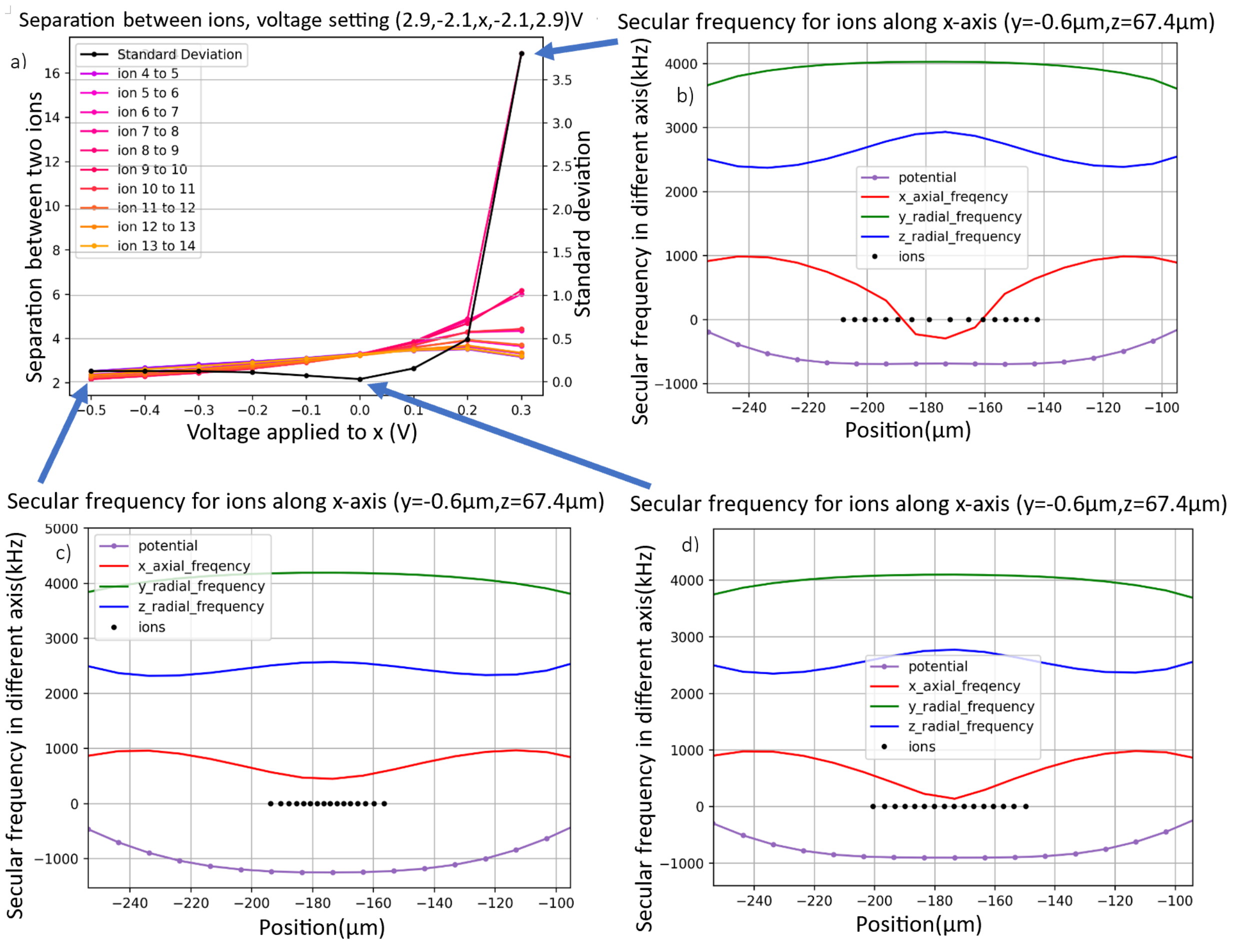

Figure 6.8: The equilibrium position of the ions changed from squeezed at the center of the ion chain to pushed out as we gradually increased the voltage applied to the middle pair electrodes. a) shows the separation between ions as the voltage applied to the middle pair electrodes increases. b) shows the equilibrium position of the ions when the potential is overly non-harmonic. c) shows the equilibrium position of the ions when the potential is still harmonic. d) show the equilibrium position of the ions when the potential is optimized for even ion spacing.

the pattern of the ion chain. We wish to keep the ion chain linear. The ion chain could be squeezed into a zigzag structure if the RF voltage is too strong. Therefore, I also plotted the separation of the ions in the y and z-axis as the RF voltage increases to the safe limit, which is 400V peak to peak, as shown in Fig 6.9. Although one ion popped out of the ion chain along the z-axis, the deviation is exactly the minimum displacement I set the program to have. Thus, it could just be two neighbouring cells with the same potential, and the program just placed the ion in one of the two cells. Therefore, we could still consider it as no deviation and conclude that we will not drive the ion chain to a zigzag structure within the safe operating voltage. To find all frequencies of the phonon modes, I should calculate the eigenvalues of the symmetrized mass-weighted Hessian matrix[39]. To conclude that this voltage setup works, the principle axis of the trapping potential should also be verified. If the principle axis is rotated with respect to the trap's axis, the motion of ions along the two axes is then coupled. For a four-rod tarp, the principal axis is reflected in the shape of the potential. The potential would be an eclipse shape, and the principal axis would be the longest and shortest radius of the eclipse. The surface trap potential looks circular, as shown in Fig 6.10. Therefore, we can not determine the principle axes by observing the potential. I should calculate the eigenvectors of the symmetrized mass-weighted Hessian matrix[39]. On the other hand, the lowest point of potential was shifted on each ion. The lowest point of potential of the mid ion was higher than the lowest point of potential of the edge ion. However, this displacement was not picked up by the equilibrium program, meaning the displacement is less than the minimum position step of the program, which is 80nm.

6.4 Conclusion

In conclusion, we have found a voltage setting that produces a trapping potential that supports evenly spaced ions. I will refer to this potential as the potential in the conclusion section. Initial analysis indicates the secular frequencies along three axes are distinct enough that laser addressing ion's motion along one axis won't couple to the ion's motion along another axis. The analysis also shows that the ion chain remains linear regardless of the strength of the RF voltage. However, a more in-depth examination of the phonon modes of the ion chain in this potential is necessary to assess its impact on quantum operations.

The potential will surely have an influence on the phonon mode of the ion chain. If we think of ions as small balls and the interacting force between them as springs, adding potential to compensate for the Coulomb force between ions is like changing the spring constant of the springs. Thus, the phonon mode of the ions will surely change. Single qubit operations, which do not involve the phonon mode of the ion chain, remain unaffected by the potential. Yet, multi-qubit operations, such as the MS gate, rely on the ion chain's phonon mode and may be influenced. However, I anticipate that the potential will not significantly impact quantum operations because the MS gate couples qubits through the ion's motion along the y-axis. In contrast, the potential affects the ion's motion along the x-axis. Therefore, the potential should not impact multi-quantum operations as long as the ion's motion along these two axes is not coupled. Nevertheless, a comprehensive understanding requires the calculation of the phonon modes of the ion chain and the contribution vectors.

At present, the simulation calculates the equilibrium position of ions based on the voltage applied to each electrode. The next step involves developing a program that inputs the desired equilibrium positions of ions and outputs the voltage solutions that can achieve it. This program will automatically attach the analysis to the potentials generated. With this functionality, we can adjust the position of ions more efficiently and adapt the trapping solution to any upcoming upgrades.

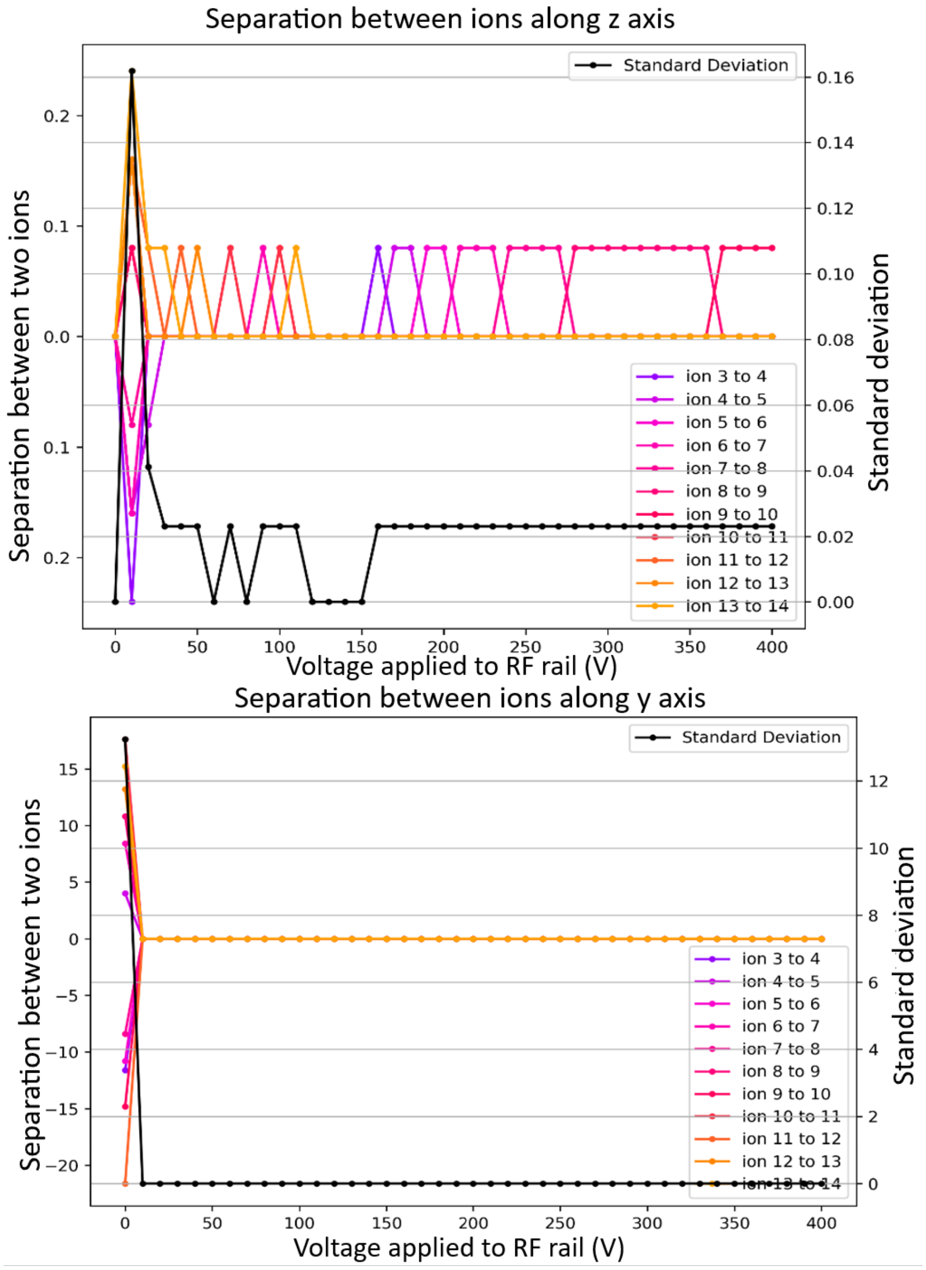

Figure 6.9: The spacing between ions along the y and the z-axis as we increase the RF power to the safe level. It shows within the safe RF operating voltage, and the ion chain will remain linear. The voltage setting for 5 pairs of electrodes are (2.9,-2.1,0,-2.1,2.9)V.

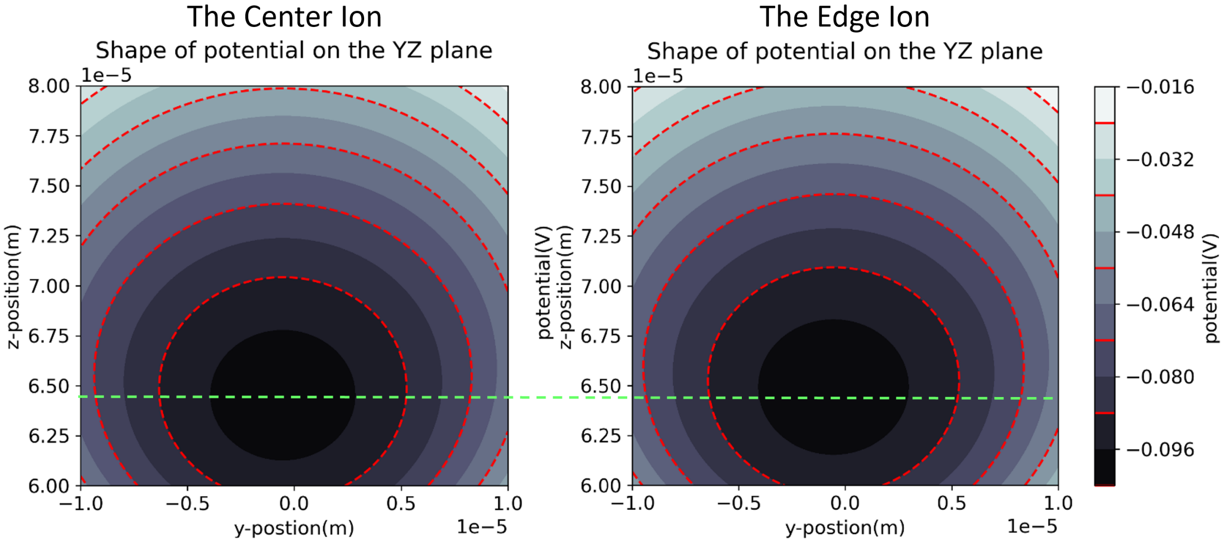

Figure 6.10: The segment of the potential on the y-z plane. The left is the cross-section of potential on the y-z plane at the position of the ion in the middle of the ion chain, while the right is the cross-section of potential on the edge of the ion chain. It shows the potential experienced by the ion at the center of the trap is about the same as the potential experienced by the ion at the edge of the trap.

Chapter 7

Conclusion and Outlook

The QuantumIon project is an initiative that aims to construct a 16-qubit trapped ion quantum computing platform accessible to the academic community. We wish to give users the ability to program quantum circuits and the ability to construct an experiment by manipulating laser properties. As a result, we need to provide remote control permissions down to the firmware level. The system's design complexity extends from firmware-level specifics, like optical boards and electronic mappings, to software-level components, including firmware control programs and quantum circuit software. We have implemented a modular architecture to reduce system downtime and ensure flexibility for future upgrades. For such a complex system to operate effectively, meticulous attention to detail and experimental verification of each innovative design is essential. However, due to the COVID-19 pandemic, we did not have the opportunity to validate all designs physically.

The system's design was completed during the pandemic. At that time, the COVID-19 pandemic was causing significant disruptions to everyday life around the globe. Scientists were dealing with limited access to their labs, and the lead time for purchasing new components was put on hold indefinitely. In these difficult circumstances, the team members did not have the necessary components to perform physical tests on each design. Our most viable strategy was to design the entire system, place orders for all the required components, and wait to test the design until the quarantine restrictions were lifted. Therefore, my work on optimization also serves as a validation of the system.

Upon joining the team, the lab space had just been made available to us, and new components had arrived. We were at the assembly stage. My role was to conduct a feasibility test on the optical system. We decided to focus on the first major milestone of the project - trapping an ion. Therefore, my primary objective was to ensure the systems

I worked on met the requirement to trap ions. I was able to verify that the optical system could provide sufficient laser power and evenly address 16 ions without causing excessive optical background noise, as demonstrated in chapter 2,3. I also indirectly proved the system's ability to observe ions, as shown in chapter 4. Furthermore, I optimized a trapping potential that supports evenly spaced ions through simulation, as shown in chapter 6, and conducted a feasibility study on delivering an ablation laser through a multimode fiber, as detailed in chapter 5.

While the system is prepared for this critical step, we have also pinpointed areas of improvement. Some issues that directly impact the trapping test have been promptly resolved. Issues that directly influence the trapping test have been swiftly addressed. Those that won't impact the test but have a lengthy resolution time have been noted and will be tackled after the ion trapping test. The work I have done, combined with the work done by my teammates in parallel, shows that the quantum computing platform is ready to trap ions. We are now close to trapping an ion.

Once an ion is successfully trapped, it opens up a multitude of opportunities for advancement. First and foremost, the trapped ion serves as an excellent reference target for optical systems. By having an ion in the trap, we can fine-tune our system and provide concrete proof of its ability to interact with and observe an ion. Secondly, the presence of a trapped ion enables us to validate fundamental operations such as state preparation and detection. Finally, we can examine the functionalities of the surface trap, such as ion shuttling. On the software side, my colleagues are working to enable remote hardware control, which will pave the way for open access to the QuantumIon platform in the long run.

References

[1] Acousto-optic modulators. Accessed Nov 30, 2023. https://www.rp-photonics.com/acousto_optic_modulators.html.

[2] Fiber-q® 532 nm 200 mhz. Accessed Nov 30, 2023. https://gandh.com/products/fiber-optics/fiber-q-fiber-coupled-modulators/fiber-q-532-nm-200-mhz.

[3] Fused silica broadband dielectric mirrors. Accessed Nov 30, 2023. https://www.thorlabs.com/newgrouppage9.cfm?objectgroup_id=139.

[4] Laser damage threshold. Accessed Nov 24, 2023. https://www.idex-hs.com/resources/resources-detail/laser-damage-threshold.

[5] M-Labs. Accessed Nov 24, 2023. https://m-labs.hk/experiment-control/artiq/.

[6] PPLN Wavelength Conversion Module — Sensing application website — NTT Innovative Devices. Accessed Nov 24, 2023. https://www.ntt-innovative-devices.com/en/sensing_application/ppln_wavelength_conversion.html.

[7] Refractive index of SiO2 (Silicon dioxide, Silica, Quartz) - Malitson. Accessed Nov 30, 2023. https://refractiveindex.info/?shelf=main&book=SiO2&page=Malitson.

[8] Step-index multimode fiber optic patch cables: Fc/pc to fc/pc. Accessed Nov 30, 2023. https://www.thorlabs.com/newgrouppage9.cfm?objectgroup_id=5794.

[9] Yuri I. Manin. Mathematics as Metaphor: Selected Essays of Yuri I. Manin. *Philosophia Mathematica*, 17(1):122–123, 04 2008. https://doi.org/10.1093/philmat/nkn013.

[10] Nitzan Akerman, Nir Navon, Shlomi Kotler, Yinnon Glickman, and Roee Ozeri. Universal gate-set for trapped-ion qubits using a narrow linewidth diode laser. *New*

Journal of Physics, 17(11):113060, 11 2015. https://doi.org/10.1088/1367-2630/17/11/113060.

[11] D. T. C. Allcock, Wesley C. Campbell, John Chiaverini, Isaac L. Chuang, Eric R. Hudson, I. D. Moore, Anthony Ransford, Conrad Roman, Jeremy Sage, and David J. Wineland. OMG blueprint for trapped ion quantum computing with metastable states. *Applied Physics Letters*, 119(21), 11 2021. https://doi.org/10.1063/5.0069544.

[12] Frank Arute, Kunal Arya, Ryan Babbush, Dave Bacon, Joseph C. Bardin, R. Barends, Rupak Biswas, Sergio Boixo, Fernando G. S. L. Brandão, David A. Buell, Brian Burkett, Yu Chen, Zijun Chen, B. Chiaro, Roberto Collins, William Courtney, A. Dunsworth, Edward Farhi, Brooks Foxen, Austin G. Fowler, Craig Gidney, Marissa Giustina, Rob Graff, Keith Guerin, Steve Habegger, Matthew P. Harrigan, Michael J. Hartmann, Alan Ho, Markus R. Hoffmann, Trent Huang, Travis S. Humble, Sergei V. Isakov, E. Jeffrey, Jiang Zhang, Dvir Kafri, Kostyantyn Kechedzhi, J. Kelly, Paul V. Klimov, Sergey Knysh, Alexander N. Korotkov, Fedor Kostritsa, David Landhuis, Mike Lindmark, Erik Lucero, Dmitry I. Lyakh, Salvatore Mandrà, Jarrod R. McClean, Matt McEwen, A. Megrant, Xiao Mi, Kristel Michielsen, Masoud Mohseni, J. Mutus, Ofer Naaman, M. Neeley, C. Neill, Murphy Yuezhen Niu, Eric Ostby, A. Petukhov, John Platt, Chris Quintana, Eleanor Rieffel, P. Roushan, Nicholas C. Rubin, D. Sank, Kevin J. Satzinger, Vadim Smelyanskiy, Kevin J. Sung, Matthew D. Trevithick, A. Vainsencher, Benjamin Villalonga, Theodore C. White, Z. Jamie Yao, P. Yeh, Adam Zalcman, Hartmut Neven, and John M. Martinis. Quantum supremacy using a programmable superconducting processor. *Nature*, 574(7779):505–510, 10 2019. https://doi.org/10.1038/s41586-019-1666-5.

[13] Paul Benioff. The computer as a physical system: A microscopic quantum mechanical Hamiltonian model of computers as represented by Turing machines. *Journal of Statistical Physics*, 22(5):563–591, 5 1980. https://doi.org/10.1007/bf01011339.

[14] Binai-motlagh, Ali. Robust optical engineering for a trapped ion quantum computer. Master's thesis, University of Waterloo, 2022. http://hdl.handle.net/10012/18710.

[15] Bramman, Brendan. Measuring trapped ion qudits. Master's thesis, University of Waterloo, 2019. http://hdl.handle.net/10012/15165.

[16] Justin Christensen, David Hucul, Wesley C. Campbell, and Eric R. Hudson. High-fidelity manipulation of a qubit enabled by a manufactured nucleus. *npj Quantum Information*, 6(1), 4 2020. https://doi.org/10.1038/s41534-020-0265-5.

[17] Canadian Nuclear Safety Commission. Radiation doses. Accessed Nov 24, 2023. `https://www.cnsc-ccsn.gc.ca/eng/resources/radiation/radiation-doses/`.

[18] K. Ehrlich, C. A. Ross, R. J. Beck, J. D. Shephard, and R. R. Thomson. A miniature fiber optic ablation probe manufactured via ultrafast laser inscription and selective chemical etching. *APL Photonics*, 8(7):076109, 07 2023. `https://doi.org/10.1063/5.0146147`.

[19] Richard P. Feynman. 2 - tiny computers obeying quantum mechanical laws. In N. Metropolis, D.M. Kerr, and Gian-Carlo Rota, editors, *New Directions in Physics*, pages 7–25. Academic Press, 1987.

[20] C.J. Foot. *Atomic Physics*. Oxford University Press, 1 2005.

[21] John Gaebler, Adam Meier, Ting Rei Tan, Ryan Bowler, Yiheng Lin, David Hanneke, John D. Jost, Jonathan Home, Emanuel Knill, D. Leibfried, and D. J. Wineland. Randomized benchmarking of multiqubit gates. *Physical Review Letters*, 108(26), 6 2012. `https://doi.org/10.1103/physrevlett.108.260503`.

[22] Pradip K. Ghosh. *Ion traps*. Oxford University Press, 1 1995.

[23] Noah Greenberg, Brendan M. White, Pei Jiang Low, and Crystal Senko. Trapping $\mathbf{Ba}^+$ with Seven-fold Enhanced Efficiency Utilizing an Autoionizing Resonance. *arxiv:2307.07627*, 7 2023. `https://arxiv.org/abs/2307.07627`.

[24] Greenberg, Noah. Vacuum and optical designs for an open-access trapped ion quantum processor. Master's thesis, University of Waterloo, 2020. `http://hdl.handle.net/10012/16334`.

[25] Paul S. Hsu, Anil K. Patnaik, James R. Gord, Terrence R. Meyer, Waruna D. Kulatilaka, and Sukesh Roy. Investigation of optical fibers for coherent anti-Stokes Raman scattering (CARS) spectroscopy in reacting flows. *Experiments in Fluids*, 49(4):969–984, 9 2010. `https://doi.org/10.1007/s00348-010-0961-6`.

[26] K.R. Islam. *Quantum Simulation of Interacting Spin Models with Trapped Ions*. PhD thesis, University of Maryland, 2012. `https://iontrap.umd.edu/wp-content/uploads/2013/10/PhDThesis_KRajibulIslam_2012.pdf`.

[27] Eirini Kakkava, Donald B. Conkey, Thomas Lanvin, Damien Loterie, Nicolino Stasio, Edgar Morales-Delgada, Christophe Moser, and Demetri Psaltis. Ultrashort pulse

laser ablation through a multi-core fiber. In *2017 Conference on Lasers and Electro-Optics Europe European Quantum Electronics Conference (CLEO/Europe-EQEC)*, pages 1–1, 2017. https://ieeexplore.ieee.org/document/8086686.

[28] Nobu Kuzuu, Kunio Yoshida, Kanyoshi Ochi, Yoshihiro Tsuboi, Tomosumi Kamimura, Hidetsugu Yoshida, and Yoshiharu Namba. Laser-Induced Bulk Damage of Various Types of Silica Glasses at 532 and 355 nm. *Japanese Journal of Applied Physics*, 43(5R):2547, 5 2004. https://doi.org/10.1143/jjap.43.2547.

[29] Sheng-Kai Liao, Wen-Qi Cai, Weiyue Liu, Liang Zhang, Li Yang, Ji-Gang Ren, Juan Yin, Qi Shen, Yuan Cao, Zhengping Li, Fengzhi Li, Xiawei Chen, Lihua Sun, Jianjun Jia, Jincai Wu, Xiaojun Jiang, Jianfeng Wang, Yongmei Huang, Qiang Wang, Yilin Zhou, Lei Deng, Xi Tao, Lu Ma, Tai Hu, Qiang Zhang, Yu-Ao Chen, Nai-Le Liu, Xiang-Bin Wang, Zhencai Zhu, Chao-Yang Lu, Rong Shu, Cheng-Zhi Peng, Jianyu Wang, and Jian-Wei Pan. Satellite-to-ground quantum key distribution. *Nature*, 549(7670):43–47, 8 2017. https://doi.org/10.1038/nature23655.

[30] Sainath Motlakunta, Nikhil Kotibhaskar, Chung-You Shih, Anthony Vogliano, Darian Mclaren, Lewis Hahn, Jingwen Zhu, Roland Hablützel, and Rajibul Islam. Preserving a qubit during adjacent measurements at a few micrometers distance. *arXiv:2306.03075*, 6 2023. http://arxiv.org/abs/2306.03075.

[31] Michael A. Nielsen and Isaac L. Chuang. *Quantum computation and quantum information*. 6 2012. https://doi.org/10.1017/cbo9780511976667.

[32] R. Paschotta. Saturation power, Oct 2007. Available online at https://www.rp-photonics.com/saturation_power.html.

[33] Wolfgang Paul and Helmut Steinwedel. Ein neues massenspektrometer ohne magnetfeld. *Zeitschrift Naturforschung Teil A*, 8:448, 06 2014.

[34] Vinay Rastogi, S. Chaurasia, and D.S. Munda. Laser induced damage studies in borosilicate glass using nanosecond and sub nanosecond pulses. *Journal of Non-Crystalline Solids*, 463:138–147, May 2017. http://dx.doi.org/10.1016/j.jnoncrysol.2017.03.006.

[35] Melissa Revelle. Phoenix and Peregrine Ion Traps. *arXiv:2009.02398*, 9 2020. https://arxiv.org/abs/2009.02398.

[36] Brandon Ruzic, Matthew N. H. Chow, Ashlyn D. Burch, Daniel Lobser, Melissa Revelle, Joshua M. Wilson, Christopher G. Yale, and Susan M. Clark. Frequency-robust Mølmer-Sørensen gates via balanced contributions of multiple motional modes. *arXiv:2210.02372*, 10 2022. http://arxiv.org/abs/2210.02372.

[37] Chris N. Self, Marcello Benedetti, and David Amaro. Protecting expressive circuits with a quantum error detection code. *Nature Physics*, 1 2024. https://doi.org/10.1038/s41567-023-02282-2.

[38] Hiroki Takahashi, Pedro Nevado Serrano, and Matthias Keller. Mølmer–Sørensen entangling gate for cavity QED systems. *Journal of Physics B*, 50(19):195501, 9 2017. https://doi.org/10.1088/1361-6455/aa8743.

[39] Teoh, Yi Hong. Machine learning and optimization techniques for trapped-ion quantum simulators. Master's thesis, University of Waterloo, 2021. http://hdl.handle.net/10012/17322.

[40] Chetan Vishwakarma, Jay Mangaonkar, Kushal Patel, Gunjan Verma, Sumit Sarkar, and Umakant D. Rapol. A simple atomic beam oven with a metal thermal break. *Review of Scientific Instruments*, 90(5), may 2019. http://dx.doi.org/10.1063/1.5067306.

[41] Pengfei Wang, Chunyang Luan, Ming Qiao, Mark Um, Junhua Zhang, Ye Wang, Xiao Yuan, Mile Gu, Jingning Zhang, and Kihwan Kim. Single ion qubit with estimated coherence time exceeding one hour. *Nature Communications*, 12(1), 1 2021. https://doi.org/10.1038/s41467-020-20330-w.

[42] Brendan M. White, Pei Jiang Low, Yvette de Sereville, Matthew L. Day, Noah Greenberg, Richard Rademacher, and Crystal Senko. Isotope-selective laser ablation ion-trap loading of $^{137}\mathrm{Ba}^{+}$ using a bacl_2 target. *Phys. Rev. A*, 105:033102, Mar 2022. https://link.aps.org/doi/10.1103/PhysRevA.105.033102.

[43] Shuqi Xu, Xiaoxing Xia, Qian Yu, Sumanta Khan, Eli Megidish, Bingran You, Boerge Hemmerling, A. M. Jayich, Juergen Biener, and Hartmut Häffner. 3D-Printed micro ion trap technology for scalable quantum information processing. *arXiv:2310.00595*, 10 2023. https://arxiv.org/abs/2310.00595.

[44] Han-Sen Zhong, Hui Wang, Yu-Hao Deng, Ming-Cheng Chen, Li-Chao Peng, Yi-Han Luo, Jian Qin, Dajun Wu, Xing Ding, Yi Hu, Peng Hu, Yang Xiao-Yan, Weijun Zhang, Hao Li, Yuxuan Li, Xiao Jiang, Lin Gan, Guangwen Yang, Lixing You, Zhen

Wang, Li Li, Nai-Le Liu, Chao-Yang Lu, and Jian-Wei Pan. Quantum computational advantage using photons. *Science*, 370(6523):1460–1463, 12 2020. `https://doi.org/10.1126/science.abe8770`.

[45] Zhu, Jingwen (Monica). Towards pulsed telecom laser ablation loading for an ytterbium ion trap. Master's thesis, University of Waterloo, 2023. `http://hdl.handle.net/10012/20057`.

Glossary

1107 nm The frequency of this laser is doubled through a doubler to create a 553 nm laser. xii, 9, 15, 23, 24

405 nm A laser wavelength that excites Barium atom's $6P_1$ state to single electron continuum. It is the second step in two-step photoionization. x, xii, xiv, 6–9, 28, 31, 32, 34, 40, 41, 44, 48

493 nm A laser wavelength that excites barium ion's $S_{1/2}$ state to $P_{1/2}$ state transition. It is used to excite ion fluorescence. It is also used for Doppler cooling. xi–xiv, 7–10, 12–14, 20, 22–25, 28, 30, 33, 34, 36, 44

532 nm A pulse laser wavelength that we use for laser ablation. The laser pulse width is < 1 ns and the repetition rate can range from 1 Hz to 2 kHz. xii, 6, 8, 9, 17, 18, 22, 23, 43, 51, 55, 56, 61

553 nm A laser wavelength that excites Barium atom's $6S_0$ state to $6P_1$ state transition. It is the first step in two-step photoionization. viii, x, xiv, 6–10, 13–15, 22, 23, 28, 44, 45, 48, 51, 63

650 nm A laser wavelength that excites barium ion's $D_{3/2}$ metastable state to $P_{1/2}$ state transition. It pumps the ion out of a metastable state to complete $S_{1/2}$ to $P_{1/2}$ state transition. It is required for ion fluorescence and Doppler cooling. xii, xiv, 7–10, 13, 14, 17, 18, 22–25, 28, 43–45